THE ASTRONOMICAL JOURNAL VOLUME 100, NUMBER 4 OCTOBER 1990

CCD SURFACE PHOTOMETRY OF GALAXIES WITH DYNAMICAL DATA. II. *UBR* PHOTOMETRY OF 39 ELLIPTICAL GALAXIES[a)]

REYNIER F. PELETIER[b)]
Kapteyn Astronomical Institute, University of Groningen, Postbus 800, NL-9700 Au Groningen, The Netherlands
and
Harvard–Smithsonian Center for Astrophysics, 60 Garden Street, Cambridge, Massachusetts 02138

ROGER L. DAVIES
National Optical Astronomical Observatory, P. O. Box 26732, Tucson, Arizona 85726-6732

GARTH D. ILLINGWORTH[b)]
Lick Observatory/University of California Observatories, University of California, Santa Cruz, California 95064

LINDSEY E. DAVIS
National Optical Astronomical Observatory, P. O. Box 26732, Tucson, Arizona 85726-6732

MICHAEL CAWSON[b)]
Steward Observatory, University of Arizona, Tucson, Arizona 85721
and
Department of Computer Science, Manchester University, Manchester M13 9BL, United Kingdom

ABSTRACT

We have obtained U, B, and R CCD surface photometry for a sample of 39 elliptical galaxies. For each galaxy we have determined the surface brightness profile, $U-R$ and $B-R$ color profiles, and the ellipticity and position angle profiles, all as a function of major axis radius, using a two-dimensional ellipse fitting program. In addition, we have derived the sin and cos 3θ and 4θ terms that describe the high-order deviations of the B and R isophotes from ellipses. While it is very common for ellipticals to display measurable 3θ and 4θ terms, the amplitudes of these terms rarely exceed 0.5%. The isophotes of elliptical galaxies are very well characterized by ellipses. The surface brightness and color profiles are given to radii at which the error in the profile reaches 0.1 mag from the uncertainty in the brightness of the night sky. We have carried out a series of simulations of the effects of seeing on luminosity and ellipticity profiles, to determine the radius beyond which the errors in our data from seeing are less than 0.05 mag and 0.02 in ellipticity. Measurable effects of seeing extend to surprisingly large radii, as much as 5–10 seeing radii, depending upon the ellipticity of the galaxy and the form of the surface brightness profile. Ellipticity and position angle profiles are usually the same in all passbands with no indication that the contours of constant color are more or less flattened than the isophotes, i.e., the isochromes and isophotes have the same shapes, but the insensitivity of the ellipticity to differences between these properties makes this a weak argument. The high-order terms, particularly the 3θ terms, appear to be sensitive diagnostics for the existence of dust in ellipticals. We find that all the galaxies in this sample either become bluer in $B-R$ and $U-R$ with increasing radius or are of constant color. Mean values for the logarithmic gradients in color are -0.09 mag (arcsec)$^{-2}$ per dex in radius in $B-R$, and -0.20 mag (arcsec)$^{-2}$ per dex in radius in $U-R$. These color changes are consistent with a decrease in the [Fe/H] of approximately 0.20 per decade in radius. Surprisingly, there is no correlation of color gradient with luminosity. It is striking, however, that the lowest luminosity galaxies in the sample (i.e., those with $M_B > -20$) do not show any color gradients. They have boxy isophotes, and are also rotationally flattened. While these properties may be related to the fact that they are companions of larger ellipsoidal systems, it could provide an important clue to the formation of ellipticals. Low luminosity ellipticals that are not close companions to giant ellipticals need to be studied.

I. INTRODUCTION

We have undertaken a program of high-precision, multicolor, surface photometry of 39 elliptical galaxies. Rotation curves and velocity dispersion profiles have been measured and published for most of the galaxies. These data provide a sound basis for exploring relationships between the structure, stellar population, and kinematics of elliptical galaxies. Our goal is to investigate the intrinsic properties of elliptical galaxies and the mechanisms that operated during their formation and evolution.

In this observing program we have emphasized the measurement of color gradients, and report the largest body of CCD surface photometry that includes observations in the ultraviolet (U) band. Together with the smaller dataset of Franx, Illingworth, and Heckman (1989b), the sample of galaxies with *UBR* data is now 55 galaxies in size. The uncertainties involved in determining $(U-R)$ gradients are small compared to the size of the gradient and so the gradients are now well established. In addition, the ultraviolet

---

[a)] Partly based on observations collected at the European Southern Observatory, La Silla, Chile.

[b)] Visiting Astronomers at Kitt Peak National Observatory, NOAO, which is operated by the Association of Universities for Research in Astronomy under contract to the National Science Foundation.

0004-6256/90/041091-52$00.90

band is more sensitive to changes in the age and metallicity of the population.

There is a well established relationship between the integrated luminosity of early type galaxies and their color such that more luminous galaxies are redder (Sandage and Visvanathan 1978). Similarly, concentric aperture photometry showed that galaxies are redder at smaller radii (Sandage 1972; Persson, Frogel, and Aaronson 1979). These two phenomena, the color–magnitude relation and the presence of color gradients, are widely thought to have a common physical origin, namely the higher metallicity of both the stellar population in more luminous galaxies and that in the centers of individual galaxies (e.g., Cohen 1979). We find that, although there is a considerable scatter, typical galaxies appear to be consistent with color gradients arising from metallicity gradients. These data will form the basis for studies of the stellar population of ellipticals, particularly for those galaxies with measured line–strength gradients (e.g., Gorgas and Efstathiou 1987; Davies and Sadler 1987). For these and other galaxies the colors allow measurement of the population characteristics at radii greater than can be made by the more direct line–strength measurements.

Models of the formation of galaxies involving the isolated collapse of a protogalactic gas cloud have been shown to generate color gradients in the end product (Larson 1975; Carlberg 1984). Color gradients have thus been used as evidence for the role of dissipational processes in galaxy formation. While Larson's models produced galaxies that are now known to rotate too rapidly and have isochromes that are probably too flat when compared to real ellipticals, subsequent work by Carlberg (1984) has resulted in more realistic models. Carlberg modeled the isolated collapse of a gas cloud and included the effect that sites of star formation have in slowing the collapse. He produced slowly rotating galaxies with a smaller flattening of the isochromes. His model predicts that more luminous galaxies should possess steeper gradients and we are able to test this.

The observed isophote twisting in ellipticals can be used to explore their intrinsic shape, particularly when combined with kinematical data. For example, if low luminosity ellipticals are oblate (Davies *et al.* 1983), they should not exhibit isophote twisting Luminosity profiles derived here can be combined with the observed kinematics for comparison with model elliptical galaxies to investigate the dependence of mass-to-light ratio with radius (e.g., Binney, Davies, and Illingworth 1990).

Recent studies of the structure of elliptical galaxies have emphasized the deviations of the isophote shapes from perfect ellipses (Jedrzejewski 1987; Bender, Döbereiner, and Möllenhaff 1988). The higher-order terms in the Fourier expansion of the isophote shapes have a typical amplitude of 0.5%–1% of the light from an isophote. They have been shown to correlate surprisingly well with both the degree of rotational support and the radio power (Bender *et al.* 1989). Here we explore these relationships further, and identify a subclass of ellipticals that do not follow these trends.

By determining the shape of galaxies in different bands we are sensitive to the presence of patchy dust. In addition, we demonstrate that the third-order terms in the Fourier expansion of the isophote shape are a sensitive indicator of the presence of dust. For galaxies free of the contaminating effects of dust we find that the shape of the stellar light is, within the errors, identical in *U*, *B*, and *R*. This sample can be used to search for relationships between the stellar population and kinematics of elliptical galaxies. We are able to investigate the recent suggestion by Vader *et al.* (1988) that those galaxies that are flattened by rotation have the steepest color gradients.

In Davis *et al.* (1985, hereafter referred to as Paper I) we described in some detail the observational program, the photometric and absolute calibration, the surface photometry analysis, and the results for a few galaxies, namely NGC 1052, NGC 3379, and M87. In this paper we summarize the basic steps, and then pay particular attention to the effects of seeing, sky subtraction, and the uncertainty in the calibration of the data for this very much larger sample. In Secs. II and III we discuss how the data were obtained, reduced, and analyzed. In Sec. IV the results of a quantitative numerical evaluation of the effects of seeing are presented, followed in Sec. V by the results of this program (with the complete data being tabulated and plotted in Appendix A). The implications of these new data are discussed and summarized in Secs. VI and VII. In Appendix B we comment on individual galaxies, noting the problems that arose during the analysis, while highlighting results of particular interest for each galaxy. In a later paper we will analyze the observed color gradients and their relationship to other galaxy parameters in more detail.

II. OBSERVATIONS

The elliptical galaxy sample was selected primarily from the tabulation by DEFIS of 58 ellipticals with velocity and velocity dispersion profiles. In addition, we included those ellipticals in the kinematic mapping study by Davies and Birkinshaw (1988) for which surface photometry was not available, as well as a selection of very luminous ellipticals (cD's and other brightest cluster members). These latter galaxies were taken from Tonry and Davis (1981), Carter *et al.* (1985), and Illingworth and Jedrzejewski (1990). The sample consists of 39 elliptical galaxies ranging in ellipticity from $\epsilon \approx 0$ to $\epsilon \approx 0.6$, and with absolute luminosities in the range $-18 > M_B > -24.5$ (for $H_0 = 50\,\mathrm{km\,s^{-1}\,Mpc^{-1}}$). In Table I we have summarized some basic data for the galaxies of the sample.

The objects were observed between May 1982 and May 1985 with the No. 0.9 m and 2.1 m telescopes at Kitt Peak National Observatory. The data from the two telescopes are complementary. The RCA CCD on the 0.9 m telescope offered a large field of view ($5' \times 7'$), but poorly sampled data, and was best suited to observing the largest and brightest galaxies, whereas the 2.1 m with the RCA CCD gave us the higher spatial resolution and better sampling that was advantageous for the smaller and fainter galaxies. The pixel sizes were 0.38″ at the 2.1 m and 0.86″ at the 0.9 m. The field of the 2.1 m CCD was $3.2'\,(E-W) \times 2.0'\,(N-S)$. A log of the observations is presented in Table II.

Exposure times were typically 600 s in *R*, 1600 s in *B*, and 2000 s in *U*. These times were chosen to equalize the signal-to-noise ratio achieved on the galaxy in *R* and *B*; at the point where the galaxy is 5% of the sky brightness a S/N of approximately 15 is achieved by averaging 50 pixels. The exposure time in *U* was sufficient to produce good data only to radii approximately one half of those in *B* and *R*. Conditions were not always photometric, but this was of little importance since the data were to be calibrated using aperture photometry from the literature (see Sec. III*c*). Experience has shown this to be a more reliable approach.

TABLE I. Global parameters.

Galaxy	Classification		v_{grp}	M_{B_T}	Environment
	RC2	RSA	km s^{-1}		
(1)	(2)	(3)	(4)	(5)	(6)
NGC 315	SA0	- -	5303	-23.59	- -
NGC 720	E5/E3	E5	1728	-21.53	- -
NGC 741	E0/E1	E0	5347	-23.10	Group with N742
NGC 1052	E4/E2	E3/S0	1392	-20.94	Brightest in N1052 group
NGC 1129	- -	- -	5320	-23.68	AWM 7
NGC 1600	E3/E2	E4	4846	-23.14	N1600 group
Abell 496	- -	- -	9780	-23.16	- -
NGC 2300	SA0/E1	E3	2256	-21.54	- -
NGC 2768	E6/E5	$S0_{0,1}$	1355	-21.16	- -
NGC 2778	- -	- -	1827	-19.51	Group with N2779
NGC 2832	E2	E3	6780	-22.86	Group with N2831
NGC 3377	E5/E5	E6	667	-19.50	Leo group
NGC 3379	E1/E1	E0	667	-20.20	Leo group
NGC 3605	E4/E3	E5	1033	-18.34	In N3607 group
NGC 3665	SA0/E2	$S0_3$	2090	-21.36	- -
NGC 3801	S0p	- -	3171	-21.33	Pair with N3802. Dusty
NGC 4261	E2/E2	E3	2087	-21.78	Pair with N4264
NGC 4278	E1/E1	E1	754	-19.87	Pair with N4283
NGC 4374	E1/E1	E1	1074	-21.53	- -
NGC 4387	E5	- -	1074	-18.79	- -
NGC 4406	E3/E3	$S0_1$/E3	1074	-21.79	- -
NGC 4472	E2/E4	E1/$S0_1$	1074	-22.34	Pair with N4467
NGC 4478	E2/E1	E2	1074	-19.52	Pair with N4476
NGC 4486	E0p/E1	E0	1074	-22.14	Virgo A
NGC 4551	E3	- -	1074	-18.94	Pair with N4550
NGC 4636	E0/E1	E0/$S0_1$	1074	-21.46	- -
NGC 4649	E2/E1	$S0_1$	1074	-21.89	Pair with N4647
NGC 4697	E6/E4	E6	1071	-21.63	- -
NGC 4874	E0	- -	6931	-23.40	Central Coma galaxy
NGC 4889	E4/E4	E4	6931	-23.23	Central Coma galaxy
NGC 5638	E1/E1	E1	1596	-20.47	Pair with N5636
NGC 5813	E1/E1	E1	1673	-21.23	In N5846 group
NGC 5831	E3/Ep	E4	1673	-20.33	- -
NGC 5845	E3	- -	1673	-19.27	In N5846 group
IC 1101	- -	- -	23300	-24.40	Abell 2029 cD
NGC 6051	E4	- -	9722	-22.95	AWM 4
NGC 6086	E2	- -	9704	-22.95	Abell 2162 cD
NGC 6269	- -	- -	10700	-23.63	AWM 5
NGC 7626	E1p/E2p	E1	3693	-22.35	Second brightest in Pegasus I

Notes to TABLE I

Columns (2) and (3) list the galaxy classifications from the RC2 (De Vaucouleurs *et al.* 1976) and the RSA (Sandage and Tammann 1981). Column (4) gives the group velocity from Davies *et al.* (1987), corrected for the motion with respect to the centroid of the local group, using the approach in the RC2. Column (5) lists the integrated blue luminosity M_{B_T}, calculated using the group velocity and B_T from Burstein *et al.* (1987). For a few galaxies other sources have been used to obtain the group velocity and the apparent blue magnitude. The remarks on the environment of the galaxies in column (6) are taken mostly from the RC2.

1990AJ....100.1091P

TABLE II. Observation log.

Galaxy (1)	RA (2)	Dec (3)	Obs./Tel.[2] (4)	Qual. (5)	Band (6)	Exp.times (7)
NGC 315[1]	00 55.1	30 05	Jan 84/0.9[2]	2	R	100,600
					B	1600
					U	2000
NGC 720	01 50.6	-13 59	Oct 82/0.9	2	R	600
					B	1600
					U	2000
NGC 741	01 53.8	05 23	Jan 84/0.9	2	R	100,600
					U	2000
			Dec 86/1.5		R	200
					B	360
NGC 1052	02 38.6	-08 28	Oct 82/0.9	1	R	100,600
					B	800+800
					U	2000
NGC 1129[3]	02 52.9	41 26	Jan 84/0.9	2	R	100,600
					B	1600
					U	2000
NGC 1600	04 29.2	-05 12	Oct 82/0.9	2	R	600
					B	1600
					U	2000
			Dec 86/1.5		R	180
					B	300
Ab. 496[3]	04 31.3	-13 22	jan 84/0.9	3	R	100,1200
					B	2400
					U	3600
NGC 2300[3]	07 16.0	85 49	apr 84/0.9	2	R	100(2),600
					B	1600
					U	2000
NGC 2768	09 07.7	60 15	Apr 84/0.9	1	R	100,600
					B	1600
					U	2000
NGC 2778	09 09.2	35 13	Jan 84/0.9	1	R	600+600
					B	1600+1600
					U	2000+2000
			May 85/2.1		R	300+300
					B	1000
					U	2400
NGC 2832	09 16.8	33 58	Jan 84/0.9	1	R	600
					B	1600
					U	2000
NGC 3377	10 45.1	14 15	May 85/2.1	1	R	50,100
					B	150
					U	1800
NGC 3379	10 45.2	12 51	Jan 84/0.9	1	R	100
					U	2000
			Apr 84/0.9		R	100(2),300(2)
					B	1600
NGC 3605[4]	11 14.1	18 17	Apr 84/0.9	1	R	100(2),600(2)
					B	1600(2)
					U	2000
			May 85/2.1		R	300(2)
					B	1000
					U	2400
NGC 3665	11 22.0	39 02	Jan 84/0.9	1	R	100,600
					B	1600
					U	2000
NGC 3801	11 37.7	18 00	Jan 84/0.9	1	R	100,600
					B	1600
					U	2000
NGC 4261	12 16.8	06 06	Jan 84/0.9	1	R	100,600
					B	1600
					U	2000
NGC 4278	12 17.6	29 33	Jan 84/0.9	1	R	100,600
					B	1600
					U	2000
NGC 4374	12 22.5	13 10	Jan 84/0.9	1	R	100,600
					B	1600
					U	2000
			May 85/2.1		R	100(2)
					B	300
NGC 4387[3]	12 23.2	13 05	Jan 84/0.9	1	R	100,600
					U	2000
			Apr 84/0.9		R	100,600
					U	1600
			May 85/2.1		R	300(3),600
					B	2000
					U	2400
NGC 4406	12 23.7	13 14	Jan 84/0.9	1	R	100,600
					B	1600
					U	2000
NGC 4472	12 27.3	08 16	Apr 84/0.9	1	R	100,300
					B	1600
					U	2000
NGC 4478[3]	12 27.8	12 36	Jan 84/0.9	1	R	100,600
					B	1600
					U	2000
			May 85/2.1		R	300(2)
					B	1000
					U	2400
NGC 4486	12 28.3	12 40	Mar 84/0.9	1	R	300
					B	600(2)
					U	2000
NGC 4551[3]	12 33.1	12 32	Jan 84/0.9	1	R	600
					U	2000
			Apr 84/0.9		R	100,600
					B	1600
			May 85/2.1		R	300(2)
					B	1000
					U	2400
NGC 4636	12 40.3	02 58	Apr 84/0.9	1	R	100,600
					B	1600
					U	2000
NGC 4649	12 41.2	11 49	Apr 84/0.9	1	R	100,600
					B	1600
					U	2000
NGC 4697	12 47.1	-05 40	Jan 84/0.9	1	R	100(2),300
					U	2000(2)
			Apr 84/0.9		R	100,300
					B	600,1600
NGC 4874	12 57.2	28 14	Jan 84/0.9	3	R	100,600
					B	1600
					U	2000
NGC 4889	12 57.7	28 15	Jan 84/0.9	2	R	100,600
					B	1600
					U	2000
NGC 5638	14 27.2	03 27	May 85/2.1	1	R	300,1000(2)
					B	2000
					U	2400
NGC 5813[3]	14 58.6	01 53	Jan 84/0.9	1	R	600
					U	2000
			Apr 84/0.9		R	100(2),600
					B	1600(2)
			May 85/2.1		R	300(2)
					B	1000
					U	2400
NGC 5831[3]	15 01.6	01 24	Jan 84/0.9	1	R	100,600
					U	2000
			Apr 84/0.9		R	100,600
					B	1600
			May 85/2.1		R	300(2)
					B	800
					U	2400
NGC 5845[3]	15 03.5	01 48	Jan 84/0.9	1	R	100,600
					U	2000
			Apr 84/0.9		R	100,600
					B	1600
			May 85/2.1		R	150(2),300
					B	500
					U	2400
IC 1101	15 08.4	05 56	Apr 84/0.9	1	R	600,1200
					B	1600
					U	2000
			May 85/2.1		R	600,1000(2)
					B	2000(2)
					U	2400(2)

TABLE II. (continued)

Galaxy (1)	RA (2)	Dec (3)	Obs./Tel.[2] (4)	Qual. (5)	Band (6)	Exp.times (7)
NGC 6051	16 02.8	24 04	May 85/2.1	3	R	300(3)
					B	1000
					U	2400(2)
NGC 6086	16 10.5	29 38	Apr 84/0.9	3	R	100,600
					B	1600
					U	2000
			May 85/2.1		R	300
					B	1000
					U	2100
NGC 6269	16 56.0	27 56	Apr 84/0.9	3	R	100,600
					B	1600
					U	2000
			May 85/2.1		R	300,600
					B	2000
					U	2100
NGC 7626	23 18.2	07 56	Oct 82/0.9	1	R	600
					B	600
					U	2000

Notes to TABLE II

The R.A. and Dec. in columns (2) and (3) are 1950 coordinates. The Quality parameter in column (5) is discussed in the text. The exposure times are in seconds.

[1] For NGC 315, the scattered light from a very bright star close to the frame was modeled and subtracted.

[2] Telescopes: **2.1** – 2.1 m KPNO; **0.9** – #1 0.9 m KPNO; **1.5** – 1.5 m Danish telescope at ESO.

[3] A N–S ramp in the background across the detector that was caused by leakage from a red light close to the detector was modeled and subtracted from the 0.9 m *R*-band frames.

[4] A sloping background due to contamination from a large nearby galaxy, NGC 3607, was subtracted.

The characteristics of the RCA CCDs used on the No. 1 0.9 m telescope are given in Paper I. That used on the 2.2 m was similar, except for a high radiation event rate. The events could easily be masked and caused no problems. None of the CCDs showed any significant fringing with the filters used. The characteristics of the *U*, *B*, and *R* filters used on both telescopes are summarized in Table III of Paper I. The KPNO Mould *U*, *B*, and *R* filter set was used for these observations, and the results transformed onto the Cousins system (see Paper I, and Sec. III).

III. REDUCTION AND ANALYSIS

The data were reduced as described in Paper I. We determined the median bias level from the 32 column overscan region of each row of each frame and subtracted it. We then trimmed the frames to 320×512, subtracted the bias frame, and divided each galaxy and star frame by the flat-field frame taken through the appropriate filter. We used high S/N dome flat-field frames taken at the beginning and end of each night. Sky frames were used to verify, and correct if necessary, the uniformity of the flat fields. No fringing (>0.5%) from night sky lines was observed. We subsequently noticed that some *R* frames from the No.1 0.9 m telescope, contained small (<1.5% across the detector) background gradients from north to south. These frames are identified in Table II. The gradients were removed by subtracting a linear fit to the background. The gradients were apparently due to an inadequately masked red light in the dome.

a) Isophote Fitting and Profiles

Luminosity profiles were determined using a version of GASP (Cawson 1983). The GASP system has been described in detail in Paper I. It is used interactively in conjunction with a color-image display. A device mask, identifying all the "bad" pixels on a given CCD, was generated and applied to all frames, so that none of the "hot" pixels or columns with traps, etc., were included in the analysis. For each galaxy frame, all the interfering images that were superimposed on the galaxy to be measured, such as stars, small companion galaxies, and cosmic rays, were automatically identified and masked out. In some cases this automatic procedure was augmented by manual identification of objects. Elliptical isophotes were then fitted to the galaxy using a revised version of the program PROF. We are grateful to R. Jedrezejewski for giving us a much faster version of this program.

The program takes the preliminary (x,y) center, position angle, and ellipticity which had been estimated in the image-finding step, and samples the pixel data around an ellipse of given major-axis length. If the isophotes of the galaxy are elliptical, and the estimated parameters of the sampling ellipse are close to the true values, then the variation in pixel values $I(\theta)$ around the sampling ellipse can be expressed as a Fourier series with small first- and second-order terms. The intensity along the ellipse is approximated by

$$I(\theta) = I_0\left(\sum_{i=1}^{2} C_i \cos(i\theta) + \sum_{i=1}^{2} S_i \sin(i\theta)\right),$$

and this equation is fitted to give the Fourier coefficients. An iterative least-squares-fitting procedure adjusts the ellipse parameters until the sum of the squared residuals between the data and the ellipse is smaller than a set threshold, or a set number of iterations has been reached. The process was repeated at major-axis radii each of which was a factor 1.1× larger than the previous step, until less than 60% of an isophote was included in the frame, or the galaxy surface brightness fell to 1% of the sky.

The final step at each radius is the determination of any deviations from elliptical isophotes. The third- and fourth-order Fourier coefficients were determined from fitting

$$I(\theta) = I_0\left(\sum_{i=1}^{4} C_i \cos(i\theta) + \sum_{i=1}^{4} S_i \sin(i\theta)\right),$$

with the low-order coefficients held constant. That is, in this final step there was no iteration; C_1,C_2 and S_1, S_2 were held constant. We simply solve for the high-order terms, and so the coefficients do not strictly describe an isophote; the error introduced is inconsequential, since the deviations are very small, being typically 0.5%.

An ellipse is specified completely by the first- and second-order Fourier terms, so the third- and fourth-order coefficients are zero for perfectly elliptical isophotes. However, nonzero values for the third- and fourth-order components

TABLE III. Seeing, background, and cutoff radii.

Galaxy (1)	r_e ″ (2)	ϵ at 10″ (3)	Band (4)	Seeing ″ (5)	Sky (6)	Profile (7)	Ext. + K Correction (8)	Inner Cutoff (9)	Outer Cutoff (10)
NGC 315	68	0.26	R	2.3	20.59	R	0.08	3.2	122.2
			B	3.0	22.12	B - R	0.11	6.3	57.0
			U	3.5	21.72	U - R	0.12	7.7	57.0
NGC 720	52	0.40	R	2.1	20.34	R	0.01	2.6	163.0
			B	2.1	21.88	B - R	0.02	2.6	111.1
			U	2.4	20.84	U - R	0.01	4.0	69.0
NGC 741	57.5	0.17	R	1.4	20.10	R	0.02	2.1	83.4
			B	1.4	21.67	B - R	0.07	2.1	51.8
			U	2.8	21.14	U - R	0.05	7.0	32.2
NGC 1052	36.5	0.28	R	2.4	20.42	R	0.00	3 .4	122.2
			B	2.4	22.03	B - R	0.02	3.4	83.4
			U	2.4	21.31	U - R	0.02	3.4	62.7
NGC 1129	>50	0.20	R	2.3	20.43	R	0.21	3.4	163.0
			B	2.4	21.88	B - R	0.23	3.6	91.8
			U	2.7	21.42	U - R	0.27	4.5	57.0
NGC 1600	56	0.35	R	1.2	20.33	R	0.08	1.6	123.0
			B	1.2	21.90	B - R	0.11	1.6	62.7
			U	2.8	21.25	U - R	0.11	5.4	35.4
Abell 496	93*	0.21	R	2.1	20.36	R	0.08	3.1	57.0
			B	2.3	21.78	B - R	0.17	3.4	35.4
			U	2.5	21.12	U - R	0.15	4.7	26.6
NGC 2300	55*	0.20	R	3.5	20.08	R	0.09	5.4	134.4
			B	3.6	21.74	B - R	0.10	5.6	69.0
			U	4.6	20.99	U - R	0.12	7.5	42.8
NGC 2768	76.5	0.40	R	2.0	20.46	R	0.05	2.5	230.1
			B	2.0	22.12	B - R	0.05	2.5	193.8
			U	2.0	20.69	U - R	0.05	2.5	105.0
NGC 2778	18.5	0.21	R	1.7	20.78	R	0.04	2.7	48.6
			B	1.8	22.51	B - R	0.05	2.9	36.5
			U	1.9	21.97	U - R	0.05	3.0	30.2
NGC 2832	46.5*	0.28	R	2.1	20.69	R	0.05	2.9	134.4
			B	2.1	22.20	B - R	0.12	2.9	75.8
			U	2.2	21.85	U - R	0.11	3.1	51.8
NGC 3377	46	0.46	R	1.5	20.25	R	0.00	1.8	96.0
			B	1.6	21.66	B - R	0.01	1.9	86.9
			U	1.9	21.72	U - R	0.01	4.9	86.9
NGC 3379	37.5	0.10	R	2.0	20.41	R	0.00	3.3	170.0
			B	3.4	22.17	B - R	0.01	6.6	127.8
			U	2.1	21.64	U - R	0.01	3.5	105.6
NGC 3605	22.5	0.40	R	2.3	20.53	R	0.00	2.9	39.7
			B	2.0	22.10	B - R	0.01	2.9	32.8
			U	2.3	21.49	U - R	0.01	2.9	27.1
NGC 3665	65.5*	0.38	R	2.2	20.87	R	0.01	2.8	178.9
			B	2.1	22.56	B - R	0.02	2.8	111.1
			U	2.2	21.92	U - R	0.02	2.8	83.4
NGC 3801	44.5*	0.30	R	2.1	20.81	R	0.01	2.9	86.9
			B	2.6	22.41	B - R	0.04	4.9	65.2

TABLE III. (continued)

Galaxy (1)	r_e ″ (2)	ϵ at 10″ (3)	Band (4)	Seeing ″ (5)	Sky (6)	Profile (7)	Ext. + K Correction (8)	Inner Cutoff (9)	Outer Cutoff (10)
NGC 4261	42.5	0.24	U	3.2	22.23	U - R	0.03	7.0	59.3
			R	2.5	20.68	R	0.01	3.7	125.9
			B	2.6	22.28	B - R	0.02	3.8	78.2
NGC 4278	35	0.14	U	2.7	22.10	U - R	0.02	4.0	64.7
			R	2.0	20.71	R	0.00	3.2	160.0
			B	1.7	22.21	B - R	0.01	3.3	108.1
NGC 4374	57	0.20	U	2.7	21.87	U - R	0.01	5.1	89.4
			R	1.6	20.65	R	0.00	2 .4	164.0
			B	1.8	22.48	B - R	0.01	3.3	163.3
NGC 4387	20	0.40	U	4.0	22.15	U - R	0.01	6.3	112.0
			R	1.8	20.76	R	0.00	2.3	60.0
			B	2.2	22.10	B - R	0.01	2.8	44.0
NGC 4406	104.5	0.18	U	1.9	21.57	U - R	0.01	2.4	33.0
			R	2.0	20.65	R	0.00	3.0	175.0
			B	2.1	22.36	B - R	0.01	3.2	158.8
NGC 4472	114	0.20	U	2.7	21.89	U - R	0.01	6.4	108.5
			R	2.0	20.40	R	0.01	3.0	172.0
			B	2.3	22.05	B - R	0.01	3.9	156.0
NGC 4478	15.5	0.20	U	2.9	21.43	U - R	0.01	7.0	155.3
			R	1.9	20.95	R	0.00	3.1	69.3
			B	2.0	22.47	B - R	0.02	3.3	57.7
NGC 4486	110	0.03	U	2.3	22.08	U - R	0.02	3.9	43.5
			R	2.5	20.19	R	0.00	4.3	163.0
			B	2.5	22.06	B - R	0.01	4.3	148.0
NGC 4551	21	0.26	U	2.5	21.40	U - R	0.01	4.3	147.8
			R	1.8	20.70	R	0.00	2.7	57.8
			B	1.8	22.30	B - R	0.01	2.7	43.5
NGC 4636	117	0.05	U	2.2	21.96	U - R	0.01	3.3	39.2
			R	2.1	20.43	R	0.00	3.5	166.0
			B	2.4	21.81	B - R	0.01	4.0	165.3
NGC 4649	82	0.15	U	2.9	21.04	U - R	0.01	6.7	102.6
			R	2.0	20.29	R	0.00	3 .1	185.0
			B	2.4	21.76	B - R	0.01	4.8	167.8
NGC 4697	94.5	0.39	U	2.9	20.92	U - R	0.01	7.0	104.2
			R	1.7	20.37	R	0.00	2.2	188.0
			B	2.2	21.89	B - R	0.02	5.6	153.1
NGC 4874	66.5	0.07	U	2.2	21.51	U - R	0.02	5.6	126.5
			R	2.1	20.67	R	0.02	3.4	91.8
			B	2.1	22.52	B - R	0.10	3.4	51.8
NGC 4889	39	0.35	U	2.1	22.12	U - R	0.07	3.4	35.4
			R	2.7	20.54	R	0.02	3.6	122.2
			B	2.5	22.25	B - R	0.10	3.6	75.8
NGC 5638	29.5	0.10	U	2.7	21.83	U - R	0.07	3.6	51.8
			R	1.7	21.07	R	0.00	2.8	80.0
			B	2.0	21.59	B - R	0.02	3.4	54.0
NGC 5813	56	0.23	U	2.2	21.20	U - R	0.02	4.0	49.1
			R	1.9	20.85	R	0.02	2 .8	173.0

TABLE III. (continued)

Galaxy (1)	r_e ″ (2)	ϵ at 10″ (3)	Band (4)	Seeing ″ (5)	Sky (6)	Profile (7)	Ext. + K Correction (8)	Inner Cutoff (9)	Outer Cutoff (10)
			B	1.9	22.28	B - R	0.04	2.8	122.2
			U	2.0	21.79	U - R	0.05	2.9	76.0
NGC 5831	28	0.28	R	1.7	20.71	R	0.02	2.4	91.8
			B	1.8	22.09	B - R	0.04	2.6	58.5
			U	2.0	21.84	U - R	0.05	2.9	48.4
NGC 5845	4.55	0.35	R	1.6	20.76	R	0.03	2.4	36.1
			B	1.6	22.33	B - R	0.04	2.4	27.1
			U	2.3	21.94	U - R	0.04	3.7	20.4
IC 1101	114.5	0.44	R	2.1	21.06	R	0.08	2.5	76.0
			B	2.2	22.61	B - R	0.30	2.7	30.1
			U	1.8	22.09	U - R	0.23	4.1	27.4
NGC 6051	25.5	0.29	R	2.0	20.95	R	0.06	2.9	60.0
			B	2.1	22.56	B - R	0.15	3.0	55.0
			U	2.3	21.91	U - R	0.13	3.3	33.5
NGC 6086	25	0.30	R	1.6	21.19	R	0.06	2.2	92.0
			B	1.5	22.55	B - R	0.15	2.2	47.1
			U	1.5	21.98	U - R	0.13	2.2	26.6
NGC 6269	47.5*	0.25	R	2.2	20.77	R	0.08	3.2	85.1
			B	2.6	22.18	B - R	0.18	4.4	48.0
			U	1.5	21.49	U - R	0.17	6.2	24.6
NGC 7626	41.5	0.12	R	2.0	20.23	R	0.04	3.2	91.8
			B	2.1	21.99	B - R	0.04	3.4	62.7
			U	2.1	21.19	U - R	0.03	3.4	38.9

Notes to TABLE III

Column (2) gives the effective radius from Burstein *et al.* (1987), and where indicated by *, from the RC2. The Burstein *et al.* value has been transformed to major axis effective radii, using ellipticities in column (3) that were measured from the data. Column (5) lists the FWHM of the seeing in arcseconds, and column (6) the surface brightness of the sky in mag arcsec^{-2}. Column (8) gives the correction for galactic extinction and redshift together, applied to the R, $B-R$ and $U-R$ profiles. Columns (9) and (10) list the inner and outer cutoff radius used in the tabulation and presentation of the data. These radii were derived from the measured seeing and sky background level, as discussed in the text. For a few galaxies the data were of poor quality and/or the galaxy was limited by the frame size to higher surface brightnesses than normally used for the cutoff. For these we truncated the profiles at the outer radii shown below:

Galaxy	Color cutoff (% of sky)	Outer cutoff (% of sky)
NGC 1600	15	10
NGC 4261	20	10
NGC 4406	20	10
NGC 4874	20	10

are not at all exceptional for ellipticals, even though the amplitude of such terms is quite small. Typically they have amplitudes of 0.5%. Four examples of model galaxy isophotes with 3θ and 4θ terms of amplitude 0.05 (10×typical) are shown in Fig. 1 for an E4 elliptical. The reason for the characterization of the 4θ terms as "boxy" (negative) or "disk-like" (positive) are clear from the figure.

The accurate determination of the 3θ and 4θ terms requires higher S/N data than is needed for luminosity, ellipticity, and position angle profiles. For some galaxies, especially the cD's, the amplitudes of these terms are rather uncertain, as can be inferred from the scatter in the values at neighboring radii. This was particularly true of the determination of these terms from the U-band data; as a result, the 3θ and 4θ terms are not shown for the U data.

A subjective quality parameter was assigned to the data of each galaxy. Quality parameter 1 was assigned to those surface brightness measurements with low internal scatter that reproduced well in multiple observations. A few of the fainter galaxies (of low apparent magnitude) could be measured over only a limited radius range due to the poor seeing and/or poor signal-to-noise; these galaxies were assigned quality parameter 3. Intermediate cases were assigned quality 2. These quality parameters are given in Table II. A more direct assessment of the quality of the data can be obtained by inspection of the results in Fig. 15 (Appendix A).

b) Sky Subtraction

Most galaxies were sufficiently small that we could measure the sky directly from the galaxy frame. We applied the "boxes" method from Paper I, wherein the pixels in small arrays near the corners were averaged to give a sky estimate. The global average of the arrays was taken to be the sky for that frame. For a number of larger galaxies this method did not work very well, since the galaxy itself was still detectable at the edges of the frame. These galaxies were NGC 2768, 3377, 3379, 4374, 4406, 4472, 4486, 4636, 4649, and 4697.

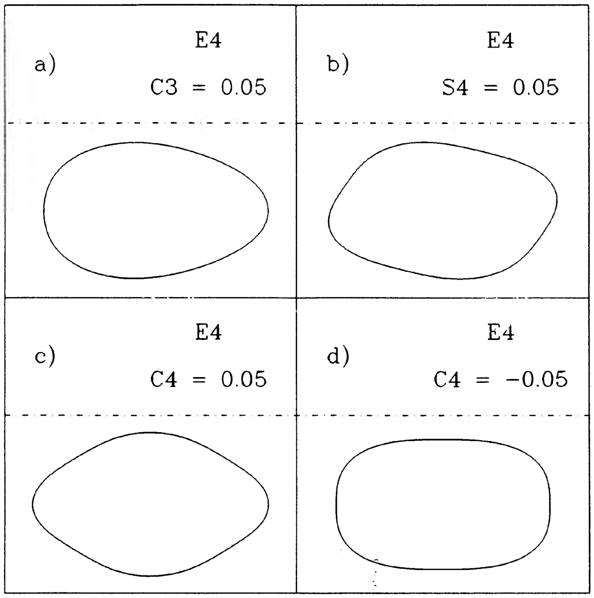

FIG. 1. Isophotes of model galaxies with nonzero high-order Fourier terms. Several E4 model ellipticals are shown with 3θ and 4θ terms with an amplitude 0.05 (10×typical) added to the model. (a) has threefold symmetry from the addition of a positive $\cos 3\theta$ term; (b)–(d) show fourfold symmetry from added positive $\sin 4\theta$ [in (b)], added positive $\cos 4\theta$ [in (c)], and added negative $\cos 4\theta$ [in (d)]. The shape in (c) is characteristic of a major- or minor-axis disk, while that in (d) is characteristic of "boxy" isophotes.

Since the 0.9 m field was 7.5′×4.5′, and some large galaxies were offset from the center of the frame, the galaxy contribution at the edges was only a few percent of sky. For these large galaxies we used the "boxes" method to get an initial value of sky. This value was then corrected slightly so that the luminosity profile in the outer parts fell off with the same slope as that in the intermediate regions.

To assess the accuracy of our sky estimates we compared the profiles for the twelve galaxies with data from both the 0.9 and the 2.1 m telescopes. The "boxes" method, with its correction from the luminosity profile when needed, was applied independently to both 0.9 and 2.1 m frames, after which the sky-subtracted profiles were compared. The radius at which sky could be determined on the 2.1 m was about half as large as on the 0.9 m. We found that no adjustment of the 2.1 m sky level was necessary for six of the galaxies; the 0.9 and 2.1 m profiles agreed.

Of the remainder, four required a decrease in 2.1 m sky estimate of about 1%. NGC 4374 and NGC 5813 are so large that the galaxy was contributing more than 5% of the level of sky at the edge of the 2.1 m frame. Even for these large galaxies the contribution of the galaxy at the edge of the 0.9 m frame was only of the order of 1% of sky. After correction the sky values should be determined to this level or better. To summarize, we expect, conservatively, that for our best data (those galaxies with quality parameter 1) the uncertainty in sky to be approximately 1%. For the very large galaxies (listed above) the error could be as large as 2%.

An additional diagnostic for sky (and flat field) problems is the position of the center of the galaxy. Position angle shifts found were very small or nonexistent, being < 0.5 pixel on the 0.9 m telescope, and even less on the 2.1 m, suggesting that both sky problems and other effects are minimal.

The profiles determined from the 0.9 and 2.1 m telescope data are compared in Fig. 2 (after adjustment of the 2.1 m sky values). We have applied an inner radial cutoff, to account for uncertainty introduced by the effects of seeing (see Sec. IV). The cutoff was based on the best seeing, so the effects of the poorer seeing frames (usually from the 0.9 m telescope) are still visible. For each galaxy the best 2.1 m frame was subtracted from the best 0.9 m frame, after correcting the 2.1 m sky background. The dominant source of noise in these comparisons is the 0.9 m data. For some galaxies, for which the 0.9 m data is poor (e.g., NGC 6086 and NGC 6269) the comparisons show large scatter. Differences in the *U* band have the largest amplitude, because the signal in *U* is the smallest on both telescopes.

The repeatability of the data between the two telescopes suggests that it is not subject to systematic errors such as internal scattered light and reflections within the instrument (from filters, detector, detector support, etc.). The different scales at the 0.9 and 2.1 m would lead to quite different contributions at a given radius.

We also checked whether our profiles reproduced from frame to frame. Frames with different exposure times were processed independently, both for the luminosity profile and the sky level. Differences in the profiles were less than 0.02 mag within the outer cutoff, except in the center where seeing effects dominated.

We have truncated the luminosity profiles at a surface brightness of 10% of the sky background. This level was chosen since our typical uncertainty of 1% in the sky level results in a 10% error (i.e., ±0.1 mag) at the cutoff radius. Similarly, we truncated the color profiles at the smaller of the radii from the two bands at which the surface brightness reached 10% of the level of sky. If the percentage of sky at the same radius was comparable in both bands, we truncated the color profiles at the radius at which the total error in the color profile was 10%. Table III gives these outer cutoffs for the *R* luminosity profile and the color profiles, together with the inner cutoffs derived as discussed in Sec. IV.

While uncertainties in the sky remain as a potential source of systematic error, we feel that we have done as well as can reasonably be done with the small CCDs available to date. The data are clearly valuable, even with this concern about the sky. Future studies with large detectors will show whether this confidence is misplaced or not.

Finally, the seeing was measured on each frame from three or four stars, when available. The GASP PROF and CUTS routines (see Paper I) were also used to derive the seeing profiles. The FWHM for the seeing are given in Table III. Note that the 2.1 m data had better seeing than the 0.9 m data; the *U* seeing is generally worse than that for the *B* and *R* data, especially on the 0.9 m.

c) Rebinning and Photometric Calibration

After sky subtraction the data were rebinned in radius and weighted averages of the profiles in each band were generated. Weight factors were directly proportional to integration times; the better seeing and sampling of the 2.1 m telescope meant that in general these data along were used for the galaxy centers. The data were rebinned in radius such as to make the data points independent. Each data point was weighted by the area of its associated annulus. When inter-

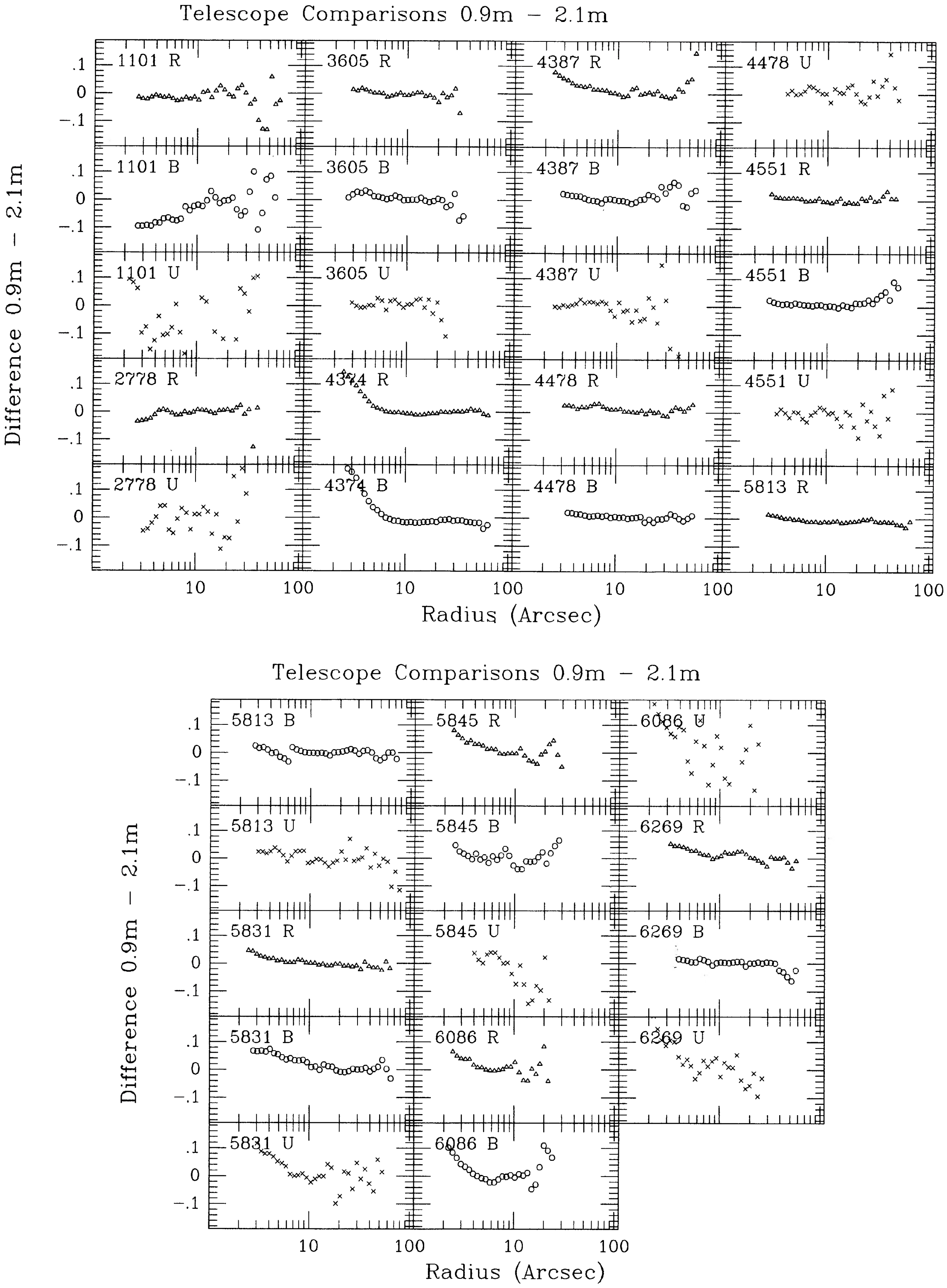

FIG. 2. Comparison of the profiles from the 0.9 and the 2.1 m data, after correction of the 2.1 m sky levels. The profiles have been limited to the radial range set by the 2.1 m seeing at small radii (Sec. V) and the sky uncertainty at large radii (Sec. III*b*). Some seeing effects from the 0.9 m are apparent. The *U* data are crosses, the *B* data are open circles, and the *R* data are open triangles.

polation was necessary a fifth-order polynomial was used with no loss of information since the profiles were well sampled in radius.

Systematic differences in scale between the images in the three bands could have caused systematic errors in the measured color gradients. In Paper I we showed that scale differences at the No. 1 0.9 m were insignificant. The scale differences were determined again by measuring the accurate positions of stars on glass copies of the Palomar Sky Survey for ≈ 20 galaxies using the Sony measuring machine at the Sterrewacht, Leiden. No significant differences from unity were found at either telescope (typical uncertainties were ± 0.002).

We found small, but systematic offsets in position angle for the same galaxy observed during different runs. These differences were typically 1–2°, but were sometimes 4–5°. We attribute these differences to small changes from run to run in the orientation of the dewar on the telescope. By measuring stars on the CCD frames and on the Palomar Sky Survey plates all position angle measurements have been corrected and are given from north through east.

To provide an absolute calibration for the profiles (i.e., to transform CCD counts to magnitudes on the Cousins UBR_C system), we used published aperture photometry from Burstein *et al.* (1987) for 30 galaxies and the catalogs of Longo and de Vaucouleurs (1983, 1985) for the remainder. The data used from the latter catalogs came primarily from Sandage and Visvanathan (1978) and Persson, Frogel, and Aaronson (1979). The transformations used are given in Paper I. For IC 1101 no published aperture photometry was available in any band, nor for NGC 2778 and NGC 5845 in U, and so we used the calibration from other galaxies that were observed on the same night. For galaxies for which the Burstein *et al.* tabulated colors are given as $V-R_J$, we derived $V-R_C$ values by using the transformation

$$V-R_C = 0.73(V-R_J) - 0.03,$$

from Bessel (1979). For galaxies for which $V-R$ was not available, we used the mean $(V-R_J)-(B-V)$ relation for ellipticals from Burstein *et al.* and the transformation above to give

$$V-R_C = 0.613(B-V) + 0.021.$$

From the scatter in the aperture measures for individual galaxies we estimate that this transformation did not introduce errors larger than 0.03 mag. From the internal scatter in the aperture measurements, we estimate that an accuracy of the zero point of ± 0.1 mag in U, B, and R is realistic. Since our main goal is to measure luminosity and color profiles, an accurate zero point is desirable, but not essential.

Galactic extinction and K corrections were dealt with in the same way as described in Paper I. Reddening corrections (from Persson *et al.* 1979) are of the form $A_V = 0.1(\mathrm{cosec}|b| - 1)$, $b < 50°$, $A_V = 3.05E_{B-V}$, $E_{U-V} = 1.71E_{B-V}$, and $E_{V-R} = 0.80E_{B-V}$. The K corrections (from Whitford 1971) were determined from $\Delta V = 2z$, $\Delta(U-V) = 2z$, $\Delta(B-V) = 3z$, and $\Delta(V-R) = -z$, where z is the redshift of the galaxy. These corrections have been applied to both the plotted and tabulated data.

IV. SEEING SIMULATIONS

Previous studies of the effects of seeing on galaxy profiles (Schweizer 1979, 1981; Djorgovski 1983; Lauer 1985) have emphasized the way in which seeing modifies core parameters. The goal of these studies has been to derive the true parameter values by generating corrections to the seeing-convolved parameters. The seeing in our data was generally not good enough to make such an approach fruitful. Here we investigate the effects of seeing on the profiles to establish the radius beyond which they are accurate (until sky errors become a major factor). We simulated galaxies with a de Vaucouleurs $r^{1/4}$ law luminosity profile and a range of constant ellipticities to determine the radii beyond which the error due to seeing is $\Delta m < 0.05$ mag for the luminosity and color profiles, and beyond which the ellipticity error $\Delta\epsilon < 0.02$. Elliptical galaxies are rarely as centrally concentrated as an $r^{1/4}$ law, and so this approach is likely to generate a conservative (upper limit) radius beyond which the profile should be accurate to the above tolerances. The simulated images were convolved with Gaussian seeing profiles covering the range of seeing-to-galaxy length-scale ratios present in the data. A seeing profile with exponential wings (as in Schweizer 1979) was also tried and produced results which were rather similar; the effects of different point-spread functions (PSFs) have been explored by the authors quoted above.

PROF was run on these simulation frames to measure luminosity and ellipticity profiles. These were then compared with the original profiles to assess the effect of seeing on the luminosity profile. Comparisons between profiles measured from galaxy models convolved with different seeing values were made to assess the effect of seeing on the color profiles. We assumed no intrinsic color gradient for the purposes of this simulation. This assumption is reasonable since the magnitude of the color gradients, even over a factor 10 in radius, is small. Seeing redistributes the light in the center of the galaxy from small radii to larger radii, reducing the central surface brightness and correspondingly increasing the surface brightness at intermediate radii, beyond which the profiles become identical. We then measured the major axis radius beyond which the difference between the original and the seeing-convolved profiles was smaller than the above limits (i.e., $\Delta m < 0.05$ mag and $\Delta\epsilon < 0.02$).

The results can be seen in Figs. 3(a)–3(c). The radii at which the effects of seeing become less than the adopted limits of $\Delta\epsilon = 0.02$, $\Delta m_L = 0.05$ and $\Delta m_C = 0.05$ are plotted against the seeing. Both the radii and the seeing are normalized by the galaxies effective radius r_e. D_s is the seeing FWHM in Fig. 3(a) and 3(b), and the smaller of the two seeing FWHM in Fig. 3(c), while D_L is the larger of the seeing FWHM. D_e is the effective diameter (twice the effective radius along the major axis). The radius cutoffs are shown for a range of ellipticities. These figures demonstrate that:

(1) The major-axis luminosity profiles are affected more by seeing when the ellipticity is low than when the ellipticity is high. This is because there is less light off the major axis in an elongated galaxy than in circular one, to "contaminate" the light on the major axis.

(2) Ellipticity profiles are affected more when the ellipticity is high. The radial extent over which seeing affects the ellipticity is much larger than we had expected.

(3) The error in the color profile caused by seeing arises predominantly from the frame with the poorer seeing; the error is small if the seeing in both frames is the same, but initially varies rapidly as D_S/D_L decreases from unity.

If we take a King model instead of an $r^{1/4}$ law, the effect of seeing depends on the core radius of the King model. For

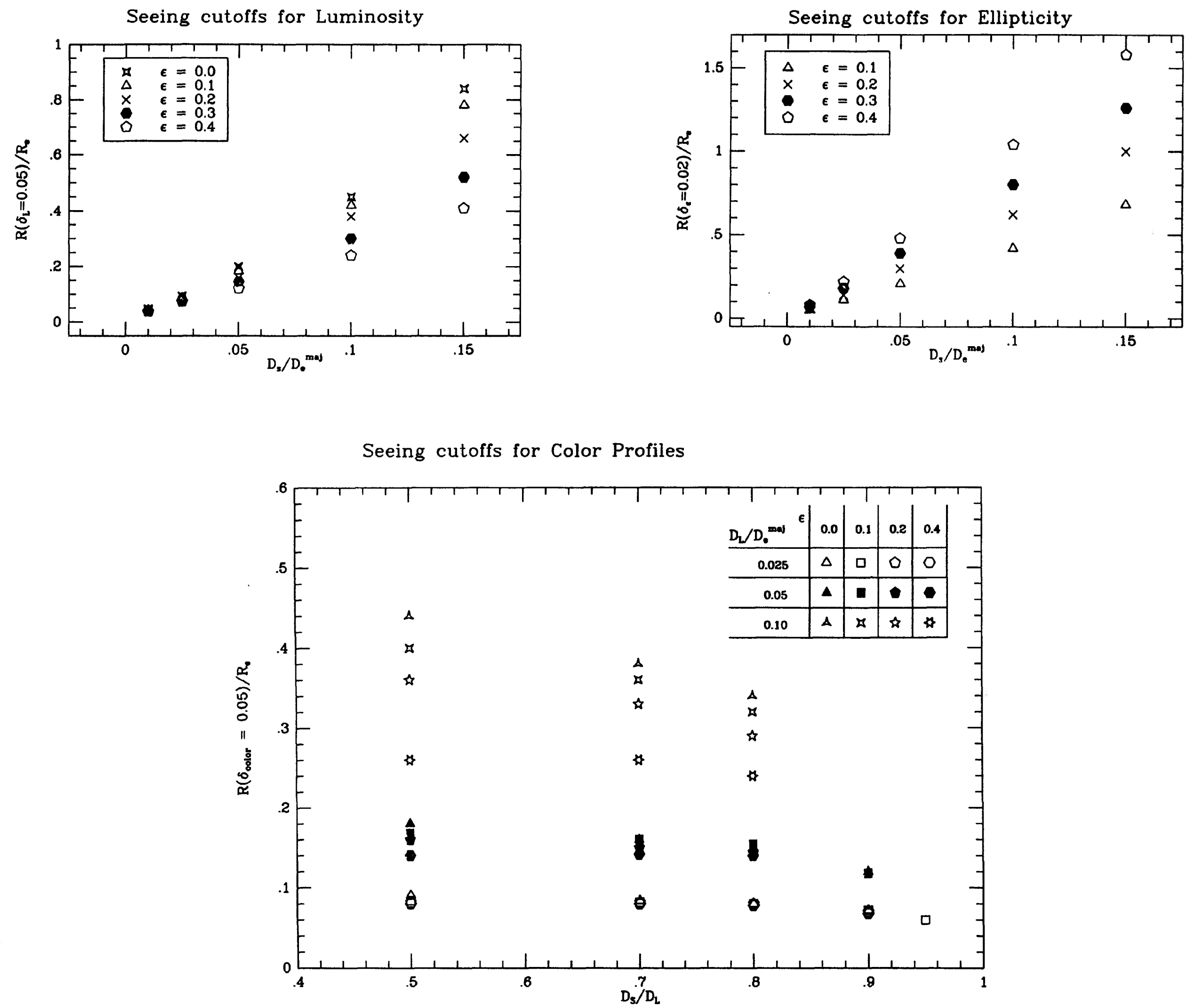

FIG. 3. Seeing cutoffs from simulations where model galaxies were convolved with Gaussian seeing point-spread functions (PSFs) for a range of ellipticities ϵ. The cutoff radii are normalized to r_e and are determined to be those beyond which the error from seeing effects on a $r^{1/4}$ law profile are (a) <0.05 mag in the surface brightness profile, (b) <0.02 in the ellipticity, and (c) <0.05 mag in the color profile. D_S is the seeing PSF FWHM in (a) and (b), and the smaller of the two seeing FWHM in (c), while D_L is the FWHM of the larger seeing PSF. D_e is the effective diameter (twice the effective radius r_e along the major axis).

core radii much smaller than the seeing radius, the results are similar to that for an $r^{1/4}$ law profile. As expected, for core radii much larger than the seeing any effect is small. When the core and seeing radii are comparable the King model fit is perturbed less than the $r^{1/4}$ law fit, since the former is less centrally concentrated and less light is available to be redistributed.

We have assumed that there is no intrinsic color gradient. Then, if the seeing in both bands is almost equal, the error resulting from the seeing in the color profile is smaller than that in either luminosity profile, because both errors almost cancel each other. For this reason, we have determined independently the radii outside which the error in the color profile is smaller than 0.05 mag. The color profile for a galaxy with no intrinsic color gradient derived from frames taken under different seeing conditions will not be constant. Seeing redistributes the light in the inner parts to larger radii. The larger the seeing, the more light is redistributed from the center. So if one subtracts the profile from the frame with the best seeing from the worst seeing case, the "color profile" is negative at the center, rises through zero to a maximum, and asymptotically returns to zero. If the maximum is larger than 0.05, there are two regions where the absolute difference is smaller than 0.05 mag: at large radii, and near the point at small radii where the profiles cross one another before separating at still smaller radii. If the maximum positive difference is greater than our chosen tolerance, namely 0.05 mag, there will be two points where the locus of the difference crosses the value + 0.05 and one, at a small radius, where the locus crosses the value − 0.05 mag.

In Fig. 3(c), we show the radius beyond which the luminosity profile of the frame with the poorer seeing is less than 0.05 mag brighter than the frame with the better seeing. We have used only the most conservative prescription in generating Fig. 3(c), so that once the maximum positive difference falls below 0.05 mag, no symbol is plotted. Note that for round galaxies the plotted radius is larger than for flattened ones. For galaxies with nonzero color gradients, the error in the color profile will not converge to zero if both seeings are equal.

We applied the results from these simulations to our galaxies, and determined the radius beyond which the profiles were essentially unaffected by seeing. The effective diameters needed for this were taken from Burstein *et al.* (1987), and converted to major-axis effective diameters. The central ellipticity was taken to be that at $\approx 10''$, beyond the worst effects of the seeing. In Table III we present this ellipticity and the effective radii. With these values and our seeing estimates we determined the inner cutoff radii for the surface brightness, ellipticity and the color profiles by interpolating across the values from the simulations. To avoid large errors caused by interpolating near $D_S/D_e = 0$, effective diameters larger than 100″ were truncated to 100″. The radial cutoffs determined from the simulations have been applied to the final tabulated and plotted data in Table IX and Fig. 15 in Appendix A.

The simulations show that the ellipticity is significantly affected by seeing out to quite large radii. As a result we have tabulated values for the ellipticity from half the inner cutoff radius determined from the simulations. For some highly flattened galaxies the ellipticity appears to decrease in the center. For example, in NGC 3377 and NGC 4697 the ellipticity decreases monotonically at radii less than 10 arcsec. The simulations show that this entire effect can be attributed to the seeing and that the data are consistent with the ellipticity remaining constant at the value observed at radii greater than 10 arcsec (see Fig. 4 where the results for NGC 3377 and NGC 4697 are shown). We caution the reader that the ellipticities are accurate to 0.02 only beyond radii that are twice as large as those for the first ϵ value in Table VII. The error in the position angle increases $\propto 1/\epsilon$ as the ellipticity tends to zero, and so can become very large (an example of a galaxy subject to this effect would be NGC 4486).

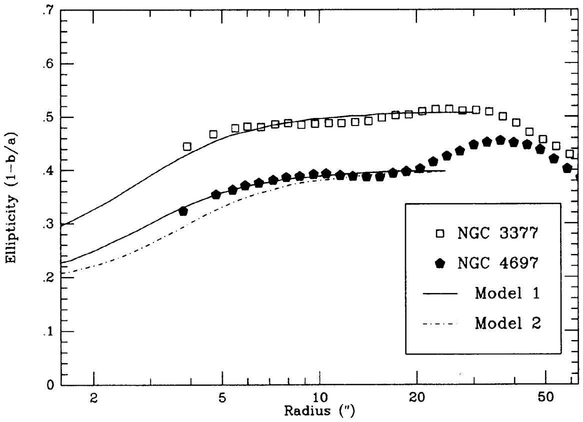

FIG. 4. Ellipticity profiles for NGC 3377 and NGC 4697 in *R*. No radius cutoffs have been applied. Model profiles are overlaid. They are derived from a galaxy with a de Vaucouleurs luminosity profile and a fixed ellipticity, convolved with circular Gaussian seeing. For the effective radii we took the values from Table III for NGC 3377 and for model I for NGC 4697, and set $r_e = 50''$ for NGC 4697 for model 2. The figure shows that the decrease in the ellipticity into the core is consistent with a constant ellipticity profile degraded by the seeing.

Franx, Illingworth, and Heckman (1989b) give analytic formulas for errors in the photometric parameters, calculated by using a few terms of the Taylor expansion of the intensity profile that is convolved with a noncircular seeing profile. They note, in particular, the effect of a noncircularly symmetric seeing point-spread function on the position angles for round galaxies. Their main conclusions agree with the results of our simulations.

V. RESULTS AND COMPARISONS WITH OTHER STUDIES

The results from this program are shown and tabulated fully in Appendix A. The *R*-band surface brightness profile plus the ellipticity and major-axis position angles profiles in *U*, *B*, and *R*, as well as the $B - R$ and $U - R$ color gradients, are tabulated (Table IX) and plotted (Fig. 15) there for each of the 39 galaxies in our sample. In addition, the sin and cos 3θ and 4θ terms are also plotted in Fig. 15. Specific comments on individual galaxies are given in Appendix B for characteristics that are distinct from the norm.

In order to characterize the properties of these galaxies from the surface photometry, we have calculated "effective" of "characteristic" parameters for each galaxy. We have derived logarithmic gradients for the color, ellipticity, and position angle profiles, i.e, we have made a linear regression of these parameters on the logarithm of the radius. We have used all the data values within the inner and outer cutoff radii. The color profiles are well represented by a linear fit against log radius, and so can be characterized quite accurately by such a relation. This is less true of the ellipticity and position angle profiles. However, the logarithmic gradients of ϵ and θ are a useful characterization for the purpose of correlations between the parameters and so are given here. The limitation of such a representation should be kept in mind. The gradients are weighted somewhat towards changes near the core, since there are more data points in the inner regions. The logarithmic gradients are given in Table IV, together with the fitted values at $r = r_e/2$.

a) Comparison with other Studies: Luminosity Profiles and Isophote Shapes

The surface photometry of the three galaxies presented in Paper I was compared extensively with the results of other authors to establish the validity of the techniques used. For this sample we have chosen not to compare our results with all the available surface photometry in the literature, but only with a number of studies that present large bodies of data. We have compared our results with those of King (1978, hereafter referred to as KI), Michard (1985, hereafter referred to as MI), Kent (1984, hereafter referred to as KE), Djorgovski (1985, hereafter referred to as DJ), Lauer, (1985, hereafter referred to as LA), and Jedrzejewski (1987, hereafter referred to as JE); the first two authors worked with photographic data, while the last four authors used CCDs. The comparisons were made between the major-axis surface brightness profiles using our data in the band closest to the above author's published band. DJ and LA used an *R* band with a larger effective wavelength than used by us; KE used the Gunn *R* band, which is narrower than Cousins *R*, but has the same effective wavelength. JE worked in Johnson *B* and *R*. We have compared the photographic magnitudes of KI and MI with our *B* measurements. For comparison with the KI and MI data we corrected our profiles to correspond to their 45° profiles. The photographic data are valu-

TABLE IV. Characteristic parameters.

Galaxy (1)	ϵ (2)	$\frac{\Delta(\epsilon)}{\Delta \log r}$ (3)	ϕ (4)	$\frac{\Delta(\phi)}{\Delta \log r}$ (5)	B-R (6)	$\frac{\Delta(B-R)}{\Delta \log r}$ (7)	± (8)	U-R (9)	$\frac{\Delta(U-R)}{\Delta \log r}$ (10)	± (11)
NGC 315	0.26	-0.005	43.8	1.9	1.76	-0.06	0.04	2.37	-0.14	0.09
NGC 720	0.40	0.154	141.7	-0.5	1.58	-0.09	0.02	2.10	-0.31	0.05
NGC 741	0.17	0.069	90.4	4.2	1.46	-0.14	0.05	2.13	-0.40	0.16
NGC 1052	0.27	0.017	114.8	5.5	1.61	-0.11	0.02	2.17	-0.28	0.02
NGC 1129	0.21	0.154	57.7	73.0	1.52	-0.09	0.07	2.15	-0.11	0.06
NGC 1600	0.34	-0.006	7.2	0.6	1.54	-0.02	0.02	2.17	-0.21	0.06
Abell 496	0.28	0.151	172.6	7.7	1.52	-0.12	0.09	2.09	-0.17	0.10
NGC 2300	0.19	0.074	78.0	8.0	1.62	-0.13	0.05	2.27	-0.33	0.12
NGC 2768	0.47	0.243	93.8	-2.8	1.40	-0.09	0.01	2.04	-0.29	0.06
NGC 2778	0.21	0.014	44.3	-3.5	1.77	-0.08	0.03	2.08	-0.21	0.03
NGC 2832	0.30	0.202	158.9	5.1	1.42	-0.14	0.04	1.97	-0.27	0.05
NGC 3377	0.47	-0.049	39.4	1.3	1.51	-0.09	0.01	1.97	-0.33	0.03
NGC 3379	0.10	0.049	71.0	0.4	1.59	-0.05	0.01	2.18	-0.24	0.01
NGC 3605	0.37	0.142	18.6	-0.7	1.41	-0.03	0.02	1.80	-0.09	0.04
NGC 3665	0.24	-0.059	27.7	6.6	1.52	-0.12	0.02	2.03	-0.16	0.03
NGC 3801	0.37	0.189	121.1	0.6	1.52	-0.43	0.10	1.97	-0.81	0.15
NGC 4261	0.20	-0.058	159.5	1.3	1.60	-0.08	0.03	2.15	-0.24	0.05
NGC 4278	0.12	-0.037	22.7	16.7	1.57	-0.15	0.01	2.00	-0.40	0.05
NGC 4374	0.12	-0.106	128.8	0.7	1.60	-0.06	0.02	2.14	-0.23	0.01
NGC 4387	0.35	0.080	141.1	2.3	1.63	-0.04	0.01	2.12	-0.05	0.02
NGC 4406	0.24	0.102	121.1	-2.0	1.56	-0.03	0.02	2.08	-0.18	0.02
NGC 4472	0.17	0.063	159.2	-5.1	1.63	-0.05	0.02	2.17	-0.20	0.04
NGC 4478	0.17	-0.002	146.3	-12.6	1.55	-0.03	0.03	2.07	-0.15	0.05
NGC 4486	0.09	0.075	159.9	0.0	1.62	-0.07	0.02	2.03	-0.30	0.05
NGC 4551	0.25	0.048	68.7	1.7	1.55	-0.01	0.02	2.12	-0.02	0.02
NGC 4636	0.20	0.178	149.3	-11.7	1.54	-0.08	0.02	2.00	-0.30	0.05
NGC 4649	0.18	0.093	103.8	5.1	1.62	-0.06	0.02	2.27	-0.21	0.03
NGC 4697	0.37	-0.033	67.4	1.1	1.51	-0.08	0.02	1.97	-0.26	0.04
NGC 4874	0.09	0.030	39.7	18.5	1.50	-0.17	0.05	2.05	-0.24	0.07
NGC 4889	0.32	0.105	78.4	2.2	1.47	-0.11	0.04	2.19	-0.19	0.04
NGC 5638	0.09	0.069	144.8	11.9	1.56	-0.06	0.02	1.82	-0.25	0.05
NGC 5813	0.20	0.177	137.2	-11.4	1.59	-0.05	0.02	2.21	-0.10	0.03
NGC 5831	0.19	-0.165	124.0	25.3	1.63	-0.08	0.02	2.11	-0.18	0.03
NGC 5845	0.25	0.085	147.6	-9.6	1.68	-0.10	0.02	2.45	-0.09	0.02
IC 1101	0.43	0.279	23.1	7.0	1.53	-0.09	0.09	2.22	-0.14	0.11
NGC 6051	0.29	0.184	165.2	0.5	1.73	-0.13	0.07	2.43	-0.03	0.05
NGC 6086	0.31	0.116	3.3	4.5	1.50	-0.04	0.05	2.12	-0.19	0.06
NGC 6269	0.27	0.040	78.8	-5.2	1.57	-0.14	0.07	2.25	-0.18	0.12
NGC 7626	0.14	0.085	9.6	8.8	1.69	-0.03	0.04	2.23	-0.21	0.07

Notes to TABLE IV

This table presents global parameters derived from the data presented in Table 2.9. We have fitted linear relations to ellipticity, position angle, $B-R$ and $U-R$ as a function of the logarithm of radius. The slope and intercept of these logarithmic gradients are given, with the intercepts being derived for $r = r_e/2$. In columns (2) and (3) we present the fits for the ellipticity $1 - b/a$, in columns (4) and (5) those for the position angle of the major axis, in columns (6), (7), and (8) the logarithmic gradient for the $B-R$ color, and in columns (9), (10), and (11) that for the $U-R$ color gradient. The color gradients are given in mag arcsec^{-2} per dex in radius.

able as a check on the sky subtraction process since they typically extend to large radii. The nonlinearity of photographic emulsions is less of a concern at low surface brightnesses.

The bands were sufficiently close and the color gradients in ellipticals small enough that no corrections were necessary before comparison. No correction was made for the zero-point difference that is typically $R_C - R_J = 0.25$ mag (see Paper I).

The comparisons in B are shown in Fig. 5(a) and those in R are shown in Fig. 5(b). Some aspects of these comparisons are noteworthy. In the R band, agreement with LA and KE is excellent; any trend present in the data appears to be $\leqslant 0.1$ mag arcsec^{-2} over the radial extent of the data. The sense of the differences is random, and the zero points are different in a way that is consistent with the different filter combinations used. The R data of JE exhibit surface brightness gradients which are systematically less steep than our profiles; his galaxies always appear too bright in the outer parts. The effect is unlike that expected from a systematic error in sky background level, since it extends smoothly to small radii. The R differences are also too large to be caused by the different R filter.

We have performed a linear regression on the difference profile in magnitudes as a function of log radius (excluding the three galaxies where the difference does appear to be due

1990AJ....100.1091P

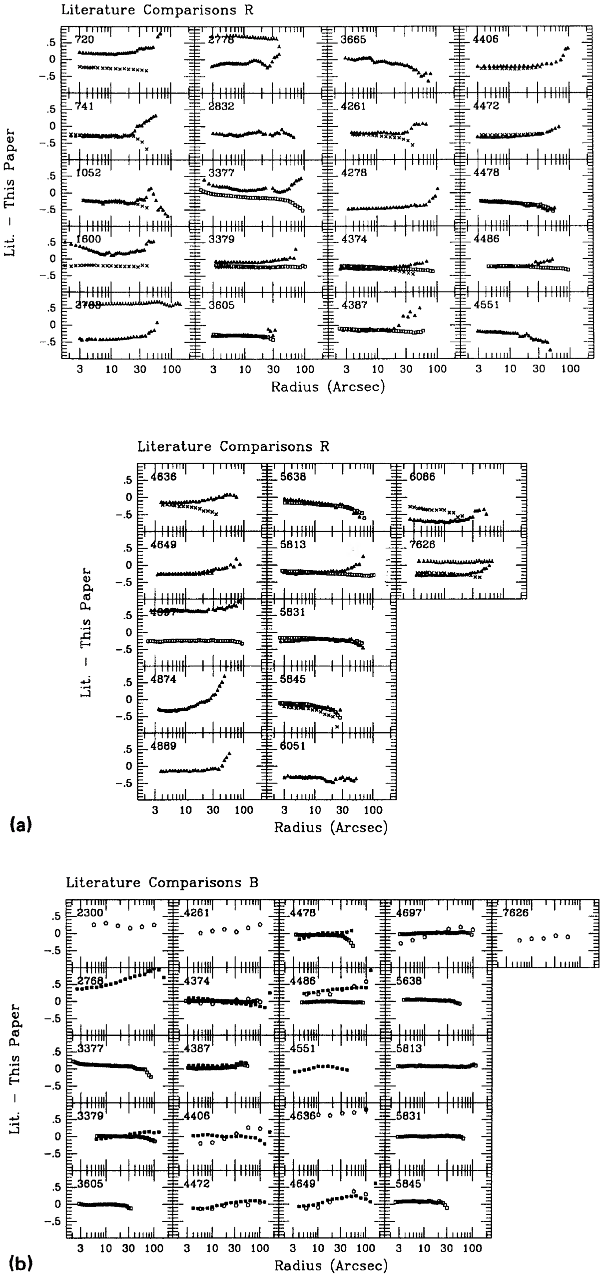

FIG. 5. Comparisons with other authors over the range defined by our cutoff radii. *R* data are used in (a), and *B* data in (b). The sources corresponding to the symbols are: open pentagons—(King 1978); open squares—(Jedrzejewski 1987); open triangles—(Kent 1984); filled squares—(Michard 1985); filled triangles—(Djorgovski 1985); crosses—(Lauer 1985). Corrections have *not* been applied for zero-point differences.

to uncertainties in the sky, i.e., NGC 3377, NGC 5638, and NGC 5845), and find a systematically smaller gradient in the JE data of 0.07 ± 0.01 mag per dex in radius. In *B* the agreement with JE is good; the regression yields a formally insignificant result.

The data of DJ were obtained using the same equipment as the data of LA, but extend to larger radii. In general, DJ reports fainter surface brightness than both we and LA find at these large radii. It seems likely that the sky background values of many of the galaxies reported by DJ have been overestimated. In many cases the galaxies filled the field of his CCD, which could have led him to overestimate the brightness of the sky. In this case, one might expect the most discrepant galaxies to be the large ones, and the smaller ones to be in better agreement; this does not appear to be uniformly true. With the exception of NGC 2768, for which there is a large difference with the data of MI, the comparisons with KI and MI show that our respective datasets agree well. The problem with NGC 2768 may be due to its large ellipticity and the derivation of the 45° profile in the presence of large quantities of dust.

The ellipticity and position angle profiles generally agree quite well. The differences with LA, for example, are small, usually being within 0.02° and 2°, respectively. Differences with DJ are often larger, and systematic in a few cases.

Other authors (e.g., Carter 1978, 1987; Lauer 1985; Bender and Möllenhoff 1987; Bender *et al.* 1988) have also derived higher-order terms, though typically they have taken a more limited approach and have just derived the cos 4θ term, and sometimes the cos 3θ term. Our sin and cos $n\theta$ profiles agree well with those in the previous references.

The high-order terms in Table V were determined by averaging several values around the maximum amplitude. We have also tabulated the radius of the peak for the cos 4θ term (C4), since this is the term that has attracted the most interest because of its probable correlation with other properties of the galaxies.

The C4 values were compared with those from Bender *et al.* (1989). Figure 6 shows that the agreement is excellent. Bender *et al.* use a slightly different definition, with different normalization: if there is a maximum (or minimum), they select the peak value, as we do, but if the profile is monotonically increasing or decreasing, they take the value at one effective radius. However, for the 19 galaxies we have in common, only two have monotonically increasing or decreasing profiles. For this reason we would expect the C4 values to be the same, but on the average our C4 values are systematically larger by ≈40% than theirs. This is presumably a result of the different normalization used.

Franx, Illingworth, and Heckman (1989b) showed that representing the deviations by their phase and amplitude makes it easier, in many cases, to understand the nature of the structure that contributes to the deviations from elliptical isophotes. We show two examples below.

b) Comparison with other Studies: Color Gradients

A number of authors have published color gradients, usually for a small set of galaxies. A comparison with the color profiles of several authors is made in Fig. 7. The results are not encouraging. In general, the agreement is still not as good as one would like. However, the difficulty of measuring color changes of a few percent over a range in surface brightnesses of several decades should not be underestimated. In the mean, most authors with CCD data are consistent, finding small negative gradients in ellipticals, consistent with those found from the concentric aperture measures, and so the reality of gradients of this form is probably well founded, even if individual cases should be treated with some skepti-

TABLE V. Effective higher-order terms.

Galaxy	C3	S3	C4	r_{C4} ″	S4
(1)	(2)	(3)	(4)	(5)	(6)
NGC 315	0.002	-0.001	-0.006	12	-0.002
NGC 720	0.002	-0.001	-0.003	12	-0.004
NGC 741	0.003	0.001	0.002	16	-0.002
NGC 1052	0.003	-0.002	0.000	10	-0.001
NGC 1129	-0.014	0.008	-0.008	22	-0.002
NGC 1600	-0.001	0.000	-0.015	11	-0.002
Abell 496	-0.007	-0.003	0.006	13	0.005
NGC 2300	0.006	0.003	0.011	38	0.003
NGC 2768	0.002	-0.001	0.006	48	0.005
NGC 2778	-0.001	-0.002	-0.003	22	0.000
NGC 2832	0.000	-0.008	-0.004	16	0.008
NGC 3377	0.007	0.002	0.019	6	-0.002
NGC 3379	-0.005	0.003	0.003	16	0.006
NGC 3605	0.002	0.002	-0.012	14	-0.004
NGC 3665	0.002	-0.003	-0.002	50	0.000
NGC 3801	-0.016	-0.012	-0.092	5	0.030
NGC 4261	0.003	-0.004	-0.019	11	0.005
NGC 4278	0.005	-0.011	0.000	-	-0.007
NGC 4374	0.003	0.000	-0.006	14	-0.002
NGC 4387	0.002	-0.001	-0.010	8	-0.005
NGC 4406	0.002	0.000	-0.010	17	-0.004
NGC 4472	-0.001	-0.003	-0.004	20	0.004
NGC 4478	0.002	-0.002	-0.015	25	0.013
NGC 4486	0.001	-0.002	0.001	-	0.001
NGC 4551	-0.003	0.002	-0.011	10	0.002
NGC 4636	-0.002	-0.002	-0.001	4	0.004
NGC 4649	0.004	0.004	-0.005	25	-0.006
NGC 4697	0.001	0.003	0.026	22	0.002
NGC 4874	0.010	0.004	-0.004	45	-0.012
NGC 4889	-0.001	0.001	-0.002	9	0.002
NGC 5638	0.000	0.000	0.001	-	-0.002
NGC 5813	0.002	0.002	0.001	30	-0.002
NGC 5831	0.002	0.001	0.008	16	-0.005
NGC 5845	0.006	-0.002	0.013	10	-0.006
IC 1101	-0.002	0.002	0.002	7	-0.002
NGC 6051	0.001	0.000	-0.002	7	0.002
NGC 6086	0.002	0.003	0.010	25	-0.005
NGC 6269	-0.002	-0.002	0.005	32	0.002
NGC 7626	-0.006	-0.005	0.004	6	0.004

Notes to TABLE V

In columns (2), (3), (4), and (6) we give the C3, S3, C4 and S4 terms, averaged as explained in the text. In column (5) we list the radius at which the maximum or minimum in C4 is reached.

cism. The advantage of the larger sensitivity of $U-R$ is apparent.

Boroson, Thompson, and Shectman (1983) determined color gradients in several bands for NGC 2300, 2768, and 4486 using the drift scan method on the Palomar 60 in. telescope. Comparison of their $B-R_J$ gradients with ours shows that they are consistent in the sense of the offset that results from their use of R_J compared to our R_C. The expected offsets can be determined from the relation given in Paper I, typical color differences are $(B-R)_J-(B-R)_C = 0.25$ mag for galaxies with $(B-R)_C = 1.6$, a little smaller than that seen in the comparison for these three galaxies.

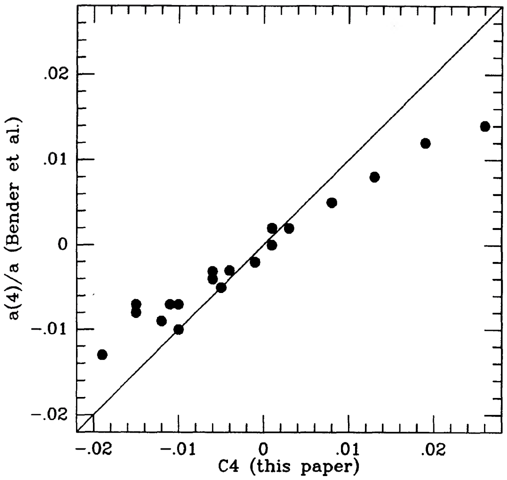

FIG. 6. A comparison between our C4 values and the $a(4)/a$ parameter from Bender *et al.* (1988) for all those galaxies in common between the two samples.

Cohen (1986) determined color gradients for NGC 4406, 4472, and 4486 using the 4-shooter on the Palomar 5 m. She finds small gradients in $g-r$ (Gunn system), which are broadly consistent with what we find. However, her data consistently show a slight reddening at large radii, unlike what is generally seen in our data.

Franx, Illingworth, and Heckman (1989b) obtained color gradients in $B-R$ and $U-R$ for 17 southern elliptical galaxies, using the same general approach, including the same filter system. The range for which they have obtained color gradients is in most cases smaller, since they used detectors with a smaller field. The general trend they see is the same: $B-R$ and $U-R$ both become bluer with increasing radius, with the gradients in $U-R$ being much larger than those in $B-R$. Only one galaxy is common to both samples, i.e., NGC 7626. The error bars on the Franx, Illingworth, and Heckman data are large, and so, while the difference looks significant in Fig. 7, one cannot draw any useful conclusions about the relative quality of the two datasets from this example.

Bender and Möllenhoff (1987) have also undertaken a large program of CCD surface photometry in which they measured $V-I$ and $R-I$ color gradients for a number of Virgo ellipticals. They also find that ellipticals typically become bluer with radius, and have noted that structure occurs in the color profiles; for example, the change in slope in the color gradient in NGC 4472 (which we see in $B-R$). The small slopes that they find in their $V-I$ and $R-I$ profiles are similar to those found by us in $B-R$, as would be expected since the sensitivity to population/metallicity changes is comparable in these bands. Their results confirm the value of $U-R$ with its much enhanced sensitivity to metallicity and population changes.

Recently more color profiles have become available from Vigroux *et al.* (1988) in B and R, using CCD photometry. In a paper interpreting these color gradients Vader *et al.* (1988) tabulate the color gradients they find in $B-R_J$ per decade in radius. In Fig. 8 a comparison is made for the nine galaxies we have in common. Our gradients have been converted to the Johnson system by multiplying them by a factor

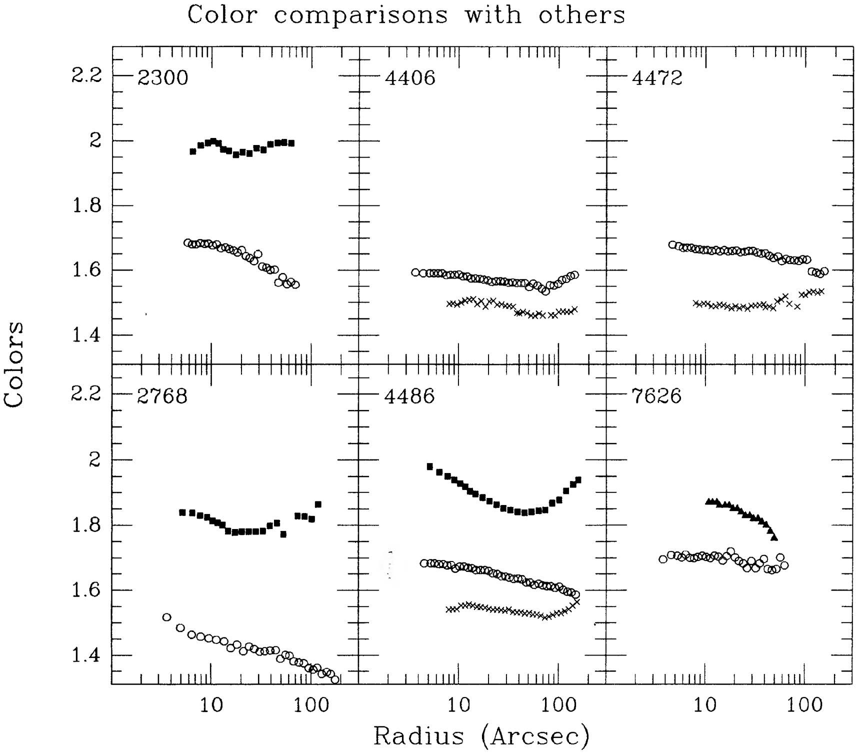

FIG. 7. Color gradient comparisons with other authors. Our data have been plotted with open circles. The Boroson *et al.* (1983) $B-R_J$ data are shown as filled squares, the Franx, Illingworth, and Heckman (1989b) $B-R_J$ data as filled triangles, and the Cohen (1986) $g-r$ data as crosses. We have added 1 to the $g-r$ data from Cohen. No correction has been made for the zero-point differences in the bands. The expected differences *others—us* are ≈ 0.25 mag for the Boroson, Thompson, and Shectman data and the Franx, Illingworth, and Heckman data, and ≈ -1.1 mag for the Cohen data.

1.14. The agreement is reasonably good; all points lie close to the line of equal gradients, except NGC 5638, for which the gradient from Vader *et al.* is much larger than the value we found. These authors do not fully take into account the effects of seeing. In addition, their estimate of the errors in the sky background determination are apparently too small. Together these effects, seeing and sky determination, could be responsible for the scatter in Fig. 8.

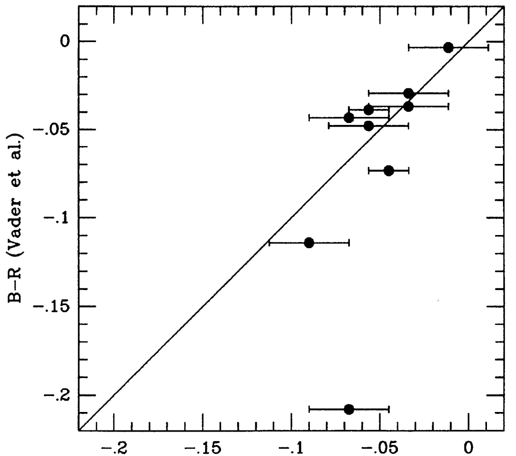

FIG. 8. A comparison of the logarithmic gradients in color in mag per decade in radius between Vader *et al.* (1988) and us. Our values have been transformed to the Johnson system.

c) Deviations from Elliptical Isophotes

In general the isophotes of these galaxies are very close to ellipses. However, as noted by several authors (e.g., Carter 1978; Lauer 1985; Bender *et al.* 1988) deviations are common at the 1% level. With rare exceptions, primarily of galaxies that contain substantial quantities of dust, the maximum deviations from ellipses are 1.5%–2%, with 0.5% being a more typical value. Although small, the 3θ and 4θ terms given are real; they agree between B and R, as well as with the results of other authors (e.g., Bender *et al.* 1988).

While we have represented these deviations by the amplitudes of the cos and sin 3θ and 4θ terms, representing them as the phases and amplitudes of the 3θ and 4θ terms has value for understanding the structure(s) that contribute to the deviations from ellipses (Franx, Illingworth, and Heckman 1989b). The amplitudes and phases, determined from the peak values as for the Table V results, are tabulated in Table VI. The radius of the fourth-order peak is also given.

Differences in B and R are also a useful diagnostic of the presence of dust. Nonzero 3θ terms are often found at the radius where a galaxy is known to have dust absorption; for example, in NGC 315 (Butcher, Van Bruegal, and Miley 1980; Kormendy and Stauffer 1987), NGC 1052 (Davies and Illingworth 1986), NGC 2768 (Strom *et al.* 1978), NGC 3665 (Kotanyi 1979), NGC 3801 (Heckman *et al.* 1983), NGC 4278 (Gunn 1979), and NGC 4374 (Hansen Nørgaard-Nielsen, and Jørgensen 1984).

Again, a diagnostic for the presence of dust is that the 3θ and 4θ terms differ in B and R. The integrated colors of these galaxies are no redder than dust-free ellipticals so it appears that the amplitude of the 3θ terms and the differences seen between B and R are much more sensitive indicators of the presence of small quantities of dust than integrated colors.

TABLE VI. Effective amplitudes and phases of the higher-order terms.

Galaxy (1)	A3 (2)	$\phi3_{maj}$ (deg) (3)	$\phi3_N$ (deg) (4)	A4 (5)	r_{A4} ″ (6)	$\phi4_{maj}$ (deg) (7)	$\phi4_N$ (deg) (8)
NGC 315	0.003	15	55	0.004	25	50	0
NGC 720	0.003	115	10	0.004	23	55	15
NGC 741	0.007	60	-	0.007	–	80	–
NGC 1052	0.003	0	55	0.003	20	48	70
NGC 1129	0.015	52	5	0.008	–	65	68
NGC 1600	0.002	60	-	0.014	11	45	55
Abell 496	0.009	70	60	0.007	13	10	–
NGC 2300	0.006	0	90	0.007	38	85	80
NGC 2768	0.003	110	20	0.007	70	10	15
NGC 2778	0.002	90	0	0.002	22	40	0
NGC 2832	0.008	80	65	0.005	16	30	7
NGC 3377	0.002	40	70	0.019	6	0	40
NGC 3379	0.004	50	0	0.006	21	16	85
NGC 3605	0.002	20	40	0.012	16	47	67
NGC 3665	0.003	110	20	0.002	40	60	80
NGC 3801	0.010	60	5	0.016	5	40	–
NGC 4261	0.003	100	75	0.021	7	43	22
NGC 4278	0.004	100	115	0.004	40	80	85
NGC 4374	0.002	0	5	0.003	14	48	85
NGC 4387	0.003	0	20	0.012	8	53	10
NGC 4406	0.005	0	0	0.011	17	50	10
NGC 4472	0.003	80	60	0.006	28	35	15
NGC 4478	0.004	105	10	0.020	22	37	0
NGC 4486	0.001	60	-	0.001	–	40	–
NGC 4551	0.003	50	115	0.010	10	40	15
NGC 4636	0.003	50	15	0.004	–	50	25
NGC 4649	0.006	20	0	0.008	25	55	70
NGC 4697	0.005	30	95	0.026	22	00	67
NGC 4874	0.008	5	40	0.012	30	60	5
NGC 4889	0.004	55	10	0.003	16	50	5
NGC 5638	0.001	0	-	0.001	–	80	45
NGC 5813	0.004	20	90	0.003	30	65	30
NGC 5831	0.003	0	5	0.009	16	0	25
NGC 5845	0.005	110	12	0.010	17	80	45
IC 1101	0.004	40	-	0.003	10	60	80
NGC 6051	0.003	90	75	0.002	20	40	30
NGC 6086	0.006	25	-	0.006	13	85	87
NGC 6269	0.005	60	15	0.005	25	0	80
NGC 7626	0.004	105	100	0.005	19	20	30

Notes to TABLE VI

In columns (2) to (4) we list the effective amplitudes and phases of the third order Fourier terms (A3 and $\phi3$). In column (3) this phase is given with respect to the major axis, and in column (4) with respect to a fixed position angle (i.e., North). Columns (5), (7), and (8) list the same data for the 4th-order terms. We also tabulate (in column 6) the radius at which A4 reaches its maximum or minimum. The angles in columns (3) and (4) are modulo 120°, while those in columns (7) and (8) are modulo 90°.

Therefore, many of the other galaxies with significant nonzero 3θ terms and differences in the 3θ and 4θ terms may also be dusty. A way of confirming this could be through color maps (see, e.g., the maps of NGC 1052 in Davies and Illingworth 1986). Possible candidates for dust from our sample that have either significant 3θ terms or notable differences in the amplitudes in B and R would be NGC 2300, NGC 2832, NGC 3377, and NGC 5813.

For the remaining galaxies the nonzero third- and fourth-order terms presumably represent nonelliptical distortions in the stellar densities. Even for those with modest amounts of dust, some of the structure may well be intrinsic to the stellar component. One other class of galaxies needs to be distinguished in the discussion that follows. These are the large, often cD galaxies, Abell 496, IC 1101, NGC 741, NGC 1129, NGC 4874, NGC 4889, NGC 6051, NGC 6086, and NGC 6269, which are strongly contaminated by close companion galaxies, and are often of low surface brightness. For these galaxies the data are noisy and have had the many companions removed, rendering the data generally unsuitable for deriving deviations from ellipses.

There are only three galaxies in our sample which are consistent with having truly elliptical isophotes. They are NGC 4486, NGC 4636, and NGC 5638. Omitting the regions with dust it is possible to add NGC 5813 and NGC 3665 to this group. The remaining galaxies, with the exception of the large (cD?) galaxies noted above, can be usefully "classified" into three groups as follows:

(1) **"Box-shaped" galaxies.** These galaxies show a significant negative cos 4θ term, and usually a small sin 4θ term. This group contains NGC 720, 1600, 3605, 4261, 4374, 4387, 4406, 4472, 4478, 4551, and NGC 4649. Its members have small third-order amplitudes, except for NGC 4374 which contains dust and the outer parts of NGC 4649, where the influence of its companion, NGC 4647, is noticed. It is interesting to note that nearly half of these galaxies are low-luminosity elliptical companions (NGC 3605, 4387, 4478, and 4551) to giant ellipticals—out of a sample this is strongly biased towards luminous objects.

(2) **"Disk-like" galaxies.** The galaxies in this group have positive cos 4θ terms, that have been interpreted as being due to an embedded faint disk component. This disk is not comparable with those seen in S0 galaxies, since the contribution of this disk anywhere to the surface brightness never amounts to more than a few percent. The fourth-order amplitudes are large, with phases of 0° (modulo 90°). Members of this group are NGC 2768, 3377, 4697, 5831, and NGC 5845. NGC 3377 and NGC 4697 are excellent examples of ellipticals with weak disks. It is noteworthy that in the outer regions of all five galaxies, where the relative contribution of the disk has decreased considerably, the appearance of the isophotes changes: NGC 3377 and NGC 2768 become boxy, while the *phase* of the other three changes to $\approx 65°$, intermediate between "box-like" and "disk-like."

(3) **Exceptions.** Along with the dusty galaxies, this group consists of NGC 2778, 2832, 3379, and 7626. The amplitudes in this group are small, but still significantly nonzero. The structures are complex and not as easily interpreted as the two "classes" above. The third- and fourth-order deviations in NGC 2832 are probably caused by its close companion, NGC 2831. NGC 3379 is noteworthy. The third- and fourth-order amplitudes at 50° and 15°, respectively, indicate a complex shape, with a "diamond-like" character.

While generally small, there are good indications that these terms do convey useful information about the dynamical properties and dynamical history of ellipticals (e.g., Bender *et al.* 1989). This is discussed further in Sec. VI.

For those galaxies where the high-order deviations could be determined to large radii (i.e., excluding those galaxies whose outer parts were contaminated by companions/superpositions typical of the large galaxies in clusters), it is striking to note that most of the amplitudes in 3θ and 4θ peak at radii comparable to r_e or smaller.

Franx, Illingworth, and Heckman (1989b) also noted that plotting the phases against a fixed position angle (P.A.), as opposed to the major-axis position angle enabled one to readily identify features that do not follow the major axis, i.e., they do not twist. They show a striking example of a skew "disklike" structure in NGC 1700. We have plotted the phases against north for our galaxies. Comparing the constant PA phases with the phases plotted against the major-axis position angle, structures can occasionally be seen which do not follow the major axis. In our sample we have found two examples of this. They are NGC 1129 nd NGC 5831. The amplitudes of the third- and fourth-order terms and their phases with a fixed zero-point are plotted in Fig. 9.

Both galaxies have a large position angle twist; NGC 1129 by 90°! NGC 1129 is a large elliptical in a small cluster. Such galaxies have probably grown by digesting their neighbors—the structure in NGC 1129 could have resulted from a recent such acquisition. The position angle twist in NGC 1129 is so dramatic that we could even be seeing the result of a merger of two comparable ellipticals. On the other hand, if the galaxy is triaxial with different axial ratios, this twist might be intrinsic, and the result of viewing it along a favorable line of sight. At radii larger than 30″, the center of the isophotes has moved significantly to the SW, an effect seen in both *B* and *R*. By $r = 100''$, the center has moved 12″ away from its original position. This favors the merger hypothesis. In Fig. 14(a) we have added a grey-scale map of the central regions of this galaxy.

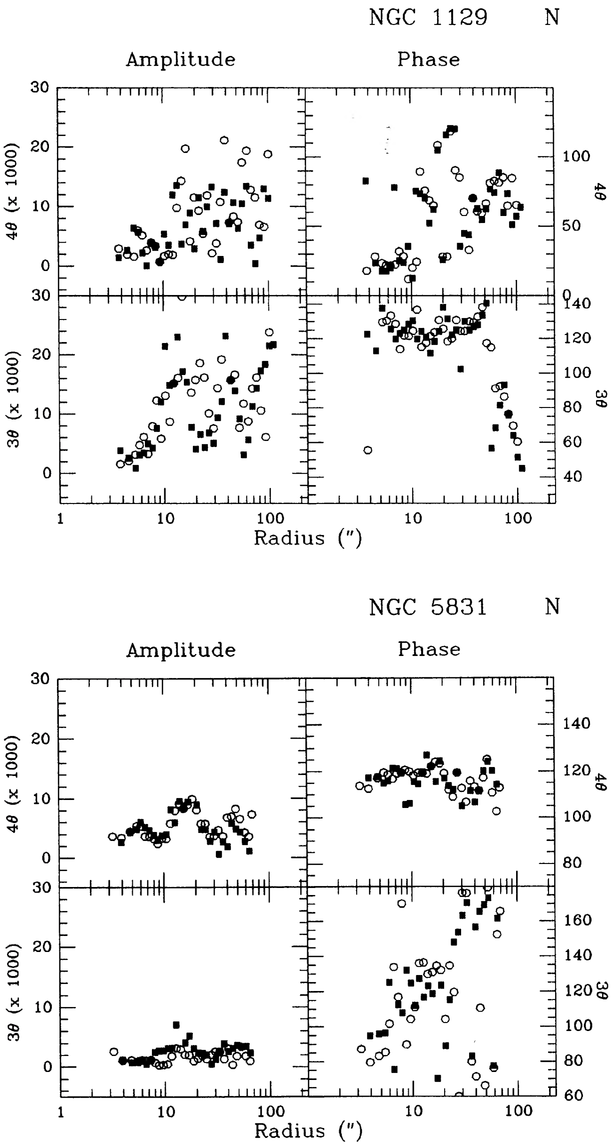

FIG. 9. The 3θ and 4θ Fourier terms presented as fractional amplitudes (in units of 0.001) and phases in degrees with respect to north for NGC 1129 and NGC 5831. In the former the position angle of the 3θ structure remains constant, while in the latter it is the 4θ structure that remains at constant position angle while the major axis twists. *B* data are shown as open circles, while *R* data are given as filled squares.

In NGC 5831 the most likely interpretation of the residuals is that there is a weak disk that does not twist in projection, unlike the major axis (cf. Fig. 15).

VI. DISCUSSION

The multicolor surface photometry of the sample of galaxies presented has been acquired and analyzed in a consistent way, and is large enough to allow us to explore the correlations of dynamical, photometric, and other properties of ellipticals. In addition, these data provide a valuable complement to the large body of kinematical data that is now available.

In Table VII we have compiled data from other sources on the kinematics and photometry of the galaxies in our sample. The values of $v_{\rm rot}$ and $v/\bar{\sigma}$ were taken from DEFIS, the central velocity dispersions and recession velocities were taken from Davies *et al.* (1987), and the photometric parameters such as the apparent magnitude, and the mean surface brightness within r_e were taken from Burstein *et al.* (1987), when available. The radio powers were mostly taken from Birkinshaw and Davies (1985). From these data absolute magnitudes and radio fluxes were derived assuming a uniform Hubble flow with $H_0 = 50$ km s^{-1} Mpc^{-1}, after correcting for the velocity with respect to the centrod of the local group. *IRAS* 100 μm fluxes wee taken from Knapp *et al.* (1989). The x-ray fluxes are from Canizares, Fabbiano, and Trinchieri (1987).

A number of correlations between the characteristic parameters of the stellar populations of galaxies, their structure, and kinematics will be explored using the data assembled in the previous section (Tables IV–VI) and the collected data of Table VII.

a) Box-Like and Disk-Like Isophotes

Bender (1988) has suggested that elliptical galaxies can be separated into two classes: those with "box-like" isophotes ($C4 < 0$), that are flattened by anisotropic velocity dispersions, and those with "disk-like" isophotes ($C4 > 0$) that are flattened by rotation. In Fig. 10(a) we plot $(v/\sigma)^*$ vs C4 for our sample, after removing the ellipticals with dust and the brightest cluster galaxies (including cD's) (see Sec. V). Our data show a similar distribution to that shown by Bender, with some detailed differences. It appears that for galaxies that are within a factor of 2 of being rotationally flattened (for which $(v/\sigma)^* \approx 1$), $(v/\sigma)^*$ is independent of C4. That is, for rotationally flattened ellipticals, there are roughly comparable numbers of elliptical galaxies with boxy as with disk-like isophotes. Bender's sample lacked the galaxies with boxy isophotes and $(v/\sigma)^* > 0.5$ such as NGC 2778, 3605, 4261, 4387, 4478, and 4551. It is interesting to note that four of these: NGC 3605, 4387, 4478, and 4551 are low-luminosity companions to luminous ellipticals, and that NGC 2778 has a close companion.

For galaxies that have $(v/\sigma)^* < 0.5$ there appears to be a strong preference for box-shaped isophotes. Essentially no galaxies are found that have low rotation and disk-like dis-

TABLE VII. Global parameters from the literature.

Galaxy (1)	r_e kpc (2)	$(\sigma)_m$ km s^{-1} (3)	$(v/\sigma)^*$ (4)	B_T mag (5)	M_{B_T} mag (6)	SB$_e$ mag arcsec^{-2} (7)	F_{100} mJy (8)	log P_{5GHz} W Hz^{-1} (9)	log ΔL_X erg s^{-1} (10)
NGC 315	35	352	0.17	12.50	-23.59	22.36	360± 90	23.09	41.91
NGC 720	8.7	247	0.47	11.15	-21.53	21.14	<56	<19.02	41.06
NGC 741	30	280	0.75	12.05	-23.10	21.64	1000± 96	22.39	– –
NGC 1052	5.0	206	0.70	11.53	-20.94	21.11	1400± 60	21.96	– –
NGC 1129	>26	335	– –	11.25	-23.68	– –	– –	– –	– –
NGC 1600	26	321	0.13	12.01	-23.14	22.17	170± 65	21.24	41.81
Abell 496	>47	354	0.11	13.42	-23.16	– –	– –	– –	– –
NGC 2300	12	260	– –	11.99	-21.54	21.51	<81	– –	41.10
NGC 2768	10.1	198	0.48	10.92	-21.16	21.56	1220± 56	19.93	– –
NGC 2778	3.4	166	1.11	12.50	-19.51	21.38	450± 85	<19.21	– –
NGC 2832	31	354	0.21	12.39	-22.86	– –	1330± 137	– –	– –
NGC 3377	3.0	131	0.80	11.10	-19.50	20.76	310± 57	<17.90	<39.60
NGC 3379	2.5	201	0.63	10.33	-20.20	20.16	<96	18.31	<39.80
NGC 3605	2.3	120	0.70	13.06	-18.34	21.42	– –	<18.18	– –
NGC 3665	13.4	205	1.20	11.75	-21.36	– –	6690± 163	20.96	– –
NGC 3801	13.8	168	0.85	13.00	-21.33	– –	2490± 78	– –	– –
NGC 4261	8.7	294	0.78	11.38	-21.78	21.25	130± 43	22.69	– –
NGC 4278	2.6	266	0.78	11.13	-19.87	20.60	1650± 53	21.18	– –
NGC 4374	5.9	287	0.23	10.23	-21.53	20.81	1030± 109	22.02	40.79
NGC 4387	2.1	84	0.72	12.95	-18.79	20.80	<158	<18.38	– –
NGC 4406	10.9	250	0.22	10.02	-21.79	21.65	290± 59	<18.39	41.58
NGC 4472	11.9	287	0.37	9.32	-22.34	21.40	<94	20.46	41.71
NGC 4478	1.7	149	1.05	12.15	-19.52	19.87	<66	<18.83	– –
NGC 4486	11.5	361	0.18	9.62	-22.14	21.60	360± 91	23.49	– –
NGC 4551	2.2	100	0.69	12.85	-18.94	20.95	<137	<18.36	– –
NGC 4636	12.2	191	0.32	10.50	-21.46	22.23	<152	20.06	41.64
NGC 4649	8.5	341	0.41	9.83	-21.89	21.10	970± 57	19.89	41.40
NGC 4697	9.9	165	0.82	10.11	-21.63	21.41	1100± 67	<18.40	40.27
NGC 4874	45	245	– –	12.90	-23.40	23.24	<95	– –	– –
NGC 4889	26	381	0.11	12.57	-23.23	21.96	<61	20.23	– –
NGC 5638	4.6	159	1.31	12.20	-20.47	21.28	400± 106	<18.74	– –
NGC 5813	9.1	238	0.07	11.57	-21.23	21.82	<88	19.35	– –
NGC 5831	4.5	166	0.58	12.46	-20.33	21.42	– –	<18.83	– –
NGC 5845	0.7	251	1.20	13.10	-19.27	18.38	200± 87	<18.83	– –
IC 1101	>110	375	0.08	13.93	-24.40	– –	– –	– –	– –
NGC 6051	25	243	– –	13.49	-22.95	– –	490± 296	– –	– –
NGC 6086	24	304	– –	13.50	-22.95	– –	<172	– –	– –
NGC 6269	50	228	– –	13.02	-23.63	– –	– –	– –	– –
NGC 7626	15	234	0.21	12.17	-22.35	21.87	<113	21.79	41.30

Notes to TABLE VII

In column (2) we present the major axis effective radii in kpc, using effective radii from Table 2.3 and group velocities from Davies *et al.* (1987), corrected for the motion with respect for the centroid of the local group. The mean velocity dispersion in column (3) in km s^{-1} and the $(v/\sigma)^*$ in column (4) are taken primarily from DEFIS and Malumuth and Kirshner (1985). The total blue luminosity in column (6) (in mag) is derived from the apparent blue luminosities given by Burstein *et al.* (1987) (in column 5), using $H_0 = 50$ km s^{-1} Mpc^{-1}. The mean blue surface brightness inside an effective radius was derived using the luminosities and effective radii here, and tabulated in column (7) in mag arcsec^{-2}. The *IRAS* 100 μm fluxes in column (8) were taken from Knapp *et al.* (1988) and are given in mJy. The radio powers (in W/Hz) were mostly taken from Birkinshaw and Davies (1985). The x-ray fluxes in ergs/s are from Canizares *et al.* (1987).

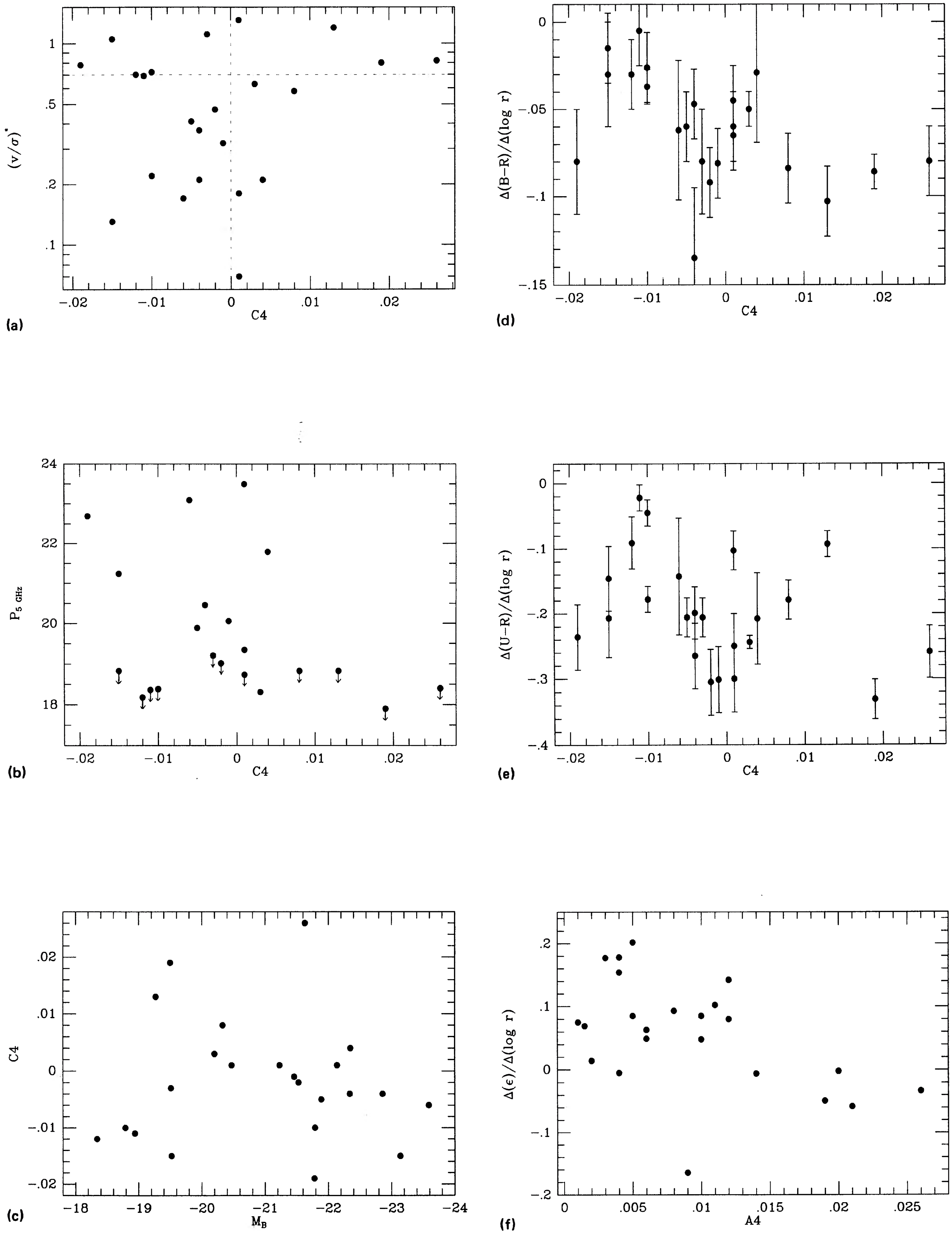

FIG. 10. Global parameters against C4 and A4. The data plotted against C4 ranges from $(v/\sigma)^*$, a measure of the amount of rotational support, in (a), to the radio continuum power at 5 GHz in (b), the total blue luminosity in magnitudes in (c), the logarithmic color gradient in $B-R$ in (d), and finally to the logarithmic color gradient in $U-R$ in (e). The fourth-order Fourier amplitude A4 is plotted against ellipticity at 10″ in (f).

tortions. Could this be the result of an observational selection effect? As Bender and others have noted, the existence of isophote residuals from ellipses that have positive amplitude for the cos 4θ term, C4, is indicative of the presence of a weak disk. Such a disk will typically be rotating much faster than the body of the elliptical. Major-axis velocity profiles will then have contributions from both the disk and the elliptical. The measurements of velocities in multicomponent systems with Fourier or CCF (cross correlation) is known to be biased towards the narrow lined, and thus the more rapidly rotating component (see, e.g., Whitmore 1980; Franx and Illingworth 1988). Thus the major-axis velocity in such a composite system would be biased towards higher values, leading to an overestimate of $(v/\sigma)^*$ [cf. Fig. 3 of Bender (1988) and Fig. 10(a)]. An example of an elliptical where the velocity drops significantly away from the major axis is NGC 4697 (Binney, Davies, and Illingworth 1990).

This may be a factor in the distribution of values in the C4 vs $(v/\sigma)^*$ plane, but does not diminish the remarkable correlations of C4 with radio power and x-ray luminosity seen in these data by Bender *et al.* (1989). The relevant parameter for these other correlations may not be the rotational properties of the elliptical body, but the presence or absence of a disk.

The picture is also complicated because some galaxies have both disk-like and box-like distortions of their isophotes. An example is NGC 3377 which has positive C4 for $r < 40''$ and negative C4 for $r > 40''$. What is the appropriate C4 to use in Fig. 10(a) in galaxies such as NGC 3377? We used the inner value, but this is rather *ad hoc.* Part of the problem is using C4 alone to describe the fourth-order residuals, and thus ignoring the sin 4θ component—or, alternatively, ignoring the phase of the effects. As noted by Franx, Illingworth, and Heckman (1989b), certain structures do not follow the major axis, and so use of the phase-amplitude form for the 3θ and 4θ terms may subsequently prove to be more useful in understanding the source of these deviations from ellipses. We will explore this in a future paper.

We have also investigated other correlations. We find no correlation in this sample of elliptical galaxies between ellipticity and C4; there are as many flattened galaxies in our sample with box-shaped isophotes as with disk-like perturbations. Our sample is too small to show the *V*-shaped distribution noted by Bender *et al.* (1989). Initial inspection of Fig. 10(b) indicates no correlation between C4 and luminosity, although there is a deficit of luminous galaxies with disk-like isophotes. However, if one excludes the galaxies that are close companions of giant ellipticals, the trend for luminous galaxies to be boxy, and for less luminous ones to be disk-like becomes clearer. Since the companion galaxies have other distinct properties, namely minimal or zero color gradients and appear to be rotationally flattened, they may well form a physically separate group of objects.

We also show the correlation with radio power in Fig. 10(c), as did Bender *et al.* (1987), and Bender *et al.* (1989). The lack of powerful radio galaxies among those with positive C4 is striking. Within the subset of galaxies with negative C4, there is no relation at all with $(v/\sigma)^*$, with radio flux or with luminosity [see Figs. 10(a)–10(c)].

Other correlations have been made. There is a slight tendency for galaxies with larger negative C4 to have smaller color gradients, both in $B-R$ and in $U-R$ [Figs. 10(d) and 10(e)]. This effect disappears when one removes the low-luminosity companions to bright ellipticals. If boxy isophotes arise from mergers or accretion events, as has been suggested by Binney and Petrou (1985), one might expect boxy galaxies to show smaller gradients. However, it would be unexpected if the lowest-luminosity galaxies were the ones that most strongly showed the effects of merging or accretion.

One correlation which did arise was between the logarithmic gradient of the ellipticity and the fourth-order amplitude (Table VI). Ellipticals with large fourth-order amplitudes, with the exception of NGC 5831 appear to have small ellipticity gradients [Fig. 10(f)]. The implications of this correlation are not clear.

b) Color Gradients

The colors of the galaxies in this sample become bluer with radius in both $U-R$ and $B-R$, with an occasional profile remaining constant in color. The color gradients do not depend upon ellipticity, *IRAS* 100μm flux (after removing the dusty ellipticals), or the twist in position angle. After removing NGC 3801, a particularly dusty galaxy, we find that the mean logarithmic gradient in $U-R$, i.e., $\Delta(U-R)/\Delta(\log r)$ is -0.20 ± 0.02 mag per dex in radius, and is -0.09 ± 0.02 mag per dex in radius in $B-R$. Such values are consistent with those found by Sandage and Visvanathan (1978). Transformation of their results to our system yields values of -0.21 and -0.10, respectively.

The $B-R$ and $U-R$ gradients correlate with each other (Fig. 11), but with some scatter. While recent star formation and/or age differences could be responsible for some of the scatter, it is most likely that the scatter arises from observational errors introduced by the uncertainty in the sky levels. We have made an attempt to determine this error. Since the sky uncertainties affect the outermost points, in a nonlinear way, the error in the gradient is dependent on the outer cutoff radius. However, since the color profiles are usually linear, when plotted against the logarithm of radius, the gradient can be determined in a region where the sky errors are less important.

We have estimated our errors in the gradients in the following way: We made three color profiles, namely the original, and two in which the color in the outermost point was 0.1 mag bluer and redder, as a result of the expected uncertainty in the sky (10%). From these profiles we used all data points up to $0.5r_e$, and determined the gradients using a least-squares method. The final error was a combination of the differences between these gradients with respect to each other and with respect to the original gradient, calculated using all the points. Typically, they are ≈ 0.03 mag in $B-R$ and 0.05 mag in $U-R$. Most of the scatter in Fig. 11 could be caused by these uncertainties, but for a few galaxies, like NGC 5845 and NGC 3665, other factors appear to be playing a role.

Assuming that the color gradients are due to metallicity changes (decreasing metallicity), it is of interest to see if the ratio of the $U-R$ to the $B-R$ mean color gradients are consistent with such a hypothesis. Since, in the past, models and/or measurements have been made in colors other than those studied here, we have used a multistep process to derive the expected metallicity change for a given color change. We used two relations by Burstein *et al.* (1984) from Galactic and M31 clusters, to find the dependence of $U-V$ and $B-V$ on Mg_2. To convert Mg_2 to [Fe/H] we used the

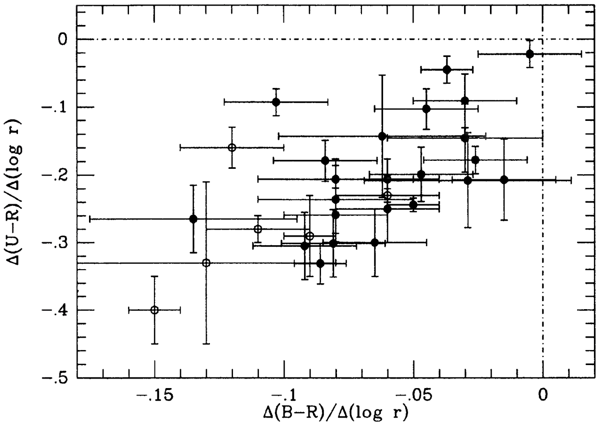

FIG. 11. Logarithmic color gradients in $U-R$ in mag dex^{-1} against color gradients in $B-R$. There is a correlation, but it is weaker than might be expected. This is mainly due to the large scatter in $\Delta(B-R)$ from observational uncertainty.

TABLE VIII. Gradient ratios.

age (1)	range in Z (2)	$\frac{\nabla(U-R)}{\nabla(B-R)}$ (3)
20 Gyr	0.04 - 0.01	1.79
	0.01 - 0.001	1.73
16 Gyr	0.04 - 0.01	1.71
	0.01 - 0.001	1.64

Notes to TABLE VIII

In column (3) we list the expected gradient ratio between $U-R$ and $B-R$ for integrated stellar populations for two different ages and two different metallicities (from Peletier *et al.* 1989).

relation from Mould (1978), [Fe/H] = 3.9 Mg_2 − 0.9, as suggested by Terlevich *et al.* (1981). $U-V$ and $B-V$ were converted to our observed $U-R$ and $B-R$ using synthetic colors for G-, K-, and M-type stars from the stellar library by Gunn and Stryker (1983). We found the following relations for converting $V-R$ to $B-V$ and $U-V$:

$$(B-R) = 1.465(B-V) + 0.098$$

and

$$(U-R) = 1.125(U-V) + 0.325.$$

Taking this together we determined that a change of 1 dex in [Fe/H] would give a change of 0.46 mag arcsec^{-2} in $B-R$ and 1.01 mag arcsec^{-2} in $U-R$ for the mean colors of these galaxies, so that the expected slope of the $\Delta(U-R)/\Delta(B-R)$ relation is 2.19. Our observed ratio of 2.2 ± 0.5 is quite consistent with this value and with the hypothesis that the gradients are due to metallicity changes. Our observed gradients correspond to a decrease in metallicity of 0.20 in. [Fe/H] per dex in radius for metallicities around solar. Given the uncertainties of the Mg_2 vs [Fe/H] calibration, this figure can be in error by a factor 2.

We have also derived the expected value of the $\Delta(U-R)/\Delta(B-R)$ ratio by using the artificial colors from Peletier, Valentijn, and Jameson (1990). They calculated integrated colors for composite stellar systems using the Yale (Green, Demarque, and King 1987) isohrones. For systems without a blue horizontal branch contribution, their values for $\Delta(U-R)/\Delta(B-R)$ are given in Table VIII.

These values while lower than what we derive, are certainly within the uncertainty of our mean ratio of 2.2 ± 0.5. Increasing the horizontal branch contribution in the outer parts results in larger numbers, as would be expected, and would give ratios closer to the observed value. Together these two approaches suggest that the observed ratios are consistent with the assumption that the color gradients are caused by a change in metallicity.

One should not infer too much from this conclusion, however, since the observational errors are large. The results from different authors are not as consistent as one would like. The differences are often comparable to the gradients, particularly in $B-R$. While difficult to measure, U-band data are very valuable since the gradients seen in $U-R$ are large enough that observational uncertainties do not dominate as they can in $B-V$ and $B-R$. We believe that the reality of color gradients is not now in question, and that the most likely explanation for them is a decrease in the metal abundance with radius. However, the detailed form of this variation is still rather poorly determined.

Vigroux *et al.* (1988) and Vader *et al.* (1988) have measured $B-R$ color gradients for 36 early-type galaxies. For their luminous galaxies, with measured kinematics, they found that galaxies with large $(v/\sigma)^*$, i.e., rotationally supported galaxies (see, e.g., DEFIS), have large color gradients. In the mean, as noted in Sec. V, their gradients agree with ours. In Figs. 12(a) and 12(b) we plot our $B-R$ and $U-R$ gradients against $(v/\sigma)^*$ for our whole sample with the exception of the largest galaxies (typically cD's and first-ranked cluster members). The correlation noted by Vader *et al.* does not appear with this sample. There is a hint in Fig. 12 that those with larger $B-R$ gradients may be more rotationally supported, but the opposite might be suggested by the $U-R$ data; neither "trend" is at all significant.

Color gradients (and absolute colors) can provide invaluable constraints on the formation processes for ellipticals. They have particular utility for what they can tell us about the role of gaseous interactions and star formation. The luminosity dependence of color gradients is a good discriminant among various models of galaxy formation. If galaxies were formed purely by dissipation, the most massive galaxies would have the largest color gradients (Carlberg 1984). Mergers on the other hand cause initial color gradients to decrease (e.g., White 1979). Thus, the luminosity dependence may provide clues as to the importance and frequency of mergers and/or accretions. The number of mergers which a galaxy has undergone would be expected to increase with luminosity, leading one to expect color gradients to diminish with increasing luminosity.

There is also no indication that galaxies change shape with photometric passband. There are no consistent, large-scale differences in the ellipticity profiles. The ellipticity profiles overlap in the different colors, except in the cases where dust is present. In such cases the dust usually manifests itself as rather irregular differences in the color ellipticity profiles, and in the 3θ and 4θ terms. This is also true of the noisier U-

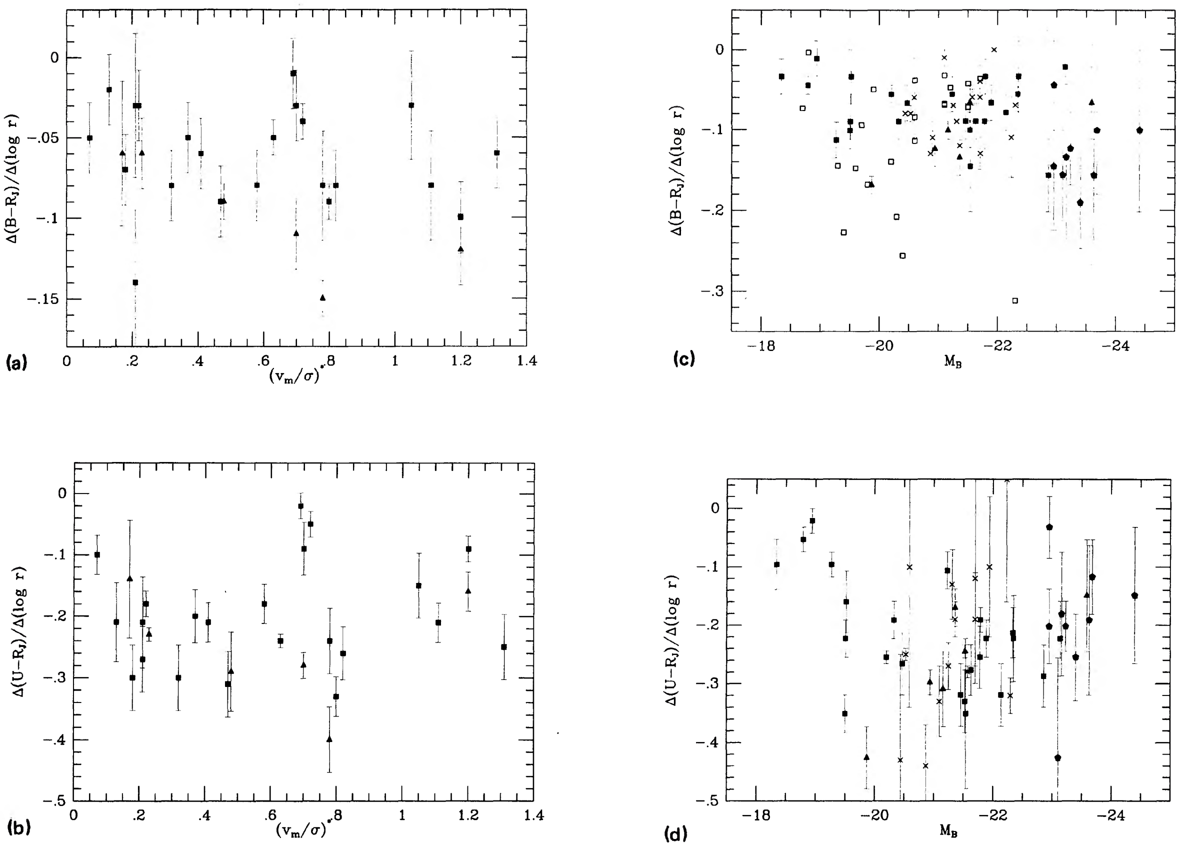

FIG. 12. Global parameters against color gradients. $(v/\sigma)^*$ is plotted against the color gradients in $B-R$ in (a), and against the $U-R$ gradient in (b). These figures show that there is no strong relation between the color gradient and the total amount of rotational support. The same color gradients have been plotted against total blue luminosity in (c) and (d). The data from this paper and Davis *et al.* (1985) are plotted with filled symbols. Dusty galaxies are indicated by triangles, while the brightest galaxies (including cD's) are shown as pentagons, and the remainder as squares. The data from Vader *et al.* (1988) are shown as open squares, and the Franx, Illingworth, and Heckman (1989b) data as crosses.

band ellipticity profiles. The differences in NGC 4697 and 5845 can be explained by dust absorption along the major axis. This result makes it unlikely that elliptical galaxies were formed in a simple one-stage dissipational collapse, because one should then see nontracking isophotes and isochromes (Carlberg 1984). However, the ubiquity of color gradients implies that dissipational collapse/accretion should not be ignored.

We have plotted our gradients versus absolute magnitude in Figs. 12(c) and 12(d), using the values tabulated in Tables IV and VI. We have included the cD and first-ranked galaxies, as well as the galaxies with dust. They are distinguished by different symbols. To these we have added the data from Vader *et al.* and Franx, Illingworth, and Heckman (1989b). The latter datasets have been transformed to the Cousins system, using the relations $(B-R)_C = 0.88(B-R)_J - 0.04$ and $(U-R)_C = 0.94(U-R)_J - 0.07$, from Paper I.

From Fig. 12 we conclude the following:

(a) The three datasets are consistent, although Vader *et al.* have some galaxies in their sample with very large $B-R$ gradients.

(b) There is large, intrinsic scatter in the amplitude of the color gradients at all luminosities, with the possible exception of the highest and the lowest.

(c) There is no significant relation between color gradient and luminosity, nor is there a relation between color gradient and $(v/\sigma)^*$ [cf. Vader *et al.* (1988) and Kormendy and Djorgovski (1989) for an alternative view].

(d) The lowest luminosity galaxies ($M_B > -19$) have small or zero gradients. They have boxy isophotes and are rotationally flattened, and are the companions of giant ellipticals. It appears that this group may be physically distinct from the other galaxies and that their evolution may have been strongly influenced by their massive neighbors.

(e) The brightest galaxies do not have significantly smaller color gradients, unlike that expected if larger galaxies were the debris of repeated mergers of smaller galaxies.

With the possible exception of the lowest-luminosity galaxies, the correlation of gradient with luminosity is distinguished by its lack of any clear trend. While observational uncertainty could mask any such relation for $B-R$, this is less likely to be the case for the $U-R$ data for which the gradients are significantly larger. Given that there is a trend of color with luminosity, and that color gradients are ubiquitous, it is noteworthy that color gradients themselves do not vary systematically with luminosity.

c) Other Relations

Position angle twisting appears to depend only upon the intrinsic orientation of the galaxy, and not on luminosity or any other parameters. In Fig. 13 we have plotted the amount of position angle twist per dex in radius against ellipticity at $r_e/2$ for all galaxies except the brightest cluster galaxies and the cD's. We see clearly that position angle twists are larger for round galaxies. This is what one would expect for triaxial galaxies. If position angle twists were mainly caused by tidal interactions flattened galaxies would also have rather large position angle twists.

As was seen in Djorgovski's (1985) thesis data, both ellipticity and the major-axis position angle vary a lot with radius. An extreme example is NGC 1129, for which we have measured a position angle twist of almost 90°. Such large twists, while rare, are possible for projected triaxial figures for special viewing orientations. In general galaxies become rounder at smaller radii, even accounting for the effect of seeing. However, the sharp drop towards the center that is seen, e.g., in NGC 4697 and NGC 3377, can be explained entirely by seeing, indicating that it is certainly possible for a galaxy to have very elongated isophotes close to the center.

VII. CONCLUSIONS

With the advent of wide dynamic range, linear detectors, surface photometry is beginning to play an important role in delineating the properties of ellipticals. This is particularly true of multicolor surface photometry from which color gradients and maps can be derived. These data have particular relevance for formation models which involve gaseous processes.

The highlights of this program are:

(a) Multicolor *UBR* CCD images have been obtained for 39 elliptical galaxies, ranging in luminosity from $M_B \approx -18$ to some of the brightest cD galaxies. The use of a small telescope proved valuable in obtaining a good compromise between scale and field, enabling us to derive results at several arcseconds while still being able to determine the sky satisfactorily. The U data have proven particularly valuable for determining color gradients. The large amplitudes for the $U-R$ gradients, compared to $B-R$ gradients, gives us greater confidence in the reality of color gradients in ellipticals. Color gradients, particularly in $B-V$ and $B-R$, are still not well determined, as indicated by the disagreement between different authors. The derivation of higher-order residuals from ellipses has proven valuable, as shown by other authors. We show that it is important to use terms other than the cos 4θ residuals used by others.

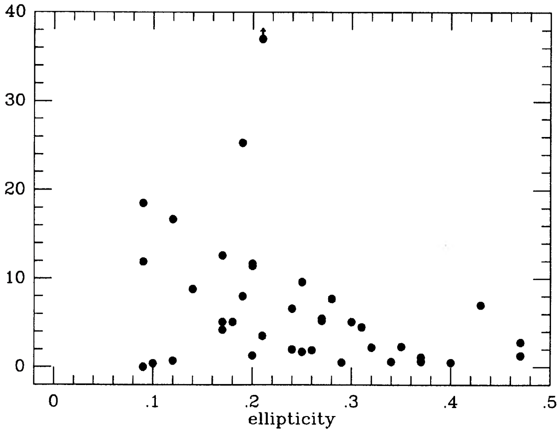

FIG. 13. Absolute position angle twist against ellipticity at $r_e/2$, showing that large position angle twists are not seen in flattened galaxies.

(b) While not an unbiased sample, it is large enough that some general statements would not be inappropriate.

(1) In general, elliptical galaxies show color gradients in both $U-R$ and $B-R$, with those in $U-R$ being 2.2× larger, in the mean than those in $B-R$. The gradients are always negative, except for a few cases where they are consistent with zero, i.e., the center is always redder than the outer parts. The mean logarithmic gradient in $U-R$ is $\Delta(U-R)/\Delta \log r$, is -0.20 ± 0.02 mag per dex in radius, while that in $B-R$ is -0.09 ± 0.02 mag per dex in radius.

(2) $U-R$ gradients correlate with those in $B-R$. The mean of the ratio of the gradients in $U-R$ and $B-R$ is consistent with a decreasing metallicity profile, with a change of metallicity of $\Delta[\mathrm{Fe/H}]$ of 0.20 per dex in radius.

(3) There is virtually no correlation between absolute magnitude and color gradient, with the possible exception of smaller gradients in the lowest luminosity ellipticals. The scatter at any luminosity is intrinsic, being greater than the observational uncertainty, particularly in $U-R$.

(4) Some ellipticals have ellipticity profiles that are consistent with being quite flattened at small radii, i.e., at radii of the order of 1–200 pc (less than a few arcseconds, typically). This effect is often masked by seeing which can effect ellipticity profiles out to large radii (5–10 seeing radii).

(5) Dust is common in ellipticals, and may explain some of the reddening in the centers of ellipticals, but not all since line strength gradients provide strong evidence for metallicity changes.

(6) Ellipticity, position angle and the higher-order terms show no color dependence, except when the complicating effect of dust is present. While the sensitivity to differences is low, there is no evidence for isochromes to be more flattened than isophotes.

(7) Elliptical galaxies have elliptical isophotes, with the high-order (third- and fourth-order Fourier components) residuals usually not exceeding 1% in amplitude. More typical values are 0.5%, with fourth-order component occurring more commonly. Occasional galaxies, particularly dusty ones, have larger residuals. The more common form for the residuals is a box-shaped distortion characterized by a negative cos 4θ residual, or alternatively by a fourth-order maximum phase shifted by 45° from the major axis. This appears to be particularly common among low-luminosity ellipticals.

(8) We confirm that galaxies with disk-like distortions, i.e., positive cos 4θ residuals, or alternatively fourth-order maxima aligned with the major axis show strong rotation and are not strong radio sources. We note that such relations could be biased by the preferential detection of the weak, but rapidly rotating disk component in those galaxies with disk-like isophotes, and also by the enhancement of both the rotation and the amplitude of the high-order terms in edge-on galaxies.

(9) We suggest that the low-luminosity ellipticals that are companions to giant elliptical galaxies may form a physically distinct group. They appear to have small or zero color gradients, boxy isophotes and rotation velocities sufficient to account for their flattening. This combination of properties distinguishes them from other ellipticals. Perhaps their evolution has been strongly influenced by the presence of their massive neighbor.

The authors want to thank Tjeerd van Albada, Jeanette Barnes, Marijn Franx, Robert Jedrzejewski, Edwin Valentijn, and Tim de Zeeuw for their valuable advice and help with this work. We thank S. Djorgovski and Robert Jedrzejewski for access to their unpublished data. R.F.P. acknowledges travel support from the Leids Kerkhoven Bosscha Fonds, and thanks KPNO for its hospitality and support during two visits. The authors are grateful to the director of KPNO for generous allocations of telescope time.

APPENDIX A: NOTES ON THE INDIVIDUAL GALAXIES

NGC 315. A bright star at 200″ NW of the galaxy caused a gradient in the background across the frame. The galaxy was offset from the center of the frame so that the star itself did not fall on the frame. A model of the stellar profile of the form $I(r) = I_0 (r/r_0)^{-1.5}$ was subtracted in *B* and *R*.

NGC 720. This galaxy is quite isolated. We have data from October 1982 only. This run generated less reliable data than those of January 1984 and April 1984. The shape parameters were kept constant for $r > 100''$ to allow accurate determination of the luminosity profile.

NGC 741. The data for this galaxy consists of KPNO data in *R* and *U*, and *B* and *R* frames from the 1.54 m ESO telescope at La Silla, Chile. The ESO data had considerably better seeing, so that there is a large seeing difference between *U* on one hand and *B* and *R* on the other hand. A star at 9″ N of the core was masked out, as was NGC 742, a companion galaxy 50″ to the north.

NGC 1052. We used the same data from October 1982 as was used in Paper I. The 3θ and 4θ terms show considerable structure inside 20″; this probably results from the dust present in this galaxy (see, e.g., the detailed study by Davies and Illingworth 1986).

NGC 1129 (AWM7). This is a very luminous galaxy in a small group. Four companion galaxies in a chain to the south from 25″ to 50′ were masked out causing the galaxy profile to be noisier in this radius range. The large position angle twist is discussed in Sec. V [see Figs. 9 and 14(a)].

NGC 1600. The brightest galaxy in a group. Our KPNO data are of poor quality; the central regions were reobserved at ESO in *B* and *R* in December 1986, with seeing of 1.2″. The internal consistency between both datasets is good.

Abell 496. A 5% E–W gradient was subtracted from this galaxy in *B* and *R* before analysis. The quality of the data for this galaxy is poor despite the long integration times; the sky is probably uncertain by 2%. The *U* data is of particularly poor quality as the only frames we have are from the 0.9 m. The *R* and *B* frames were taken in cloudy conditions. All the companion galaxies of the central galaxy have been masked out.

NGC 2300. Poor seeing has smoothed out the inner profile. This galaxy is near the north pole so the poor image quality could be partly due to the large zenith distance. The galaxy has a lot of structure in the third- and fourth-order terms, probably because of the presence of dust. A "bump" between 20″ and 60″ in both the position angle and C4 profiles is suggestive of a possible additional "disk component" in the galaxy.

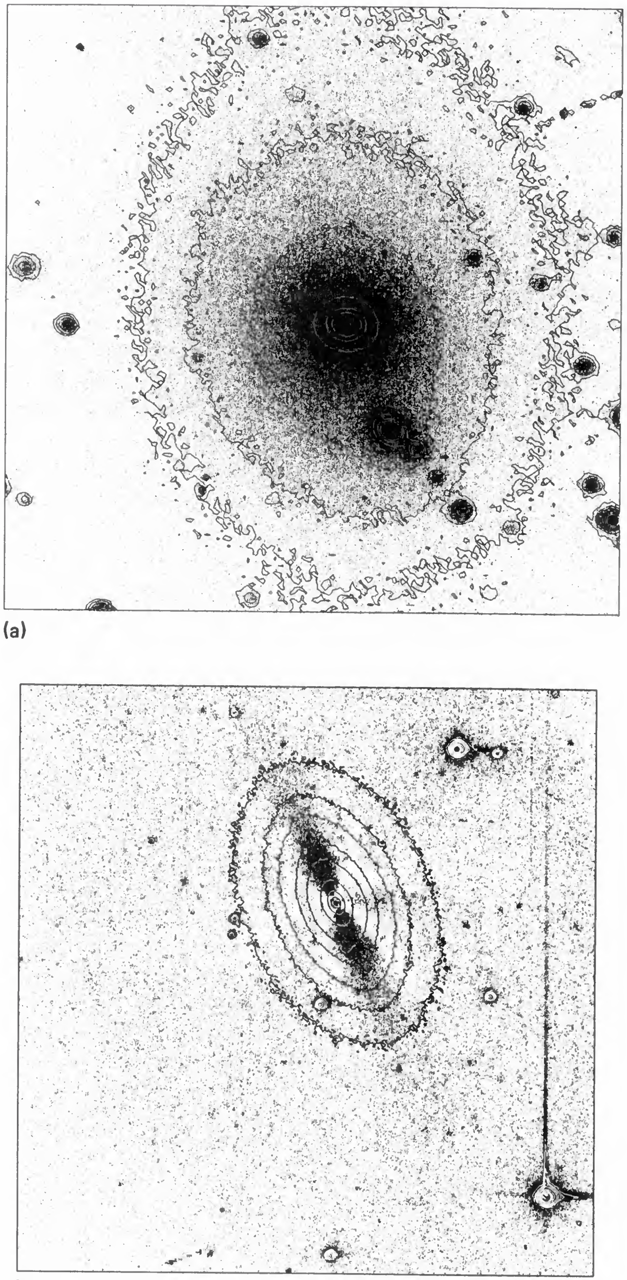

FIG. 14. A grey-scale image of the inner parts of NGC 1129, a galaxy with a position angle twist of almost 90°, is shown in (a). In (b) a difference image for NGC 4697 shows the "disk-like" structure on the major axis. A model of the galaxy, based on the surface photometry, with the assumption that NGC 4697 can be represented by ellipses, has been subtracted from the data frame, leaving the third- and fourth-order residual structure. The galaxy isophotes have been overlaid.

NGC 2768. This galaxy is very flattened in its outer parts, with the ellipticity rising steadily from the center. The power in the C4 term, in particular, suggests that there may be a disk-like component around 50″. The galaxy contains a considerable amount of dust (Ebneter and Balick 1985). The seeing for this galaxy was estimated from other frames taken on the same night.

NGC 2778. NGC 2779 has been masked out of the frames used. The signal-to-noise ratio has been greatly improved by the large number of galaxy frames used.

NGC 2832. This is the brightest galaxy in Abell 779. One close companion galaxy at 23″ N has been masked out, as has a disk galaxy at 80″ N. The S3 and S4 terms appear to be significant between 10″–20″.

NGC 3377. Determination of the sky was a problem since this large galaxy was only observed with the 2.1 m telescope. The sky was estimated from the corners of the frame, since the galaxy is quite elongated. The galaxy has a disk on the major axis, which is significant up to $\approx 30''$, and is boxy at radii larger than 40″. The luminosity profile changes slope at the position where the galaxy changes from "disk-like" to "boxy." To see whether the isophotes in the inner 40″ were boxy as well (in addition to the presence of a disk) we looked at the higher-order terms determined after having masked out the disk. They were around zero, which means that this galaxy has elliptical isophotes in the inner regions in addition to a disk and that the isophotes only become boxy after the disk has stopped.

NGC 3379. This galaxy was discussed extensively in paper I. We used the same data here, adding *U* data from April 1984. Although the amplitudes of the fourth-order terms are small, they are very significant. The deviations from elliptical isophotes are between disk-like and box-like, making the galaxy look like a diamond.

NGC 3605. This is a small galaxy close to NGC 3607. It was necessary to model NGC 3607 in *U*, *B*, and *R* and to subtract the models from the frames. The sky determination came from the 0.9 m frames. The isophotes are "boxy" at radii less than 20″, typical for the small companions of bright ellipticals.

NGC 3665. The strange behavior of the profiles around 10″ results from the sharp dust lane or ring,which is shown in Kotanyi (1979). Except for this feature, presumably responsible for its large *IRAS* flux, the galaxy looks normal.

NGC 3801. This galaxy is very dusty, with multiple dust lanes that have greatly affected the various profiles. It also has a very large color gradient in $U-R$ and in $B-R$, presumably because of the dust. Note that the amplitude scale for the third- and fourth-order terms has been changed to ± 0.10 in Fig. 15.

NGC 4261. This galaxy rotates about its major axis (Davies and Birkinshaw 1986). It also is the most "boxy" galaxy in this sample, with the largest amplitude for the C4 term, except for those galaxies with prominent dust lanes. Although our profiles agree very well with Bender and Möllenhoff (1987), we were not able to see the dust lane noted by them. The differences between their ellipticity profiles in the three bands suggest that their "dust lane" could have resulted from dividing two frames with nonzero ellipticity and different seeing. Kormendy and Stauffer (1987) noted an almost round patch of dust; our seeing is not good enough to confirm this.

NGC 4278. A relatively small galaxy containing dust (Ebneter and Balick 1985), and with a large amount of H I (Raimond *et al.* 1981). The companion to the NE was masked out.

NGC 4374. This large galaxy filled the CCD frame and since it is round in the outer parts the sky was difficult to determine and is uncertain. Note that there are considerable amounts of dust in the central regions (see, e.g., Hansen *et al.* 1984), which affected all profiles. From the fourth-order term, we conclude that NGC 4374 is slightly boxy between 10″ and 50″. The seeing in *U* was much worse than the seeing in *B* and *R*. The ellipticity profile is somewhat unusual in that it decreases monotonically outwards.

NGC 4387. This galaxy has very "boxy" isophotes, without any evidence for dust.

NGC 4406. Again the galaxy completely fills the CCD frame so the sky level is uncertain. NGC 4406 is also a minor-axis rotator, like NGC 4261 (Bender 1988; Illingworth and Franx 1988; Franx, Illingworth, and Heckman 1989a), but with a kinematically distinct core rotating around the minor axis. Apparently the core and the main body of the galaxy are decoupled. Interestingly, the isophotes are "boxy" outside the core, just like NGC 4261.

NGC 4472. This very large elliptical, the brightest in Virgo, was offset on the 0.9 m frame to provide a better estimate of the sky. The galaxy is slightly boxy. This galaxy is rotating slowly around its minor axis, except within the core inside 5″, where it does not rotate (Franx, Illingworth, and Heckman 1989a).

NGC 4478. A low-luminosity elliptical. A small NS gradient in the background on the *B* and *R* frames taken on the 0.9 m telescope was modeled and removed. The quality of the data is good since 2.1 m data was also available. This low-luminosity elliptical shows interesting structure from $r \approx 10''$–50″, with significant fourth-order terms peaking around 23″, outside which the position angle changes drastically. This galaxy, a companion to NGC 4486, has very small color gradients.

NGC 4486. This galaxy has been discussed in Paper I. The $U-R$ profile flattens in the center, as the bluer nuclear component begins to contribute. This is the roundest galaxy in the sample, and is truly elliptical, since it is one of the only three galaxies in this sample with higher-order terms that are consistent with zero. Since the ellipticity close to the center is very low, the accuracy of the position angle determination is reduced significantly, especially in *U*.

NGC 4551. A low-luminosity elliptical. Neither the 0.9 nor the 2.1 m data shows a color gradient in this galaxy. The isophotes are "boxy" between 5″–15″. A spiral companion, NGC 4550, was masked out.

NGC 4636. This galaxy is large and the radius at which the galaxy is only 5% of the night sky surface brightness was not reached. Although very similar to NGC 4649, its isophotes are very elliptical.

NGC 4649. A spiral galaxy, NGC 4647, was masked out in one of the corners. The galaxy is "boxy" from $\approx 10''$ outwards. Its kinematics are regular for a galaxy of this type; it appears not to have a decoupled core (Franx, Illingworth, and Heckman 1989a).

NGC 4697. The galaxy was offset to the north to allow determination of the sky background. NGC 4697 has a very large C4 term, which has a form similar to the ellipticity profile. This indicates that NGC 4697 has a strong major-axis disk. We verified this by subtracting a smooth model from the *R* frame. This is shown in Fig. 14(b). There are also indications of unusual structure in the outer regions (cf. NGC 3377).

NGC 4874. This elliptical is one of the two brightest in the Coma cluster. The data is of rather poor quality, due to its low surface brightness. A large number of companion galaxies have been removed, making the higher-order terms difficult to interpret.

NGC 4889. The other central galaxy in Coma. Again a large number of companion galaxies have been masked out.

1990AJ....100.1091P

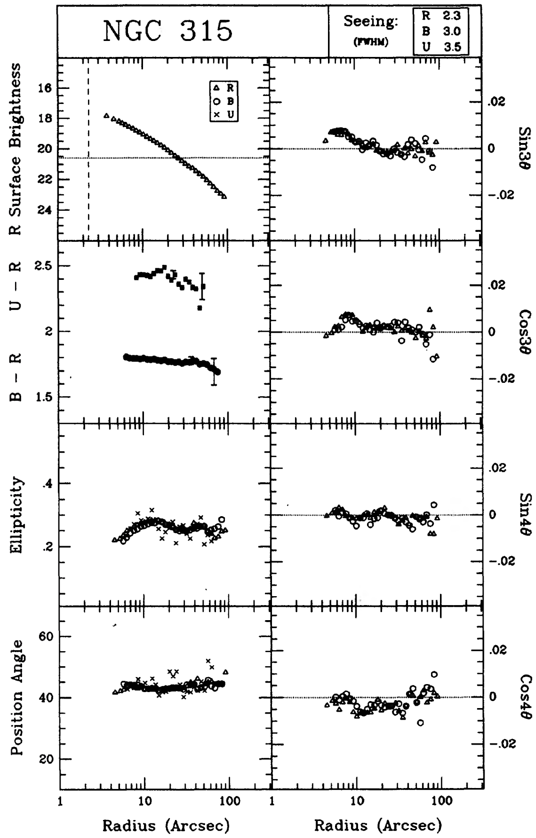

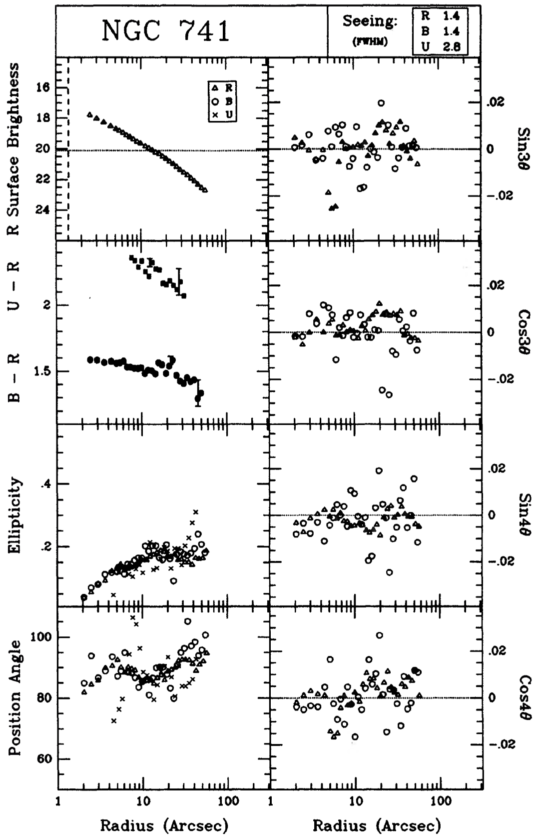

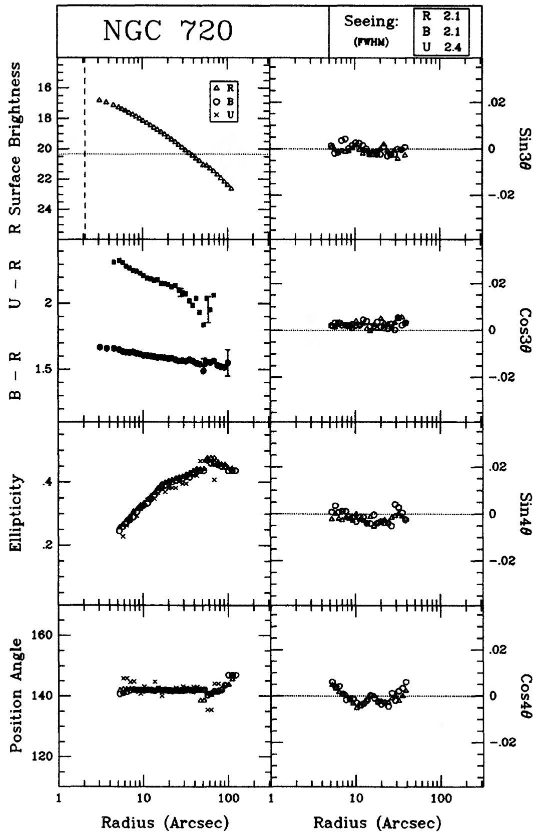

FIG. 15. The *R*-band surface brightness, ellipticity, and major-axis position angle profiles, as well as the $B-R$ and $U-R$ color gradients and the cos 3θ (C3), sin 3θ (S3), cos 4θ (C4), and sin 4θ (S4) profiles. The data are plotted as a function of major-axis radius in arcseconds. Data in the *R* band are indicated by open triangles, in *B* by open circles, and in *U* by crosses. Representative error bars for a 1% uncertainty in the sky are shown at two radii for the color profiles.

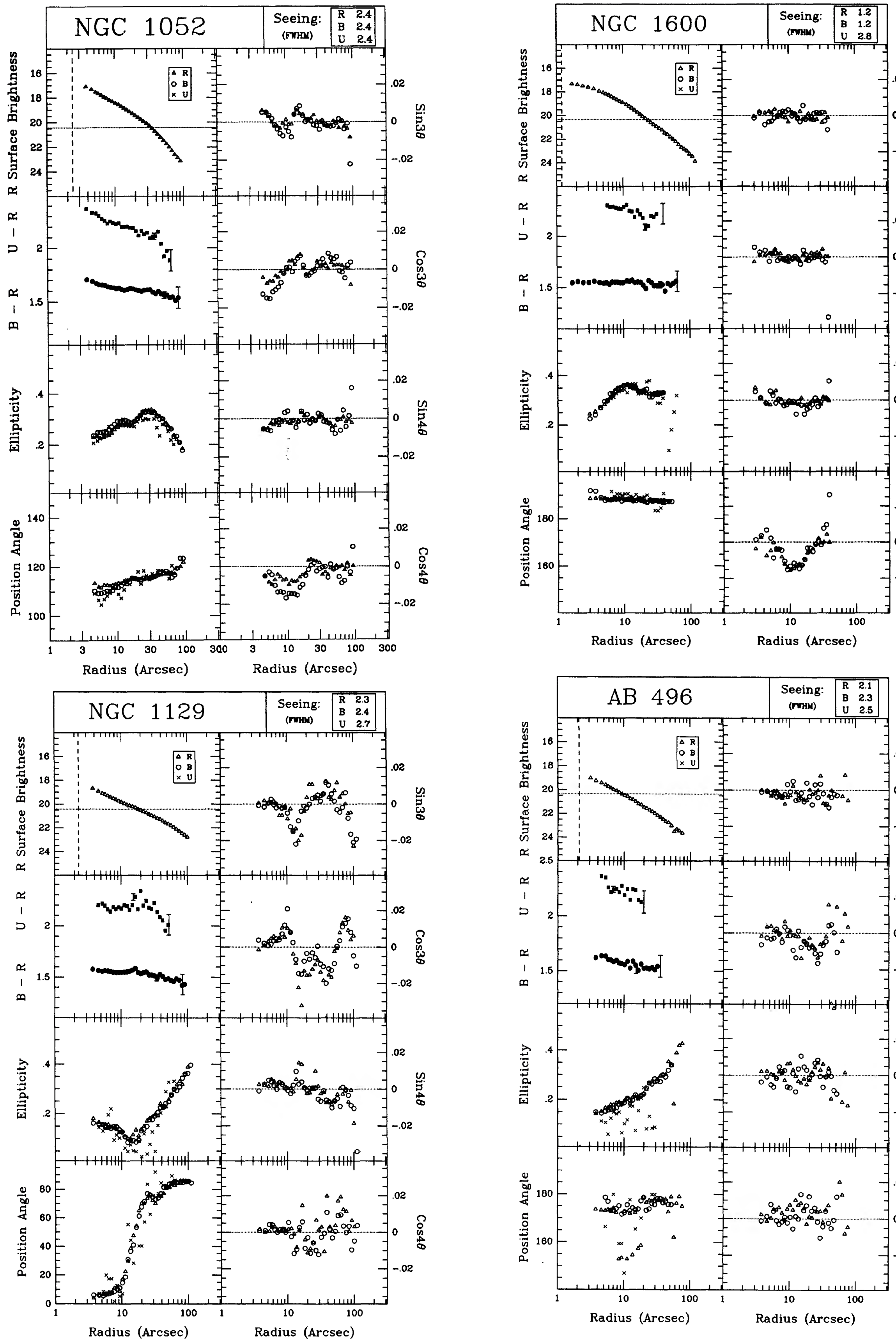

FIG. 15. (continued)

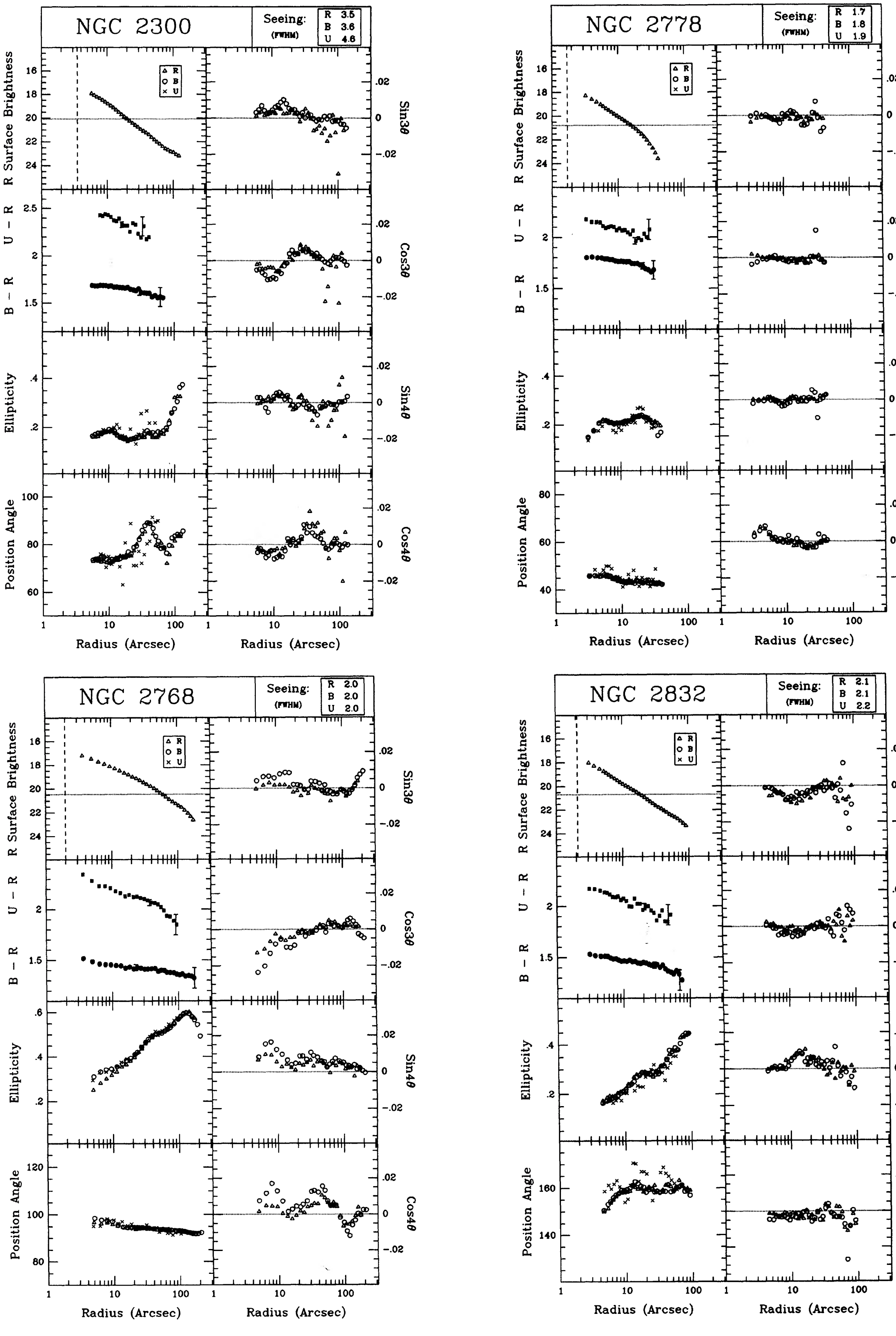

FIG. 15. (continued)

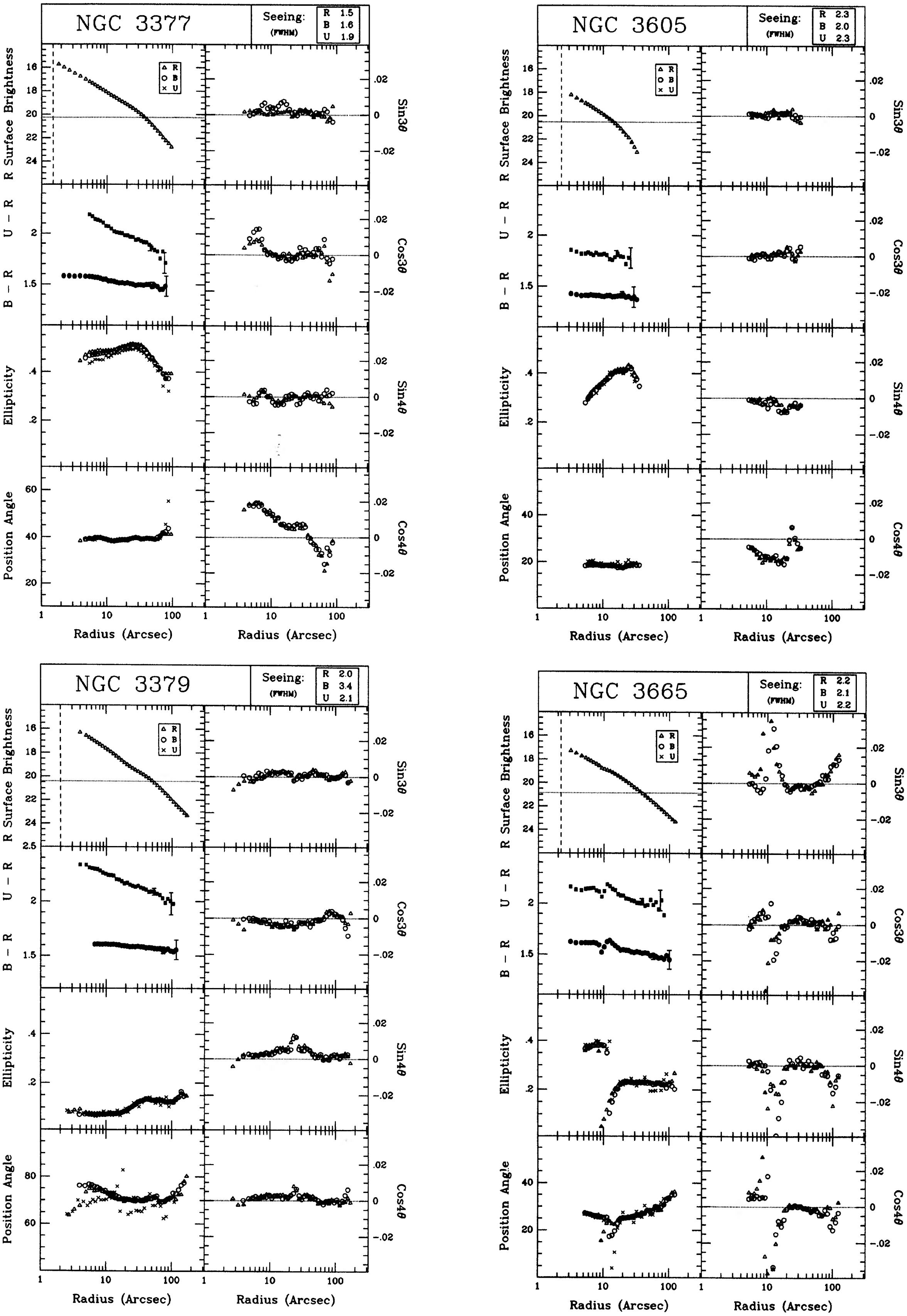

FIG. 15. (continued)

1990AJ....100.1091P

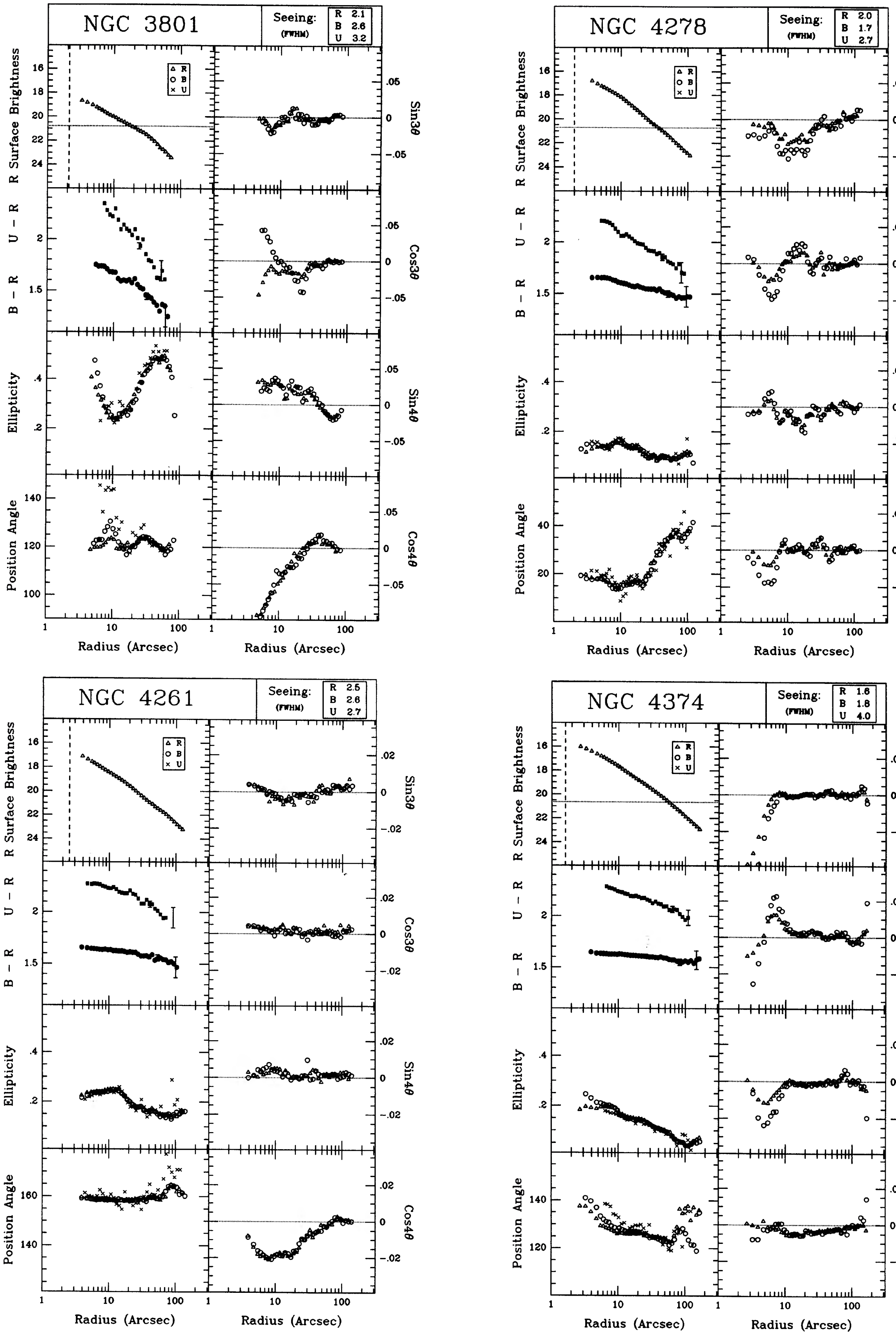

FIG. 15. (continued)

1990AJ....100.1091P

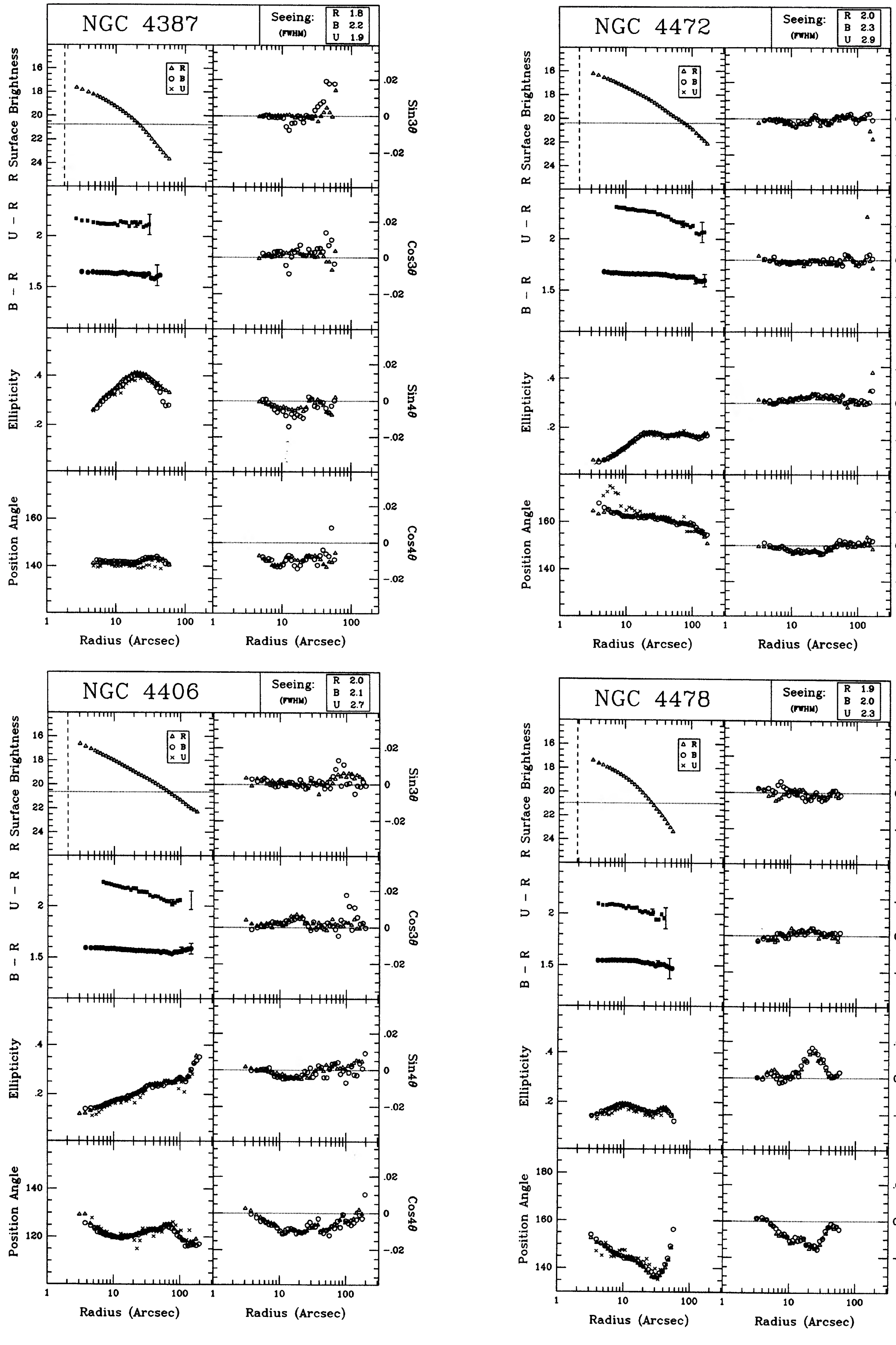

FIG. 15. (continued)

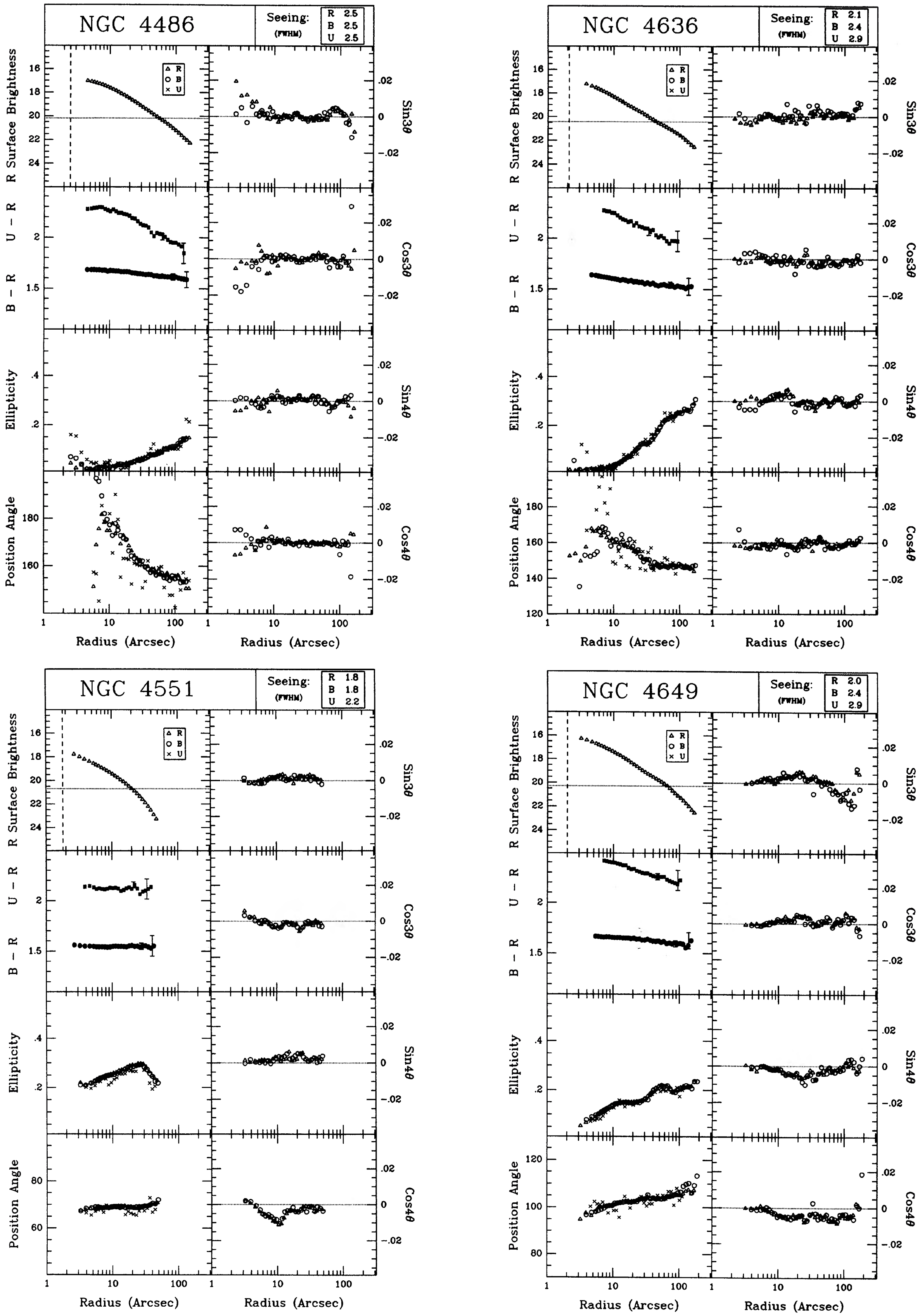

FIG. 15. (continued)

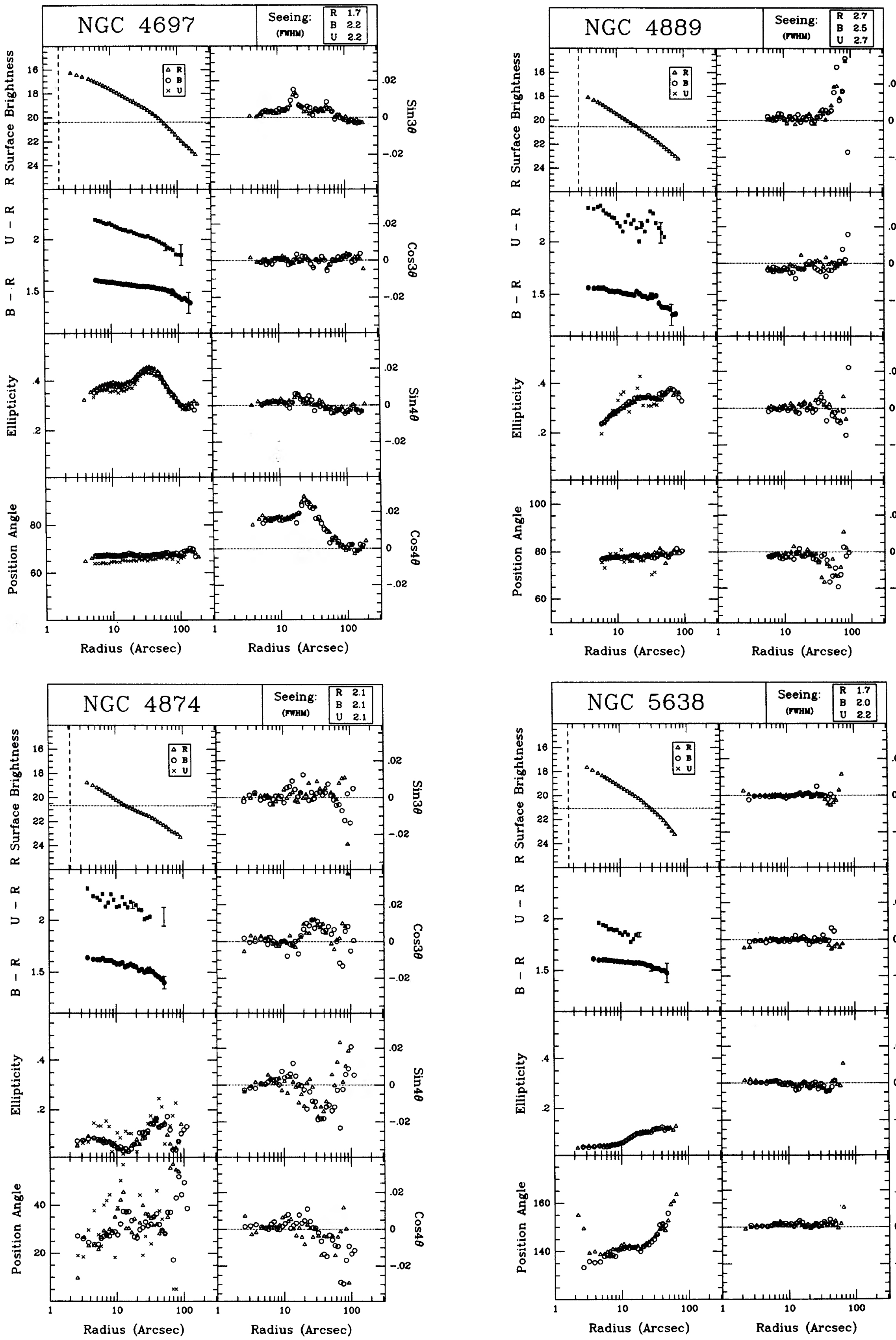

FIG. 15. (continued)

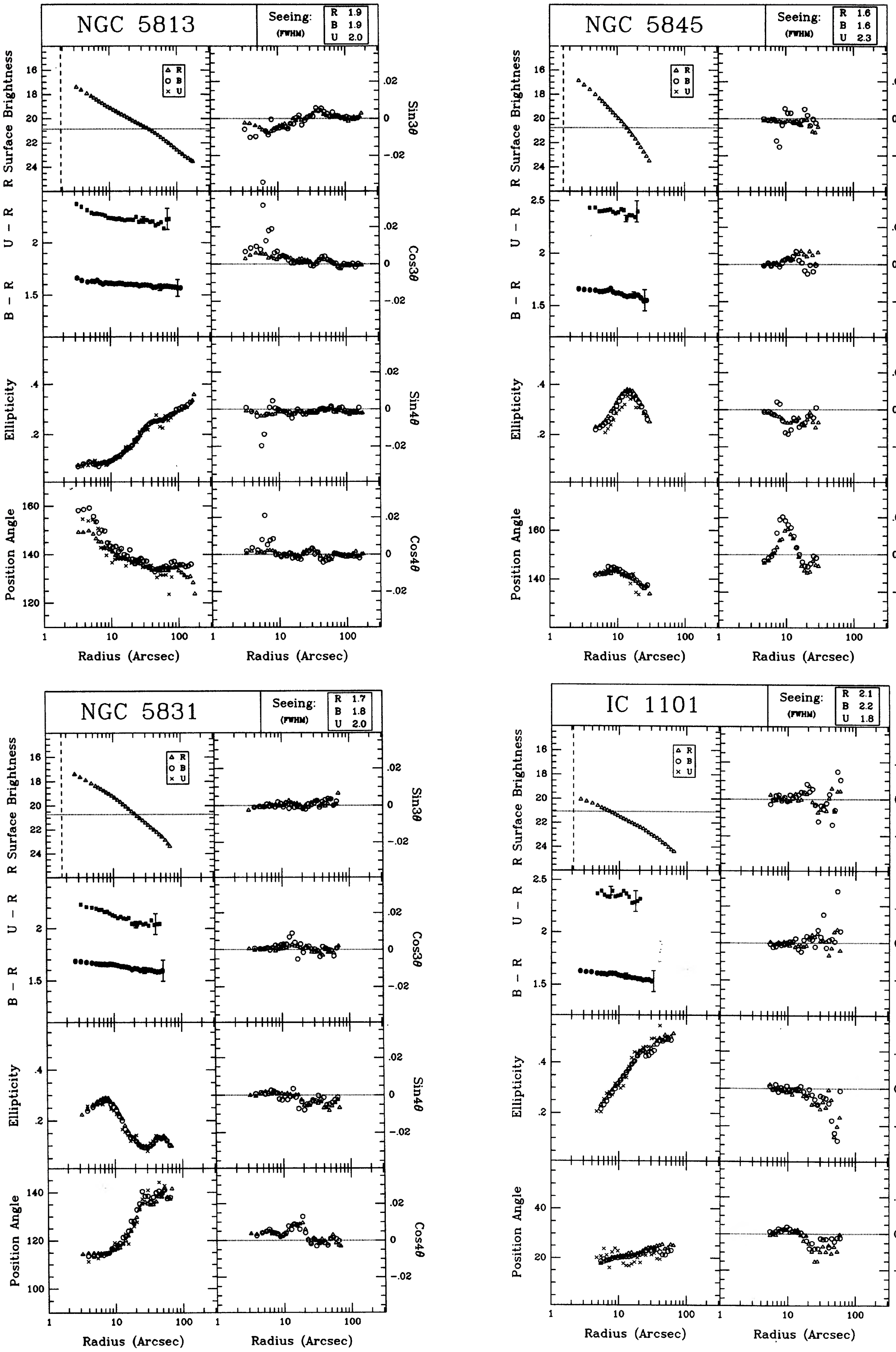

FIG. 15. (continued)

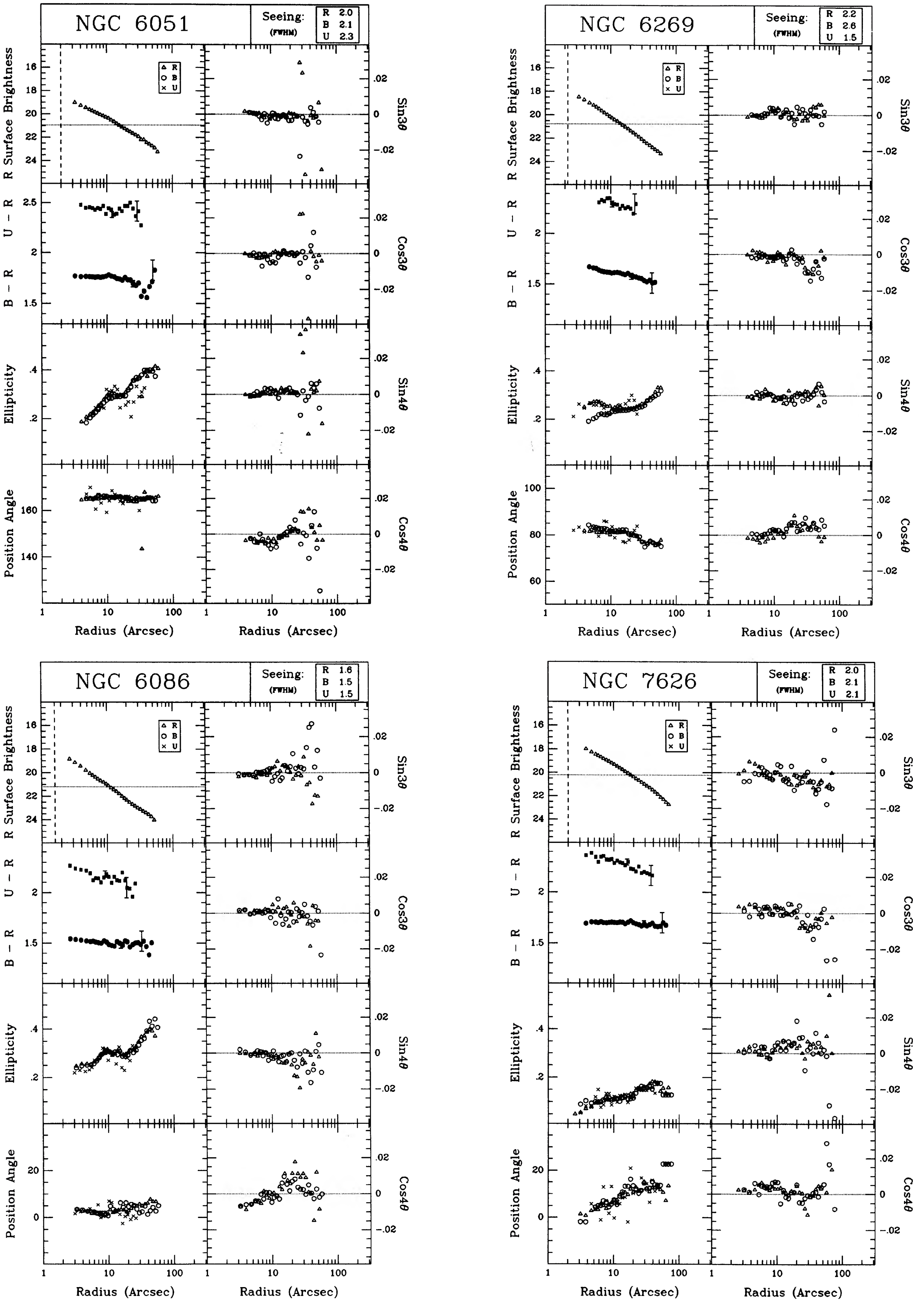

FIG. 15. (continued)

TABLE IX. Galaxy parameters.

NGC 315						NGC 720						NGC 741					
Radius (1)	μ_R (2)	ϵ (3)	ϕ (4)	$B-R$ (5)	$U-R$ (6)	Radius (1)	μ_R (2)	ϵ (3)	ϕ (4)	$B-R$ (5)	$U-R$ (6)	Radius (1)	μ_R (2)	ϵ (3)	ϕ (4)	$B-R$ (5)	$U-R$ (6)
3.8	17.84	0.207	41.0	- -	- -	3.1	16.82	- -	- -	1.67	- -	2.5	17.80	0.056	84.4	1.58	- -
4.6	18.05	0.221	41.7	- -	- -	3.8	16.96	- -	- -	1.66	- -	3.0	18.03	0.081	85.7	1.58	- -
5.3	18.21	0.225	42.1	- -	- -	4.6	17.12	- -	- -	1.66	2.32	3.6	18.27	0.091	89.8	1.57	- -
5.8	18.32	0.235	42.6	- -	- -	5.3	17.27	0.257	141.9	1.65	2.33	4.4	18.51	0.122	90.5	1.56	- -
6.4	18.44	0.249	43.5	1.80	- -	5.8	17.38	0.266	142.3	1.64	2.31	5.1	18.70	0.134	92.5	1.56	- -
7.0	18.56	0.254	44.0	1.80	- -	6.4	17.49	0.279	142.3	1.63	2.29	5.6	18.81	0.144	90.0	1.56	- -
7.7	18.69	0.261	43.2	1.79	2.45	7.0	17.62	0.292	142.4	1.63	2.27	6.2	18.96	0.125	88.3	1.57	- -
8.5	18.82	0.269	43.0	1.79	2.41	7.7	17.74	0.308	142.3	1.63	2.25	6.8	19.11	0.129	90.1	1.53	- -
9.3	18.95	0.274	43.3	1.79	2.43	8.5	17.88	0.315	142.1	1.62	2.25	7.5	19.24	0.134	89.6	1.53	2.36
10.2	19.08	0.276	42.6	1.79	2.43	9.3	18.01	0.326	141.8	1.62	2.23	8.2	19.37	0.140	89.1	1.52	2.34
11.3	19.22	0.279	42.8	1.79	2.43	10.2	18.17	0.333	142.0	1.60	2.21	9.0	19.52	0.144	86.7	1.52	2.29
12.4	19.35	0.283	42.7	1.78	2.42	11.3	18.31	0.344	141.7	1.61	2.19	9.9	19.64	0.157	85.5	1.53	2.34
13.6	19.49	0.283	42.5	1.79	2.44	12.4	18.46	0.355	141.8	1.60	2.19	11.3	19.83	0.158	85.8	1.51	2.22
15.0	19.63	0.284	42.0	1.78	2.46	13.6	18.61	0.365	141.8	1.60	2.18	12.4	19.94	0.169	86.3	1.51	2.22
16.5	19.78	0.276	42.7	1.78	2.46	15.0	18.76	0.380	142.3	1.59	2.18	13.6	20.09	0.175	84.7	1.48	2.32
18.2	19.94	0.272	42.7	1.78	2.49	16.5	18.90	0.394	141.9	1.59	2.15	15.0	20.22	0.182	86.6	1.56	2.28
20.0	20.10	0.267	42.8	1.77	2.42	18.2	19.06	0.398	142.0	1.59	2.15	16.5	20.33	0.188	87.6	1.55	2.27
22.0	20.27	0.264	42.7	1.77	2.39	20.0	19.23	0.402	142.0	1.58	2.14	18.2	20.50	0.183	85.8	1.48	2.17
24.2	20.46	0.251	43.0	1.76	2.43	22.0	19.39	0.407	141.8	1.58	2.13	20.0	20.66	0.170	88.7	1.54	2.16
26.6	20.63	0.253	42.8	1.77	2.36	24.2	19.56	0.412	141.6	1.57	2.14	22.0	20.82	0.167	89.2	1.58	2.19
29.2	20.81	0.247	43.1	1.76	2.33	26.6	19.74	0.414	141.7	1.56	2.10	24.2	20.97	0.175	89.9	1.47	2.15
32.2	20.98	0.251	43.6	1.77	2.40	29.2	19.92	0.418	142.0	1.56	2.08	26.6	21.17	0.157	92.2	1.42	2.12
35.4	21.14	0.256	45.0	1.77	2.38	32.2	20.09	0.423	141.8	1.56	2.07	29.2	21.36	0.159	92.6	1.41	2.18
38.9	21.29	0.274	44.6	1.78	2.33	35.4	20.27	0.430	141.9	1.57	2.02	32.2	21.54	0.150	92.6	1.45	2.07
42.8	21.47	0.261	46.1	1.77	2.32	38.9	20.45	0.436	141.8	1.56	1.99	35.4	21.71	0.150	92.5	1.42	- -
47.1	21.66	0.261	43.0	1.75	2.18	42.8	20.62	0.442	141.9	1.55	2.04	38.9	21.92	0.142	91.2	1.44	- -
51.8	21.84	0.266	44.4	1.75	2.34	47.1	20.81	0.442	138.6	1.54	1.93	42.8	22.10	0.164	88.9	1.29	- -
57.0	22.06	0.248	45.0	1.75	- -	51.8	21.07	0.442	138.6	1.49	1.84	47.1	22.33	0.162	91.0	1.34	- -
62.7	22.28	0.240	45.2	1.72	- -	57.0	21.11	0.476	140.8	1.55	2.04	51.8	22.55	0.163	92.1	1.40	- -
69.0	22.51	0.226	44.3	1.71	- -	62.7	21.30	0.476	140.3	1.55	1.95	57.0	22.71	0.188	94.7	- -	- -
75.8	22.77	0.232	44.2	1.69	- -	69.0	21.49	0.477	141.1	1.56	2.06						
83.4	22.96	0.248	44.2	- -	- -	75.8	21.72	0.463	141.8	1.53	- -						
91.8	23.16	0.251	48.2	- -	- -	83.4	21.94	0.456	142.4	1.52	- -						
						91.8	22.17	0.456	143.8	1.52	- -						
						101.0	22.40	0.443	143.8	1.55	- -						
						111.1	22.65	0.443	145.6	- -	- -						
						122.2	22.91	0.437	136.4	- -	- -						

TABLE IX. (continued)

NGC 1052					
Radius (1)	μ_R (2)	ϵ (3)	ϕ (4)	$B-R$ (5)	$U-R$ (6)
3.8	17.08	--	--	1.71	2.37
4.6	17.33	0.228	113.3	1.69	2.34
5.3	17.53	0.232	111.9	1.67	2.33
5.8	17.67	0.227	111.6	1.66	2.31
6.4	17.80	0.229	112.6	1.66	2.28
7.0	17.94	0.236	112.7	1.65	2.26
7.7	18.07	0.237	112.3	1.64	2.23
8.5	18.20	0.246	112.7	1.64	2.25
9.3	18.31	0.260	113.1	1.63	2.24
10.2	18.43	0.269	113.5	1.62	2.23
11.3	18.56	0.276	113.3	1.63	2.24
12.4	18.70	0.275	114.3	1.61	2.20
13.6	18.84	0.276	113.7	1.61	2.20
15.0	18.99	0.279	114.6	1.61	2.20
16.5	19.14	0.286	115.2	1.62	2.19
18.2	19.30	0.293	114.9	1.62	2.19
20.0	19.46	0.299	114.8	1.61	2.16
22.0	19.61	0.313	114.4	1.60	2.12
24.2	19.77	0.325	114.8	1.60	2.16
26.6	19.92	0.335	115.6	1.61	2.13
29.2	20.10	0.336	115.8	1.61	2.14
32.2	20.28	0.339	115.7	1.61	2.09
35.4	20.49	0.330	116.1	1.59	2.11
38.9	20.73	0.313	116.4	1.57	2.11
42.8	20.95	0.312	116.8	1.60	2.15
47.1	21.20	0.303	117.3	1.57	2.04
51.8	21.48	0.281	117.0	1.56	1.92
57.0	21.74	0.273	117.6	1.56	1.97
62.7	22.01	0.264	117.7	1.54	1.88
69.0	22.30	0.236	117.3	1.54	--
75.8	22.59	0.220	119.2	1.51	--
83.4	22.85	0.210	120.1	1.54	--
91.8	23.13	0.184	121.8	--	--

NGC 1129					
Radius (1)	μ_R (2)	ϵ (3)	ϕ (4)	$B-R$ (5)	$U-R$ (6)
3.8	18.67	0.181	4.1	1.58	--
4.6	18.90	0.167	6.0	1.57	2.20
5.3	19.07	0.155	6.7	1.56	2.22
5.8	19.18	0.158	6.4	1.57	2.20
6.4	19.29	0.157	8.3	1.56	2.16
7.0	19.40	0.148	7.3	1.56	2.14
7.7	19.51	0.143	11.1	1.55	2.18
8.5	19.62	0.137	12.0	1.54	2.16
9.3	19.73	0.125	9.0	1.55	2.18
10.2	19.83	0.128	17.3	1.55	2.17
11.3	19.94	0.106	22.7	1.55	2.20
12.4	20.05	0.099	30.0	1.55	2.19
13.6	20.13	0.099	38.8	1.56	2.15
15.0	20.21	0.115	47.5	1.57	2.20
16.5	20.29	0.135	54.4	1.59	2.28
18.2	20.42	0.111	64.9	1.54	2.16
20.0	20.51	0.136	70.3	1.53	2.34
22.0	20.63	0.150	70.2	1.54	2.20
24.2	20.72	0.172	73.8	1.55	2.24
26.6	20.85	0.182	76.6	1.52	2.18
29.2	20.96	0.188	72.2	1.52	2.16
32.2	21.07	0.197	70.1	1.51	2.22
35.4	21.19	0.193	75.5	1.49	2.14
38.9	21.25	0.241	75.2	1.53	2.09
42.8	21.40	0.227	77.2	1.51	2.05
47.1	21.55	0.229	81.1	1.48	1.96
51.8	21.68	0.257	81.4	1.48	2.01
57.0	21.82	0.274	83.6	1.47	--
62.7	21.95	0.299	82.6	1.46	--
69.0	22.11	0.316	84.5	1.48	--
75.8	22.26	0.330	86.1	1.47	--
83.4	22.45	0.319	86.0	1.42	--
91.8	22.61	0.360	86.1	1.43	--
101.0	22.76	0.388	85.4	--	--
111.1	22.93	0.409	85.8	--	--

NGC 1600					
Radius (1)	μ_R (2)	ϵ (3)	ϕ (4)	$B-R$ (5)	$U-R$ (6)
1.7	17.32	--	--	1.56	--
2.1	17.39	--	--	1.56	--
2.5	17.49	--	--	1.55	--
3.0	17.61	0.245	8.5	1.55	--
3.7	17.75	0.255	8.7	1.55	--
4.4	17.92	0.268	8.4	1.55	--
5.1	18.06	0.283	8.7	1.54	--
5.6	18.17	0.296	8.1	1.55	2.30
6.2	18.27	0.311	8.2	1.53	2.29
6.8	18.41	0.323	8.6	1.55	2.29
7.5	18.52	0.337	8.6	1.55	2.28
8.2	18.64	0.346	8.6	1.55	2.27
9.0	18.78	0.350	8.5	1.55	2.27
9.9	18.91	0.359	8.1	1.55	2.29
11.3	19.07	0.360	8.7	1.56	2.31
12.4	19.23	0.352	7.6	1.56	2.25
13.6	19.37	0.356	7.5	1.57	2.24
15.0	19.54	0.348	8.0	1.55	2.19
16.5	19.71	0.339	7.8	1.56	2.25
18.2	19.88	0.338	7.4	1.55	2.22
20.0	20.06	0.332	7.1	1.52	2.18
22.0	20.23	0.327	6.7	1.49	2.09
24.2	20.40	0.326	7.7	1.57	2.10
26.6	20.57	0.322	7.5	1.55	2.20
29.2	20.74	0.323	7.7	1.52	2.19
32.2	20.91	0.320	7.5	1.52	2.22
35.4	21.06	0.326	7.0	1.52	--
38.9	21.22	0.327	6.4	1.53	--
42.8	21.46	0.254	6.4	1.47	--
47.1	21.59	0.295	6.4	1.54	--
51.8	21.79	0.300	12.5	1.52	--
57.0	21.98	0.269	8.4	1.54	--
62.7	22.19	0.269	8.2	1.56	--
69.0	22.44	0.272	7.2	--	--
75.8	22.67	0.268	7.9	--	--
83.4	22.80	0.304	7.9	--	--
91.8	22.98	0.317	7.4	--	--
101.0	23.22	0.317	7.4	--	--
111.1	23.44	0.304	8.1	--	--
122.2	23.85	0.314	9.2	--	--

TABLE IX. (continued)

Abell 496 cD						NGC 2300						NGC 2768					
Radius (1)	μ_R (2)	ϵ (3)	ϕ (4)	$B-R$ (5)	$U-R$ (6)	Radius (1)	μ_R (2)	ϵ (3)	ϕ (4)	$B-R$ (5)	$U-R$ (6)	Radius (1)	μ_R (2)	ϵ (3)	ϕ (4)	$B-R$ (5)	$U-R$ (6)
3.1	19.17	--	--	--	--	5.8	17.94	0.161	73.0	1.68	--	3.6	17.21	--	--	1.52	2.34
3.8	19.38	0.142	173.6	1.62	--	6.4	18.08	0.161	73.3	1.68	--	5.0	17.49	0.251	96.7	1.48	2.28
4.6	19.58	0.153	173.2	1.64	--	7.0	18.23	0.163	73.0	1.68	--	6.4	17.73	0.283	96.1	1.46	2.23
5.3	19.74	0.166	173.1	1.64	2.35	7.7	18.37	0.170	72.8	1.68	2.43	7.9	17.92	0.302	96.6	1.46	2.23
5.8	19.87	0.166	173.5	1.61	2.26	8.5	18.52	0.177	73.0	1.68	2.42	9.5	18.12	0.316	95.8	1.45	2.21
6.4	19.99	0.179	173.2	1.60	2.22	9.3	18.66	0.181	72.5	1.68	2.44	11.4	18.29	0.332	95.2	1.45	2.18
7.0	20.12	0.178	174.2	1.59	2.24	10.2	18.82	0.181	72.2	1.68	2.43	13.5	18.47	0.354	94.8	1.44	2.16
7.7	20.23	0.186	172.3	1.60	2.25	11.3	18.98	0.181	72.7	1.68	2.41	15.8	18.66	0.364	94.3	1.42	2.13
8.5	20.37	0.190	152.9	1.58	2.21	12.4	19.15	0.175	73.9	1.67	2.38	18.3	18.82	0.380	94.5	1.43	2.14
9.3	20.49	0.182	153.3	1.57	2.27	13.6	19.33	0.165	73.5	1.67	2.37	21.1	19.00	0.396	93.7	1.41	2.12
10.2	20.62	0.195	172.8	1.56	2.19	15.0	19.53	0.157	75.2	1.66	2.39	24.0	19.15	0.419	93.9	1.43	2.12
11.3	20.71	0.202	152.9	1.59	2.24	16.5	19.72	0.155	75.0	1.66	2.33	27.1	19.31	0.436	94.2	1.42	2.11
12.4	20.90	0.186	172.0	1.53	2.15	18.2	19.91	0.148	75.5	1.65	2.32	30.9	19.48	0.458	94.4	1.41	2.10
13.6	20.98	0.208	154.5	1.59	2.24	20.0	20.09	0.147	75.2	1.66	2.32	34.5	19.62	0.472	94.4	1.41	2.09
15.0	21.13	0.212	172.3	1.55	2.23	22.0	20.27	0.149	75.2	1.64	2.26	39.2	19.80	0.485	93.9	1.41	2.06
16.5	21.34	0.202	157.3	1.51	2.14	24.2	20.45	0.150	77.4	1.64	2.34	44.5	19.98	0.500	93.4	1.42	2.06
18.2	21.42	0.215	158.5	1.56	2.13	26.6	20.62	0.152	80.2	1.63	2.33	49.7	20.18	0.503	93.5	1.39	2.05
20.0	21.61	0.225	178.8	1.52	2.03	29.2	20.77	0.169	82.9	1.65	2.23	55.6	20.35	0.510	93.5	1.40	2.02
22.0	21.71	0.242	176.6	1.53	2.21	32.2	20.95	0.158	84.4	1.61	2.19	61.2	20.51	0.517	93.2	1.40	1.99
24.2	21.84	0.265	177.5	1.52	2.21	35.4	21.11	0.159	85.4	1.61	2.31	67.3	20.69	0.522	93.7	1.38	1.93
26.6	21.99	0.274	177.2	1.53	2.18	38.9	21.26	0.174	88.6	1.60	2.18	75.4	20.89	0.537	93.6	1.38	1.93
29.2	22.14	0.271	178.0	1.51	--	42.8	21.42	0.178	88.4	1.60	2.20	85.1	21.09	0.551	93.1	1.38	1.89
32.2	22.29	0.282	177.3	1.55	--	47.1	21.63	0.158	84.5	1.56	--	95.4	21.27	0.569	92.9	1.36	1.85
35.4	22.44	0.296	177.3	--	--	51.8	21.84	0.157	79.7	1.58	--	105.0	21.43	0.581	92.7	1.35	--
38.9	22.61	0.302	178.0	--	--	57.0	22.03	0.164	79.2	1.56	--	115.4	21.58	0.594	92.5	1.36	--
42.8	22.83	0.302	178.0	--	--	62.7	22.19	0.179	80.6	1.56	--	128.9	21.81	0.598	92.5	1.34	--
47.1	22.92	0.354	172.6	--	--	69.0	22.39	0.172	78.3	1.56	--	144.2	22.06	0.601	92.4	1.35	--
						75.8	22.59	0.188	72.3	--	--	158.7	22.34	0.583	91.7	1.34	--
												174.4	22.63	0.572	91.6	1.32	--
												193.8	23.01	0.537	--	1.30	--

TABLE IX. (continued)

NGC 2778						NGC 2832						NGC 3377					
Radius (1)	μ_R (2)	ϵ (3)	ϕ (4)	$B-R$ (5)	$U-R$ (6)	Radius (1)	μ_R (2)	ϵ (3)	ϕ (4)	$B-R$ (5)	$U-R$ (6)	Radius (1)	μ_R (2)	ϵ (3)	ϕ (4)	$B-R$ (5)	$U-R$ (6)
3.2	18.29	0.148	45.8	1.81	2.18	3.1	18.01	--	--	1.53	2.17	1.8	15.74	--	--	--	--
4.0	18.58	0.178	45.6	1.80	2.15	3.8	18.27	--	--	1.52	2.17	2.2	15.99	--	--	1.58	--
4.7	18.82	0.205	45.4	1.80	2.15	4.6	18.54	0.173	150.1	1.51	2.16	2.7	16.24	--	--	1.58	--
5.4	19.04	0.220	45.8	1.80	2.11	5.3	18.74	0.185	151.3	1.51	2.14	3.2	16.49	--	--	1.58	--
6.0	19.20	0.218	45.3	1.79	2.09	5.8	18.88	0.192	153.7	1.51	2.13	3.9	16.75	0.445	38.3	1.58	--
6.6	19.36	0.214	45.2	1.79	2.10	6.4	19.04	0.190	155.0	1.49	2.12	4.7	17.01	0.468	38.7	1.58	--
7.2	19.52	0.209	44.5	1.78	2.11	7.0	19.20	0.193	156.4	1.48	2.09	5.5	17.21	0.479	39.0	1.57	2.19
7.9	19.68	0.206	44.2	1.78	2.10	7.7	19.34	0.204	157.8	1.48	2.09	6.0	17.36	0.482	39.1	1.57	2.17
8.7	19.83	0.206	43.6	1.77	2.07	8.5	19.50	0.209	157.9	1.47	2.10	6.6	17.50	0.481	39.2	1.57	2.14
9.6	19.98	0.204	44.0	1.76	2.09	9.3	19.66	0.211	158.0	1.46	2.06	7.3	17.64	0.486	39.3	1.57	2.14
10.6	20.13	0.207	43.9	1.77	2.07	10.2	19.81	0.222	158.3	1.47	2.08	8.0	17.79	0.488	39.4	1.56	2.12
11.6	20.28	0.212	43.5	1.76	2.07	11.3	19.95	0.231	158.6	1.46	2.05	8.8	17.94	0.485	39.2	1.55	2.11
12.8	20.43	0.216	44.3	1.76	2.05	12.4	20.08	0.245	160.8	1.47	2.00	9.7	18.08	0.487	38.9	1.55	2.07
14.1	20.59	0.218	43.3	1.76	2.03	13.6	20.23	0.268	160.3	1.46	2.00	10.7	18.22	0.488	38.8	1.53	2.07
15.5	20.76	0.222	43.3	1.74	2.07	15.0	20.35	0.279	159.4	1.46	2.07	11.7	18.37	0.488	38.6	1.53	2.05
17.0	20.92	0.229	43.7	1.74	1.97	16.5	20.49	0.280	159.7	1.44	2.02	12.9	18.51	0.490	38.5	1.53	2.02
18.7	21.10	0.239	43.2	1.74	1.99	18.2	20.64	0.289	158.4	1.44	2.02	14.2	18.65	0.492	38.7	1.52	2.01
20.6	21.30	0.236	43.1	1.73	1.97	20.0	20.79	0.290	159.3	1.45	1.96	15.6	18.78	0.498	38.9	1.51	2.01
22.7	21.52	0.230	43.1	1.72	2.04	22.0	20.95	0.280	160.5	1.44	1.99	17.2	18.92	0.503	38.8	1.51	2.00
24.9	21.75	0.227	42.4	1.69	2.00	24.2	21.12	0.280	159.6	1.43	2.00	18.9	19.06	0.504	38.9	1.51	1.98
27.4	22.03	0.216	42.6	1.68	2.08	26.6	21.31	0.268	161.1	1.42	1.96	20.8	19.19	0.510	39.1	1.52	1.98
30.2	22.36	0.207	42.6	1.66	2.05	29.2	21.47	0.293	158.8	1.42	1.93	22.9	19.33	0.514	39.2	1.51	1.97
33.2	22.71	0.214	41.9	1.68	--	32.2	21.64	0.300	158.1	1.43	1.86	25.2	19.48	0.514	39.4	1.50	1.96
36.5	23.11	0.207	43.1	1.74	--	35.4	21.79	0.313	159.2	1.40	1.90	27.7	19.65	0.511	39.5	1.49	1.94
40.1	23.58	0.196	42.1	--	--	38.9	21.92	0.320	161.2	1.42	1.96	30.5	19.82	0.512	39.3	1.50	1.94
						42.8	22.06	0.337	161.6	1.38	1.85	33.5	20.00	0.509	39.2	1.50	1.93
						47.1	22.21	0.361	160.6	1.36	1.84	36.9	20.21	0.500	39.2	1.49	1.91
						51.8	22.37	0.378	158.8	1.35	1.91	40.6	20.43	0.488	39.2	1.50	1.91
						57.0	22.52	0.374	160.3	1.33	--	44.6	20.67	0.471	39.2	1.50	1.89
						62.7	22.63	0.381	163.1	1.36	--	49.1	20.91	0.457	39.0	1.48	1.86
						69.0	22.78	0.428	160.6	1.33	--	54.0	21.16	0.444	39.0	1.49	1.84
						75.8	22.95	0.431	159.7	1.27	--	59.4	21.41	0.429	39.0	1.48	1.82
						83.4	23.15	0.438	159.8	--	--	65.3	21.68	0.414	40.1	1.45	1.75
						91.8	23.36	0.448	159.0	--	--	71.8	21.97	0.393	41.2	1.45	1.82
												79.0	22.21	0.393	41.2	1.48	1.71
												86.9	22.48	0.393	41.2	--	--
												95.6	22.76	0.393	41.2	--	--

TABLE IX. (continued)

NGC 3379						NGC 3605						NGC 3665					
Radius (1)	μ_R (2)	ϵ (3)	ϕ (4)	$B-R$ (5)	$U-R$ (6)	Radius (1)	μ_R (2)	ϵ (3)	ϕ (4)	$B-R$ (5)	$U-R$ (6)	Radius (1)	μ_R (2)	ϵ (3)	ϕ (4)	$B-R$ (5)	$U-R$ (6)
4.0	16.30	0.093	67.7	1.65	2.33	3.2	18.20	--	--	1.43	1.85	3.1	17.28	--	--	1.62	2.17
4.9	16.57	0.079	73.4	1.64	2.33	3.9	18.47	--	--	1.42	1.84	3.8	17.50	--	--	1.61	2.14
5.5	16.74	0.077	74.9	1.62	2.31	4.6	18.72	--	--	1.41	1.82	4.6	17.73	--	--	1.61	2.13
6.1	16.88	0.075	75.0	1.61	2.30	5.4	18.92	--	--	1.41	1.82	5.3	17.90	0.359	26.7	1.61	2.14
6.7	17.03	0.075	73.9	1.61	2.30	5.9	19.05	0.305	19.3	1.41	1.83	5.8	18.03	0.365	26.6	1.61	2.15
7.4	17.17	0.074	74.1	1.61	2.29	6.5	19.19	0.320	19.1	1.42	1.82	6.4	18.16	0.372	26.3	1.62	2.15
8.1	17.31	0.072	74.4	1.61	2.28	7.1	19.33	0.332	18.9	1.41	1.80	7.0	18.28	0.377	26.3	1.62	2.15
8.9	17.46	0.073	73.7	1.61	2.26	7.9	19.48	0.342	19.1	1.41	1.83	7.7	18.42	0.378	25.5	1.61	2.12
9.8	17.62	0.074	73.2	1.61	2.25	8.6	19.64	0.353	18.6	1.41	1.81	8.5	18.57	0.357	26.4	1.59	2.11
10.7	17.78	0.075	72.7	1.61	2.24	9.5	19.79	0.362	18.4	1.40	1.81	9.3	18.78	0.049	15.5	1.52	2.06
11.8	17.94	0.076	72.5	1.61	2.24	10.5	19.96	0.371	18.6	1.40	1.82	10.2	18.86	0.079	19.2	1.57	2.12
13.0	18.11	0.076	71.3	1.61	2.24	11.5	20.12	0.383	18.5	1.41	1.80	11.3	18.94	0.117	22.8	1.63	2.19
14.3	18.29	0.076	70.6	1.60	2.20	12.7	20.29	0.394	18.3	1.41	1.77	12.4	19.03	0.152	23.8	1.64	2.17
15.7	18.47	0.078	70.3	1.60	2.20	13.9	20.47	0.401	18.4	1.40	1.76	13.6	19.14	0.183	22.7	1.61	2.14
17.3	18.66	0.078	70.4	1.60	2.18	15.3	20.65	0.411	18.1	1.40	1.78	15.0	19.28	0.203	22.5	1.59	2.13
19.0	18.84	0.083	69.5	1.59	2.16	16.8	20.86	0.416	18.1	1.40	1.82	16.5	19.42	0.214	24.0	1.56	2.09
20.9	19.01	0.090	69.9	1.59	2.17	18.5	21.10	0.417	17.8	1.41	1.79	18.2	19.57	0.225	25.0	1.54	2.08
23.0	19.17	0.098	70.1	1.58	2.15	20.4	21.36	0.418	17.3	1.42	1.79	20.0	19.72	0.232	25.4	1.54	2.07
25.3	19.32	0.108	70.1	1.59	2.14	22.4	21.64	0.418	17.7	1.39	1.72	22.0	19.88	0.234	25.3	1.54	2.05
27.9	19.46	0.113	69.4	1.58	2.13	24.6	21.87	0.434	18.3	1.40	1.78	24.2	20.05	0.231	25.0	1.54	2.04
30.6	19.59	0.121	69.8	1.59	2.14	27.1	22.23	0.425	18.8	1.38	1.84	26.6	20.23	0.227	25.5	1.52	2.03
33.7	19.72	0.127	69.8	1.58	2.13	29.8	22.67	0.402	19.2	1.40	--	29.2	20.41	0.226	25.1	1.52	2.02
37.1	19.86	0.129	69.5	1.58	2.12	32.8	23.09	0.384	19.4	1.37	--	32.2	20.57	0.231	26.7	1.52	2.01
40.8	20.01	0.132	69.7	1.57	2.11							35.4	20.75	0.233	26.3	1.52	2.00
44.9	20.17	0.132	70.3	1.58	2.09							38.9	20.93	0.232	26.8	1.51	2.02
49.3	20.36	0.133	70.5	1.58	2.09							42.8	21.11	0.235	27.2	1.52	1.98
54.3	20.56	0.129	70.9	1.57	2.09							47.1	21.30	0.232	28.0	1.51	1.98
59.7	20.76	0.130	71.0	1.57	2.07							51.8	21.51	0.227	28.3	1.48	2.04
65.7	20.98	0.135	69.4	1.57	2.06							57.0	21.69	0.226	28.7	1.49	1.99
72.2	21.21	0.131	69.0	1.56	2.03							62.7	21.89	0.228	29.2	1.48	2.01
79.5	21.43	0.126	70.0	1.55	1.99							69.0	22.09	0.228	28.4	1.46	1.94
87.3	21.66	0.124	70.3	1.56	2.02							75.8	22.29	0.227	28.5	1.47	2.03
96.0	21.92	0.124	70.8	1.55	2.00							83.4	22.51	0.222	31.0	1.45	1.89
105.6	22.18	0.120	71.5	1.54	1.98							91.8	22.70	0.224	33.4	1.49	--
116.2	22.40	0.133	70.4	1.56	--							101.0	22.93	0.230	33.1	1.45	--
127.8	22.64	0.143	72.4	1.54	--							111.1	23.14	0.234	35.8	1.46	--
140.6	22.85	0.158	72.5	--	--							122.2	23.31	0.267	36.3	--	--
154.6	23.11	0.153	78.1	--	--							134.4	23.60	0.267	36.3	--	--
169.5	23.31	0.148	80.2	--	--												

TABLE IX. (continued)

NGC 3801						NGC 4261						NGC 4278					
Radius (1)	μ_R (2)	ϵ (3)	ϕ (4)	$B-R$ (5)	$U-R$ (6)	Radius (1)	μ_R (2)	ϵ (3)	ϕ (4)	$B-R$ (5)	$U-R$ (6)	Radius (1)	μ_R (2)	ϵ (3)	ϕ (4)	$B-R$ (5)	$U-R$ (6)
3.2	18.68	--	--	--	--	3.9	17.13	--	--	1.66	--	3.7	16.83	0.129	18.3	1.65	--
3.9	18.83	--	--	--	--	4.7	17.37	0.235	158.8	1.65	2.28	4.4	17.07	0.135	17.8	1.65	--
4.7	19.05	0.408	118.8	--	--	5.4	17.56	0.238	158.6	1.64	2.27	5.1	17.25	0.137	17.8	1.65	2.20
5.5	19.23	0.364	119.7	1.75	--	6.0	17.69	0.239	158.4	1.64	2.28	5.6	17.37	0.140	17.3	1.65	2.20
6.0	19.37	0.334	119.7	1.73	--	6.6	17.83	0.242	158.7	1.64	2.28	6.2	17.49	0.143	16.6	1.65	2.20
6.6	19.50	0.313	119.9	1.74	--	7.2	17.98	0.241	158.3	1.64	2.27	6.8	17.62	0.146	16.2	1.64	2.18
7.3	19.63	0.289	120.6	1.73	2.34	7.9	18.12	0.242	158.5	1.63	2.26	7.5	17.75	0.150	15.2	1.63	2.16
8.0	19.77	0.262	121.6	1.71	2.28	8.7	18.26	0.246	158.7	1.64	2.25	8.2	17.89	0.155	15.1	1.63	2.13
8.8	19.89	0.241	123.1	1.68	2.24	9.6	18.40	0.249	158.2	1.63	2.24	9.1	18.03	0.153	15.3	1.61	2.10
9.7	20.00	0.244	123.7	1.68	2.22	10.6	18.54	0.251	158.3	1.63	2.23	10.0	18.18	0.150	15.5	1.61	2.06
10.7	20.12	0.240	123.0	1.67	2.30	11.6	18.68	0.251	158.4	1.63	2.24	11.0	18.35	0.144	16.4	1.60	2.06
11.7	20.27	0.233	119.2	1.61	2.19	12.8	18.81	0.248	158.1	1.62	2.22	12.1	18.53	0.137	16.6	1.59	2.07
12.9	20.38	0.246	119.0	1.59	2.10	14.1	18.96	0.240	158.1	1.62	2.20	13.3	18.72	0.133	17.0	1.58	2.05
14.2	20.43	0.265	120.6	1.60	2.14	15.5	19.11	0.232	158.3	1.62	2.19	14.6	18.90	0.130	16.6	1.57	2.04
15.6	20.61	0.274	120.3	1.59	2.10	17.0	19.27	0.223	158.1	1.62	2.18	16.1	19.10	0.130	17.4	1.57	2.01
17.2	20.74	0.292	121.7	1.60	2.08	18.7	19.45	0.208	158.7	1.61	2.18	17.7	19.26	0.130	17.9	1.58	1.99
18.9	20.87	0.307	119.7	1.57	2.04	20.6	19.62	0.202	158.3	1.61	2.21	19.4	19.47	0.120	17.0	1.56	1.98
20.8	20.96	0.337	120.7	1.61	2.10	22.7	19.82	0.191	158.6	1.61	2.18	21.4	19.68	0.106	16.9	1.55	1.98
22.8	21.13	0.360	121.3	1.56	2.01	25.0	20.00	0.183	159.0	1.61	2.17	23.5	19.89	0.098	19.1	1.55	1.95
25.1	21.24	0.387	122.2	1.53	1.93	27.4	20.20	0.179	158.8	1.59	2.13	25.9	20.09	0.089	20.1	1.55	1.92
27.6	21.34	0.415	123.5	1.52	2.00	30.2	20.39	0.176	158.7	1.58	2.08	28.5	20.27	0.092	24.3	1.54	1.92
30.4	21.51	0.432	123.2	1.46	1.85	33.2	20.59	0.167	159.2	1.57	2.08	31.3	20.44	0.106	25.4	1.54	1.91
33.4	21.69	0.442	123.6	1.44	1.79	36.5	20.77	0.164	158.6	1.58	2.12	34.5	20.64	0.080	27.5	1.53	1.89
36.8	21.88	0.460	122.4	1.43	1.78	40.2	20.95	0.165	159.4	1.56	2.08	37.9	20.78	0.097	30.1	1.55	1.89
40.5	22.08	0.482	122.0	1.39	1.72	44.2	21.09	0.174	160.7	1.59	2.08	41.7	20.96	0.097	32.2	1.52	1.85
44.6	22.32	0.483	121.4	1.36	1.62	48.6	21.30	0.161	159.3	1.53	2.03	45.9	21.15	0.090	31.6	1.51	1.85
49.0	22.60	0.466	120.4	1.30	1.62	53.5	21.44	0.156	158.8	1.55	2.01	50.4	21.35	0.090	33.5	1.50	1.81
53.9	22.74	0.493	119.4	1.37	1.69	58.8	21.61	0.154	158.6	1.56	1.98	55.5	21.56	0.088	36.1	1.50	1.80
59.3	22.93	0.494	119.4	1.35	1.61	64.7	21.78	0.149	161.0	1.54	1.94	61.0	21.78	0.088	35.3	1.48	1.79
65.2	23.22	0.448	119.5	1.25	--	71.1	21.95	0.147	159.9	1.54	--	67.1	22.01	0.086	37.1	1.46	1.75
71.8	23.42	0.435	121.1	--	--	78.2	22.15	0.146	163.2	1.51	--	73.9	22.21	0.097	35.1	1.47	1.79
						86.0	22.36	0.136	164.7	--	--	81.2	22.43	0.105	34.7	1.46	1.70
						94.6	22.56	0.143	163.7	--	--	89.4	22.64	0.110	36.7	1.46	1.70
						104.1	22.81	0.140	161.9	--	--	98.3	22.83	0.120	37.7	1.47	--
						114.5	23.01	0.150	162.9	--	--	108.1	23.05	0.115	37.7	1.47	--
						125.9	23.22	0.163	161.7	--	--	118.9	23.25	0.125	42.7	--	--

TABLE IX. (continued)

NGC 4374						NGC 4387						NGC 4406					
Radius (1)	μ_R (2)	ϵ (3)	ϕ (4)	$B-R$ (5)	$U-R$ (6)	Radius (1)	μ_R (2)	ϵ (3)	ϕ (4)	$B-R$ (5)	$U-R$ (6)	Radius (1)	μ_R (2)	ϵ (3)	ϕ (4)	$B-R$ (5)	$U-R$ (6)
2.7	16.04	0.183	137.5	--	--	2.7	17.66	--	--	--	2.17	3.1	16.63	0.120	129.3	--	--
3.2	16.20	0.195	137.4	--	--	3.2	17.83	--	--	1.65	2.15	3.7	16.85	0.122	129.3	1.59	--
3.9	16.40	0.191	135.2	1.65	--	4.0	18.04	--	--	1.64	2.13	4.5	17.07	0.133	125.4	1.59	--
4.7	16.63	0.188	132.3	1.64	--	4.7	18.22	0.261	141.2	1.64	2.13	5.1	17.23	0.139	123.8	1.59	--
5.5	16.80	0.194	129.3	1.63	--	5.4	18.38	0.280	141.3	1.64	2.13	5.7	17.34	0.143	123.3	1.59	--
6.0	16.93	0.194	129.1	1.63	--	5.9	18.49	0.296	141.2	1.64	2.12	6.2	17.46	0.148	122.2	1.59	--
6.6	17.06	0.194	128.5	1.63	2.29	6.5	18.62	0.309	141.0	1.64	2.12	6.8	17.57	0.155	121.5	1.59	2.23
7.3	17.20	0.193	128.1	1.63	2.28	7.2	18.75	0.320	141.0	1.64	2.12	7.5	17.68	0.160	120.6	1.58	2.22
8.0	17.33	0.192	127.5	1.63	2.27	7.9	18.89	0.328	141.3	1.64	2.12	8.3	17.79	0.164	120.3	1.59	2.22
8.8	17.47	0.189	126.9	1.62	2.26	8.7	19.04	0.338	140.9	1.63	2.12	9.1	17.91	0.169	120.0	1.59	2.21
9.7	17.62	0.182	125.9	1.62	2.24	9.6	19.19	0.346	140.8	1.63	2.12	10.0	18.02	0.175	119.6	1.59	2.20
10.4	17.73	0.170	126.5	1.63	2.23	10.5	19.35	0.359	140.9	1.63	2.11	11.0	18.14	0.177	119.8	1.58	2.20
11.4	17.89	0.166	126.2	1.62	2.23	11.6	19.51	0.373	140.7	1.63	2.14	12.1	18.26	0.180	119.5	1.58	2.19
12.6	18.05	0.159	125.9	1.62	2.22	12.7	19.68	0.384	140.7	1.64	2.13	13.3	18.39	0.182	119.0	1.57	2.18
13.9	18.21	0.155	125.9	1.62	2.21	14.0	19.85	0.393	140.6	1.63	2.13	14.7	18.52	0.184	119.5	1.57	2.17
15.2	18.38	0.153	125.8	1.61	2.19	15.4	20.05	0.397	140.7	1.62	2.10	16.1	18.64	0.194	120.0	1.57	2.18
16.8	18.54	0.150	126.1	1.61	2.19	17.0	20.23	0.407	140.5	1.63	2.13	17.7	18.77	0.195	120.5	1.57	2.16
18.4	18.69	0.147	125.9	1.61	2.20	18.7	20.44	0.412	140.6	1.62	2.14	19.5	18.90	0.199	120.3	1.57	2.17
20.3	18.85	0.147	126.0	1.61	2.19	20.5	20.65	0.413	140.9	1.62	2.12	21.5	19.04	0.202	120.5	1.56	2.17
22.3	19.00	0.145	126.0	1.61	2.17	22.6	20.89	0.411	141.4	1.62	2.14	23.6	19.16	0.209	121.6	1.57	2.14
24.5	19.15	0.141	125.2	1.61	2.18	24.8	21.15	0.408	142.2	1.61	2.09	26.0	19.29	0.217	121.2	1.57	2.14
27.0	19.31	0.134	125.2	1.60	2.16	27.3	21.41	0.405	142.7	1.61	2.10	28.6	19.41	0.226	122.0	1.57	2.14
29.7	19.48	0.125	124.9	1.60	2.15	30.0	21.70	0.394	142.9	1.63	2.11	31.4	19.53	0.234	122.4	1.56	2.14
32.7	19.64	0.118	125.0	1.60	2.13	33.0	21.99	0.385	143.3	1.59	--	34.6	19.65	0.238	123.1	1.56	2.11
35.9	19.81	0.113	124.1	1.60	2.14	36.3	22.28	0.376	143.5	1.58	--	38.0	19.79	0.239	123.2	1.56	2.09
39.5	19.98	0.110	124.9	1.59	2.12	40.0	22.57	0.361	143.5	1.60	--	41.8	19.92	0.244	123.3	1.56	2.10
43.5	20.15	0.106	124.4	1.60	2.12	44.0	22.86	0.350	143.1	1.61	--	46.0	20.06	0.245	123.0	1.56	2.09
47.8	20.33	0.102	124.2	1.59	2.09	48.4	23.14	0.344	142.9	--	--	50.6	20.22	0.242	123.3	1.55	2.07
52.6	20.52	0.096	123.6	1.59	2.10	53.2	23.41	0.341	142.2	--	--	55.7	20.37	0.247	124.6	1.56	2.06
57.8	20.71	0.085	122.9	1.57	2.06							61.3	20.52	0.253	125.3	1.55	2.05
63.6	20.92	0.076	122.8	1.57	2.05							67.4	20.69	0.253	125.3	1.54	2.05
69.0	21.07	0.068	125.3	1.57	2.06							74.1	20.86	0.249	124.8	1.53	2.03
75.9	21.26	0.054	129.0	1.56	2.06							81.5	21.00	0.253	123.4	1.55	2.03
83.5	21.46	0.055	136.4	1.55	2.02							89.6	21.15	0.261	121.7	1.55	2.05
91.8	21.66	0.052	134.6	1.55	1.99							98.6	21.32	0.267	120.0	1.56	2.06
101.0	21.87	0.043	136.6	1.56	1.96							108.5	21.50	0.264	119.0	1.57	2.06
111.1	22.09	0.041	137.6	1.55	1.98							119.3	21.70	0.259	118.3	1.57	--
122.2	22.28	0.050	131.7	1.56	--							131.2	21.87	0.275	117.5	1.58	--
135.0	22.50	0.051	137.1	1.54	--							144.4	22.03	0.295	117.9	1.59	--
148.5	22.70	0.064	133.9	1.57	--							158.8	22.16	0.329	118.1	1.60	--
163.3	22.93	0.071	135.9	1.58	--							174.7	22.30	0.356	119.0	--	--

TABLE IX. (continued)

NGC 4472						NGC 4478						NGC 4486					
Radius (1)	μ_R (2)	ϵ (3)	ϕ (4)	$B-R$ (5)	$U-R$ (6)	Radius (1)	μ_R (2)	ϵ (3)	ϕ (4)	$B-R$ (5)	$U-R$ (6)	Radius (1)	μ_R (2)	ϵ (3)	ϕ (4)	$B-R$ (5)	$U-R$ (6)
3.2	16.22	0.067	164.5	--	--	3.2	17.39	0.144	152.6	--	--	4.6	17.01	0.022	137.6	1.68	2.27
3.9	16.37	0.067	163.1	--	--	4.0	17.72	0.148	150.6	1.54	2.09	5.3	17.08	0.020	137.3	1.68	2.28
4.7	16.54	0.069	163.9	1.68	--	4.6	17.89	0.155	150.3	1.54	2.08	5.8	17.14	0.016	151.4	1.68	2.29
5.4	16.68	0.076	164.9	1.67	--	5.4	18.04	0.163	148.8	1.55	2.08	6.4	17.21	0.023	168.8	1.68	2.29
5.9	16.78	0.080	164.1	1.67	--	5.9	18.15	0.170	147.7	1.55	2.09	7.0	17.28	0.029	175.6	1.68	2.29
6.5	16.88	0.087	164.0	1.67	--	6.5	18.27	0.175	147.0	1.55	2.09	7.7	17.36	0.029	1.7	1.68	2.29
7.2	16.98	0.096	164.0	1.67	2.32	7.1	18.39	0.182	146.6	1.55	2.08	8.5	17.44	0.033	178.4	1.68	2.28
7.9	17.09	0.103	163.6	1.67	2.31	7.8	18.52	0.189	146.1	1.55	2.08	9.3	17.55	0.019	174.9	1.67	2.26
8.7	17.20	0.112	162.7	1.66	2.31	8.6	18.66	0.193	145.3	1.55	2.08	10.2	17.65	0.031	174.9	1.67	2.25
9.6	17.31	0.118	162.4	1.66	2.30	9.5	18.81	0.195	145.2	1.55	2.07	11.3	17.76	0.031	177.9	1.67	2.27
10.5	17.43	0.124	162.3	1.66	2.29	10.4	18.97	0.194	144.7	1.55	2.05	12.4	17.87	0.029	173.6	1.67	2.25
11.6	17.54	0.135	162.1	1.66	2.29	11.5	19.15	0.192	143.7	1.54	2.07	13.6	17.99	0.036	176.7	1.67	2.24
12.7	17.66	0.147	162.2	1.66	2.29	12.6	19.33	0.190	143.6	1.54	2.06	15.0	18.12	0.033	169.2	1.66	2.24
14.0	17.78	0.153	162.8	1.66	2.29	13.9	19.52	0.184	143.3	1.54	2.05	16.5	18.25	0.038	172.8	1.66	2.23
15.4	17.90	0.163	162.3	1.66	2.28	15.3	19.73	0.181	142.9	1.54	2.06	18.2	18.38	0.044	171.2	1.66	2.22
17.0	18.01	0.173	162.3	1.66	2.28	16.8	19.96	0.177	142.0	1.54	2.03	20.0	18.52	0.044	168.5	1.66	2.21
18.7	18.14	0.179	162.1	1.66	2.28	18.5	20.21	0.171	141.1	1.53	2.01	22.0	18.67	0.045	166.4	1.65	2.19
20.5	18.26	0.179	162.2	1.66	2.27	20.3	20.45	0.169	140.4	1.52	2.02	24.2	18.81	0.051	164.3	1.65	2.18
22.6	18.40	0.180	162.0	1.66	2.27	22.4	20.71	0.162	138.9	1.53	2.01	26.6	18.96	0.053	163.2	1.64	2.16
24.8	18.54	0.180	161.9	1.66	2.27	24.6	20.98	0.163	137.9	1.52	2.00	29.2	19.12	0.053	161.8	1.64	2.13
27.3	18.68	0.181	161.6	1.66	2.27	27.0	21.25	0.160	136.4	1.52	2.01	32.2	19.27	0.055	160.6	1.64	2.12
30.0	18.84	0.178	161.4	1.66	2.24	29.7	21.55	0.159	136.1	1.49	1.94	35.4	19.42	0.062	159.6	1.63	2.12
33.0	19.00	0.175	161.5	1.65	2.25	32.7	21.81	0.167	135.9	1.52	1.94	38.9	19.57	0.071	159.8	1.64	2.10
36.3	19.17	0.166	161.1	1.65	2.23	36.0	22.12	0.176	136.9	1.51	1.99	42.8	19.72	0.080	158.1	1.63	2.05
39.9	19.33	0.167	160.8	1.65	2.22	39.6	22.42	0.178	138.5	1.51	1.96	47.1	19.89	0.074	157.5	1.62	2.01
44.0	19.50	0.168	160.3	1.64	2.22	43.5	22.76	0.177	140.2	1.49	--	51.8	20.05	0.082	157.5	1.62	2.04
48.4	19.66	0.167	160.4	1.64	2.19	47.9	23.11	0.164	143.5	1.48	--	57.0	20.21	0.083	156.4	1.62	2.04
53.2	19.81	0.170	160.2	1.64	2.18	52.7	23.45	0.143	148.5	1.47	--	62.7	20.36	0.087	156.2	1.62	2.03
58.5	19.97	0.172	159.5	1.63	2.17	58.0	23.82	0.121	155.3	--	--	69.0	20.52	0.100	155.9	1.61	2.01
64.4	20.11	0.179	159.5	1.63	2.16							75.8	20.69	0.097	157.1	1.61	1.98
70.8	20.26	0.177	159.0	1.63	2.15							83.4	20.86	0.105	155.5	1.61	1.96
77.9	20.41	0.176	158.9	1.63	2.15							91.8	21.04	0.105	154.8	1.61	1.95
85.7	20.58	0.175	158.8	1.63	2.14							101.0	21.23	0.110	155.8	1.61	1.95
94.2	20.75	0.170	158.3	1.63	2.12							111.1	21.43	0.118	156.2	1.60	1.93
103.6	20.93	0.169	158.1	1.63	2.13							122.2	21.64	0.131	154.2	1.60	1.91
116.7	21.23	0.164	156.7	1.60	2.06							134.4	21.87	0.135	153.4	1.59	1.85
128.3	21.46	0.160	155.6	1.59	2.05							147.8	22.05	0.148	150.7	1.59	--
141.2	21.69	0.165	155.1	1.59	2.06							162.6	22.28	0.148	150.7	--	--
155.3	21.90	0.178	153.5	1.60	2.07												
170.8	22.14	0.176	150.7	--	--												

TABLE IX. (continued)

NGC 4551					
Radius (1)	μ_R (2)	ϵ (3)	ϕ (4)	$B-R$ (5)	$U-R$ (6)
2.7	17.78	- -	- -	1.56	- -
3.2	17.99	0.219	67.5	1.55	- -
3.9	18.18	0.208	67.8	1.55	2.14
4.6	18.38	0.218	68.2	1.55	2.15
5.3	18.54	0.227	68.3	1.55	2.13
5.8	18.66	0.232	68.4	1.54	2.11
6.4	18.78	0.238	68.4	1.54	2.12
7.1	18.90	0.243	68.5	1.54	2.12
7.8	19.03	0.247	68.7	1.54	2.11
8.5	19.17	0.249	68.8	1.54	2.12
9.4	19.31	0.254	68.7	1.54	2.13
10.3	19.45	0.258	69.0	1.55	2.12
11.4	19.60	0.261	69.1	1.55	2.13
12.5	19.76	0.268	69.1	1.55	2.12
13.8	19.93	0.272	68.8	1.55	2.10
15.1	20.11	0.277	69.5	1.55	2.10
16.6	20.29	0.283	68.6	1.54	2.12
18.3	20.48	0.289	68.7	1.55	2.13
20.1	20.68	0.292	68.8	1.56	2.12
22.1	20.90	0.291	68.3	1.55	2.16
24.4	21.11	0.297	69.0	1.55	2.12
26.8	21.36	0.296	69.0	1.54	2.06
29.5	21.61	0.295	69.1	1.55	2.09
32.4	21.89	0.284	69.3	1.55	2.10
35.6	22.21	0.265	69.4	1.54	2.11
39.2	22.53	0.248	70.1	1.53	2.13
43.5	22.90	0.239	70.2	1.55	- -
47.8	23.28	0.229	70.8	- -	- -

NGC 4636					
Radius (1)	μ_R (2)	ϵ (3)	ϕ (4)	$B-R$ (5)	$U-R$ (6)
3.8	17.24	0.021	157.5	- -	- -
4.6	17.41	0.023	167.9	1.64	- -
5.3	17.55	0.023	166.4	1.63	- -
5.9	17.65	0.022	168.1	1.63	- -
6.4	17.76	0.023	163.9	1.62	- -
7.1	17.87	0.025	165.5	1.62	2.27
7.8	17.99	0.029	162.7	1.62	2.26
8.6	18.11	0.036	161.0	1.61	2.26
9.4	18.24	0.035	162.0	1.60	2.25
10.4	18.36	0.039	160.0	1.60	2.25
11.4	18.50	0.043	160.1	1.59	2.22
12.6	18.63	0.047	160.0	1.59	2.20
13.8	18.76	0.061	161.6	1.59	2.19
15.2	18.90	0.066	158.2	1.59	2.18
16.7	19.04	0.076	157.3	1.58	2.16
18.4	19.16	0.082	157.2	1.58	2.17
20.2	19.30	0.091	155.2	1.57	2.13
22.3	19.42	0.101	155.1	1.57	2.15
24.5	19.54	0.112	155.0	1.57	2.12
26.9	19.66	0.122	151.4	1.57	2.11
29.6	19.81	0.123	150.8	1.55	2.10
32.6	19.96	0.127	150.6	1.56	2.10
35.9	20.11	0.132	148.2	1.55	2.06
39.4	20.24	0.149	146.5	1.56	2.08
43.4	20.40	0.165	147.7	1.54	2.03
47.7	20.53	0.181	146.6	1.53	2.01
52.5	20.64	0.202	146.3	1.54	2.02
57.7	20.76	0.222	147.2	1.55	2.00
63.5	20.89	0.226	146.6	1.53	1.97
69.9	21.02	0.235	146.7	1.54	1.95
76.9	21.15	0.238	147.3	1.54	1.98
84.5	21.31	0.239	147.3	1.52	1.97
93.0	21.44	0.255	147.1	1.53	1.97
102.6	21.61	0.256	147.6	1.52	1.93
112.9	21.78	0.260	146.1	1.52	- -
124.2	21.96	0.263	147.4	1.51	- -
136.6	22.17	0.262	145.8	1.52	- -
150.2	22.38	0.269	145.7	1.53	- -
165.3	22.57	0.290	144.0	- -	- -

NGC 4649					
Radius (1)	μ_R (2)	ϵ (3)	ϕ (4)	$B-R$ (5)	$U-R$ (6)
3.2	16.28	0.053	94.8	- -	- -
3.9	16.41	0.066	97.5	- -	- -
4.7	16.57	0.082	96.4	- -	- -
5.4	16.70	0.089	97.9	1.67	- -
6.0	16.80	0.097	99.7	1.66	- -
6.6	16.91	0.105	100.0	1.66	- -
7.2	17.02	0.114	100.3	1.66	2.41
8.0	17.13	0.122	100.2	1.66	2.41
8.7	17.24	0.130	100.4	1.66	2.40
9.6	17.36	0.136	100.8	1.66	2.40
10.6	17.48	0.141	101.1	1.65	2.39
11.6	17.61	0.147	101.8	1.65	2.39
12.8	17.74	0.151	101.9	1.65	2.38
14.1	17.87	0.148	102.5	1.65	2.37
15.5	18.01	0.151	102.6	1.65	2.37
17.0	18.16	0.151	102.6	1.65	2.34
18.7	18.32	0.149	101.9	1.64	2.33
20.6	18.48	0.151	102.4	1.65	2.34
22.7	18.64	0.153	102.8	1.64	2.32
25.0	18.80	0.154	103.2	1.64	2.31
27.5	18.97	0.156	103.8	1.63	2.30
30.2	19.12	0.165	103.8	1.63	2.29
33.2	19.27	0.175	104.5	1.64	2.29
36.5	19.41	0.187	103.7	1.63	2.28
40.2	19.54	0.202	104.1	1.62	2.27
44.2	19.67	0.209	103.5	1.62	2.26
48.6	19.81	0.216	103.9	1.62	2.26
53.5	19.96	0.217	103.2	1.61	2.26
58.8	20.11	0.217	103.9	1.62	2.26
64.7	20.28	0.215	104.2	1.60	2.23
71.1	20.47	0.212	104.5	1.60	2.22
78.3	20.69	0.195	104.5	1.59	2.21
86.1	20.90	0.196	105.2	1.60	2.20
94.7	21.10	0.203	105.2	1.59	2.19
104.2	21.30	0.212	105.2	1.60	2.22
114.6	21.51	0.216	105.8	1.59	- -
126.0	21.76	0.211	106.9	1.56	- -
138.7	22.02	0.213	107.4	1.58	- -
152.5	22.30	0.215	105.9	1.63	- -
167.8	22.55	0.233	107.2	- -	- -
184.5	22.79	0.235	107.4	- -	- -

TABLE IX. (continued)

NGC 4697					
Radius (1)	μ_R (2)	ϵ (3)	ϕ (4)	$B-R$ (5)	$U-R$ (6)
2.6	16.29	--	--	--	--
3.2	16.44	--	--	--	--
3.8	16.60	0.323	64.9	--	--
4.8	16.79	0.354	66.2	--	--
5.4	16.92	0.363	66.8	--	--
5.9	17.02	0.371	66.6	1.60	2.19
6.5	17.13	0.376	66.7	1.60	2.18
7.2	17.24	0.381	66.7	1.60	2.18
7.9	17.36	0.386	66.9	1.59	2.16
8.7	17.48	0.388	66.9	1.59	2.15
9.6	17.60	0.392	66.8	1.59	2.16
10.5	17.72	0.393	66.7	1.59	2.14
11.6	17.85	0.390	66.7	1.58	2.13
12.7	17.97	0.388	66.8	1.57	2.12
14.0	18.11	0.387	66.8	1.57	2.10
15.4	18.24	0.387	67.0	1.57	2.09
16.9	18.36	0.394	67.6	1.57	2.09
18.6	18.49	0.397	67.4	1.56	2.08
20.5	18.63	0.402	66.8	1.56	2.08
22.5	18.75	0.415	66.8	1.56	2.06
24.8	18.87	0.426	66.8	1.55	2.05
27.2	18.99	0.435	66.9	1.55	2.04
30.0	19.12	0.447	66.7	1.55	2.03
33.0	19.26	0.452	66.8	1.54	2.03
36.3	19.40	0.455	66.9	1.54	2.03
39.9	19.55	0.451	67.2	1.54	2.01
43.9	19.71	0.447	67.2	1.54	2.00
48.2	19.89	0.438	67.0	1.53	1.99
53.1	20.08	0.420	67.5	1.52	1.98
58.4	20.29	0.402	67.7	1.52	1.96
64.2	20.51	0.385	67.8	1.52	1.95
70.6	20.75	0.366	67.1	1.50	1.92
77.7	20.97	0.353	67.2	1.49	1.91
85.4	20.19	0.342	67.4	1.49	1.90
94.0	21.44	0.319	67.2	1.46	1.85
104.5	21.72	0.306	67.2	1.44	1.85
115.0	21.96	0.301	67.6	1.42	1.85
126.5	22.18	0.300	69.1	1.43	--
139.2	22.38	0.308	69.2	1.41	--
153.1	22.60	0.308	68.8	1.39	--
168.5	22.84	0.317	68.4	--	--
187.6	23.08	0.307	66.7	--	--

NGC 4874					
Radius (1)	μ_R (2)	ϵ (3)	ϕ (4)	$B-R$ (5)	$U-R$ (6)
3.8	18.78	0.094	23.1	1.64	2.31
4.6	19.00	0.088	23.2	1.62	2.23
5.3	19.18	0.076	21.6	1.62	2.22
5.8	19.31	0.081	26.5	1.62	2.19
6.4	19.43	0.086	29.3	1.63	2.26
7.0	19.59	0.075	28.3	1.61	2.17
7.7	19.72	0.070	30.0	1.61	2.17
8.5	19.87	0.065	29.2	1.61	2.25
9.3	20.03	0.052	35.0	1.59	2.20
10.2	20.20	0.049	38.4	1.58	2.13
11.3	20.33	0.040	42.2	1.58	2.14
12.4	20.47	0.044	45.4	1.59	2.22
13.6	20.64	0.032	30.3	1.55	2.16
15.0	20.75	0.036	30.4	1.56	2.12
16.5	20.85	0.056	28.6	1.58	2.18
18.2	20.96	0.063	34.3	1.56	2.15
20.0	21.07	0.080	27.4	1.55	2.10
22.0	21.17	0.061	32.7	1.51	2.10
24.2	21.27	0.083	39.9	1.53	2.10
26.6	21.40	0.087	36.4	1.50	2.01
29.2	21.38	0.106	36.2	1.52	2.02
32.2	21.48	0.142	34.5	1.52	2.03
35.4	21.71	0.145	35.3	1.50	2.03
38.9	21.83	0.155	32.0	1.47	--
42.8	22.01	0.128	28.1	1.46	--
47.1	22.15	0.138	29.2	1.43	--
51.8	22.30	0.148	28.2	1.40	--
57.0	22.45	0.099	34.9	--	--
62.7	22.66	0.063	55.4	--	--
69.0	22.84	0.045	57.0	--	--
75.8	22.91	0.048	54.7	--	--
83.4	23.06	0.075	53.9	--	--
91.8	23.29	0.142	64.9	--	--

NGC 4889					
Radius (1)	μ_R (2)	ϵ (3)	ϕ (4)	$B-R$ (5)	$U-R$ (6)
3.8	18.10	--	--	1.56	2.33
4.6	18.33	--	--	1.55	2.33
5.3	18.50	--	--	1.56	2.34
5.8	18.64	0.237	77.3	1.56	2.35
6.4	18.77	0.246	77.4	1.56	2.31
7.0	18.92	0.254	77.3	1.55	2.28
7.7	19.07	0.266	77.6	1.53	2.27
8.5	19.21	0.273	77.4	1.53	2.24
9.3	19.36	0.276	77.8	1.52	2.23
10.2	19.50	0.286	78.1	1.53	2.19
11.3	19.66	0.299	77.8	1.52	2.15
12.4	19.81	0.300	78.0	1.51	2.10
13.6	19.96	0.309	77.9	1.51	2.20
15.0	20.10	0.313	78.3	1.50	2.26
16.5	20.26	0.325	78.5	1.50	2.18
18.2	20.39	0.325	78.5	1.49	2.21
20.0	20.51	0.346	78.3	1.53	2.13
22.0	20.69	0.348	77.7	1.51	2.01
24.2	20.87	0.342	78.3	1.48	2.17
26.6	21.03	0.344	78.5	1.48	2.10
29.2	21.19	0.345	78.7	1.46	2.21
32.2	21.34	0.340	78.4	1.48	2.30
35.4	21.51	0.339	79.7	1.48	2.28
38.9	21.68	0.341	79.7	1.48	2.18
42.8	21.86	0.334	81.4	1.41	2.14
47.1	22.06	0.350	78.5	1.38	2.09
51.8	22.26	0.362	75.1	1.37	2.05
57.0	22.43	0.374	77.5	1.37	--
62.7	22.59	0.375	79.2	1.36	--
69.0	22.82	0.352	80.5	1.30	--
75.8	22.99	0.366	79.1	1.31	--
83.4	23.20	0.363	80.5	--	--

TABLE IX. (continued)

NGC 5638						NGC 5813						NGC 5831					
Radius (1)	μ_R (2)	ϵ (3)	ϕ (4)	$B-R$ (5)	$U-R$ (6)	Radius (1)	μ_R (2)	ϵ (3)	ϕ (4)	$B-R$ (5)	$U-R$ (6)	Radius (1)	μ_R (2)	ϵ (3)	ϕ (4)	$B-R$ (5)	$U-R$ (6)
3.2	17.66	0.048	139.3	- -	- -	3.2	17.40	0.077	149.2	1.66	2.37	2.7	17.40	- -	- -	1.69	- -
3.9	17.89	0.048	139.9	1.61	- -	3.8	17.65	0.084	149.2	1.64	2.34	3.2	17.64	0.223	114.4	1.68	2.23
4.7	18.14	0.048	138.7	1.60	1.96	4.6	17.94	0.087	149.8	1.62	2.31	3.9	17.90	0.245	114.8	1.67	2.21
5.5	18.34	0.050	138.9	1.60	1.94	5.4	18.16	0.087	148.4	1.63	2.28	4.7	18.17	0.263	114.8	1.67	2.20
6.0	18.48	0.050	139.8	1.60	1.93	5.9	18.31	0.087	146.6	1.63	2.27	5.5	18.37	0.274	114.7	1.66	2.19
6.6	18.62	0.050	140.1	1.60	1.90	6.5	18.46	0.085	145.3	1.64	2.28	6.0	18.51	0.281	114.6	1.66	2.18
7.3	18.76	0.054	141.0	1.59	1.90	7.2	18.61	0.085	145.1	1.62	2.27	6.6	18.64	0.287	114.6	1.66	2.18
8.0	18.91	0.056	140.7	1.59	1.89	7.9	18.76	0.084	143.0	1.60	2.27	7.3	18.78	0.290	114.6	1.66	2.16
8.8	19.07	0.056	140.8	1.59	1.89	8.7	18.90	0.087	142.6	1.62	2.26	8.0	18.92	0.288	115.0	1.65	2.16
9.7	19.22	0.060	142.4	1.58	1.86	9.5	19.04	0.090	142.0	1.61	2.24	8.7	19.05	0.273	115.9	1.66	2.15
10.7	19.37	0.064	142.9	1.58	1.85	10.5	19.17	0.094	141.1	1.61	2.23	9.6	19.20	0.265	116.2	1.66	2.13
11.7	19.51	0.071	141.6	1.58	1.87	11.5	19.30	0.102	139.7	1.60	2.23	10.5	19.36	0.250	116.8	1.65	2.12
12.9	19.65	0.080	142.3	1.58	1.84	12.7	19.43	0.108	139.3	1.61	2.22	11.6	19.53	0.228	117.1	1.64	2.10
14.2	19.79	0.085	141.5	1.57	1.77	13.9	19.55	0.120	138.4	1.61	2.23	12.7	19.70	0.208	118.7	1.64	2.11
15.6	19.94	0.092	141.5	1.57	1.80	15.3	19.67	0.127	138.6	1.61	2.22	14.0	19.90	0.180	120.1	1.63	2.10
17.2	20.09	0.099	142.3	1.57	1.84	16.9	19.80	0.136	138.1	1.60	2.21	15.4	20.09	0.159	122.1	1.63	2.09
18.9	20.25	0.104	140.8	1.57	- -	18.6	19.93	0.144	138.2	1.60	2.22	17.0	20.29	0.140	124.0	1.62	2.10
20.8	20.43	0.106	141.8	1.57	- -	20.4	20.06	0.155	136.6	1.60	2.22	18.7	20.49	0.126	127.3	1.61	2.05
22.9	20.61	0.107	143.3	1.56	- -	22.5	20.18	0.168	136.0	1.60	2.22	20.5	20.67	0.119	129.7	1.62	2.04
25.2	20.81	0.105	143.9	1.55	- -	24.7	20.31	0.186	136.4	1.60	2.24	22.6	20.87	0.108	133.0	1.61	2.04
27.7	21.02	0.107	144.8	1.54	- -	27.2	20.43	0.195	136.2	1.59	2.20	24.8	21.06	0.093	135.4	1.60	2.06
30.5	21.22	0.112	146.0	1.52	- -	29.9	20.55	0.217	135.6	1.59	2.21	27.3	21.25	0.090	136.1	1.60	2.04
33.5	21.42	0.113	147.3	1.52	- -	32.9	20.66	0.231	134.9	1.59	2.22	30.0	21.44	0.089	135.4	1.60	2.05
36.9	21.63	0.118	149.1	1.51	- -	36.2	20.79	0.240	134.3	1.59	2.21	33.0	21.63	0.102	135.0	1.60	2.03
40.6	21.86	0.118	149.4	1.50	- -	39.8	20.92	0.250	133.6	1.59	2.20	36.4	21.83	0.110	135.1	1.60	2.08
44.6	22.11	0.119	148.6	1.49	- -	43.7	21.06	0.251	133.7	1.57	2.20	40.0	22.01	0.120	136.2	1.59	2.03
49.1	22.38	0.115	152.7	1.47	- -	48.1	21.22	0.251	133.7	1.57	2.16	44.0	22.20	0.129	138.3	1.58	2.04
54.0	22.65	0.121	159.4	- -	- -	52.9	21.38	0.255	133.2	1.58	2.18	48.4	22.41	0.131	138.1	1.58	2.05
59.4	22.96	0.112	160.7	- -	- -	58.2	21.55	0.257	133.5	1.57	2.19	52.8	22.59	0.140	140.7	1.60	- -
65.3	23.24	0.128	163.5	- -	- -	64.0	21.72	0.266	133.5	1.58	2.13	58.5	22.88	0.123	138.0	- -	- -
71.8	23.66	0.126	160.6	- -	- -	70.4	21.90	0.272	133.4	1.58	2.22	64.4	23.18	0.100	137.3	- -	- -
						76.0	22.04	0.276	134.6	1.58	2.22	69.0	23.38	0.099	141.6	- -	- -
						83.5	22.22	0.278	134.5	1.57	- -						
						91.9	22.41	0.286	134.7	1.57	- -						
						101.0	22.59	0.292	133.4	1.57	- -						
						111.2	22.78	0.296	132.5	1.57	- -						
						122.2	22.96	0.304	131.4	1.55	- -						
						134.5	23.15	0.307	130.5	- -	- -						
						148.1	23.28	0.329	131.0	- -	- -						
						163.0	23.46	0.335	128.4	- -	- -						
						172.6	23.53	0.358	123.8	- -	- -						

TABLE IX. (continued)

NGC 5845						IC 1101						NGC 6051					
Radius (1)	μ_R (2)	ϵ (3)	ϕ (4)	$B-R$ (5)	$U-R$ (6)	Radius (1)	μ_R (2)	ϵ (3)	ϕ (4)	$B-R$ (5)	$U-R$ (6)	Radius (1)	μ_R (2)	ϵ (3)	ϕ (4)	$B-R$ (5)	$U-R$ (6)
2.7	16.88	- -	- -	1.66	- -	2.7	19.55	- -	- -	1.63	- -	3.2	19.00	- -	- -	1.77	- -
3.2	17.23	- -	- -	1.65	- -	3.2	19.70	- -	- -	1.62	- -	4.0	19.26	0.186	164.6	1.76	2.48
3.9	17.61	- -	- -	1.65	2.43	4.0	19.88	- -	- -	1.61	- -	4.7	19.45	0.206	164.7	1.77	2.45
4.7	18.02	0.230	142.2	1.65	2.43	4.7	20.07	- -	- -	1.61	2.37	5.5	19.62	0.218	165.0	1.76	2.45
5.5	18.35	0.235	142.5	1.64	2.40	5.5	20.22	0.232	17.8	1.60	2.39	6.0	19.73	0.227	165.1	1.76	2.45
6.0	18.59	0.245	142.5	1.64	2.40	6.0	20.34	0.244	18.2	1.60	2.36	6.6	19.85	0.236	165.0	1.76	2.43
6.6	18.83	0.257	142.5	1.64	2.41	6.6	20.46	0.257	18.8	1.60	2.34	7.3	19.95	0.253	165.0	1.76	2.45
7.3	19.07	0.273	142.4	1.65	2.41	7.2	20.54	0.275	19.2	1.61	2.34	8.0	20.07	0.263	165.6	1.76	2.44
8.0	19.31	0.293	142.2	1.66	2.42	7.9	20.66	0.290	20.2	1.60	2.39	8.8	20.17	0.279	165.3	1.76	2.47
8.7	19.51	0.304	143.8	1.63	2.40	8.7	20.78	0.305	20.2	1.60	2.34	9.7	20.28	0.292	165.6	1.77	2.39
9.5	19.75	0.325	143.2	1.62	2.38	9.6	20.90	0.318	20.5	1.59	2.35	10.7	20.38	0.307	165.9	1.78	2.44
10.5	19.99	0.346	142.7	1.62	2.39	10.6	21.03	0.333	21.0	1.58	2.36	11.7	20.52	0.303	165.8	1.77	2.43
11.5	20.24	0.361	141.9	1.61	2.42	11.6	21.15	0.345	20.9	1.58	2.39	12.9	20.66	0.303	165.8	1.76	2.38
12.7	20.52	0.372	141.6	1.59	2.41	12.8	21.26	0.364	21.1	1.58	2.37	14.2	20.82	0.297	165.9	1.75	2.39
13.9	20.79	0.380	141.2	1.59	2.33	14.1	21.39	0.377	21.9	1.57	2.34	15.6	20.97	0.298	166.2	1.74	2.44
15.3	21.07	0.379	140.5	1.59	2.36	15.5	21.50	0.393	22.2	1.56	2.28	17.2	21.13	0.295	165.5	1.73	2.41
16.8	21.37	0.374	140.1	1.60	2.36	17.0	21.63	0.406	21.2	1.56	2.29	18.9	21.26	0.309	164.8	1.75	2.46
18.5	21.70	0.357	139.1	1.60	2.35	18.7	21.74	0.426	21.8	1.56	2.30	20.8	21.40	0.323	164.0	1.73	2.46
20.4	22.03	0.339	138.2	1.60	2.40	20.6	21.85	0.445	22.1	1.55	2.32	22.9	21.52	0.340	164.1	1.73	2.50
22.4	22.38	0.320	137.6	1.58	- -	22.6	21.98	0.448	22.8	1.54	2.28	25.2	21.65	0.354	163.9	1.69	2.44
24.7	22.75	0.284	136.2	1.55	- -	24.9	22.15	0.441	23.6	1.55	2.25	27.7	21.79	0.360	163.9	1.68	2.36
27.1	23.11	0.276	136.9	1.55	- -	27.4	22.31	0.443	24.2	1.55	2.29	30.5	21.93	0.371	164.5	1.70	2.41
29.8	23.49	0.251	134.0	- -	- -	30.1	22.47	0.458	24.2	1.53	- -	33.5	22.18	0.291	143.6	1.57	2.27
						33.1	22.61	0.471	24.3	- -	- -	36.9	22.21	0.389	167.9	1.62	- -
						36.5	22.76	0.486	24.9	- -	- -	40.6	22.45	0.373	165.3	1.56	- -
						40.1	22.91	0.498	25.1	- -	- -	44.6	22.58	0.391	165.6	1.67	- -
						44.1	23.13	0.490	25.5	- -	- -	49.1	22.74	0.402	165.5	1.72	- -
						48.5	23.28	0.510	23.7	- -	- -	54.0	22.90	0.415	165.6	1.83	- -
						53.4	23.52	0.502	24.1	- -	- -	59.4	23.25	0.406	166.2	- -	- -
						58.7	23.72	0.504	25.4	- -	- -						

TABLE IX. (continued)

NGC 6086						NGC 6269						NGC 7626					
Radius (1)	μ_R (2)	ϵ (3)	ϕ (4)	$B-R$ (5)	$U-R$ (6)	Radius (1)	μ_R (2)	ϵ (3)	ϕ (4)	$B-R$ (5)	$U-R$ (6)	Radius (1)	μ_R (2)	ϵ (3)	ϕ (4)	$B-R$ (5)	$U-R$ (6)
2.7	18.77	--	--	1.54	2.26	3.2	18.47	--	--	--	--	3.8	17.99	0.072	0.8	1.69	2.36
3.2	19.06	0.247	3.6	1.53	2.24	3.9	18.72	0.251	81.8	--	--	4.6	18.25	0.080	2.8	1.71	2.39
3.9	19.37	0.256	2.7	1.53	2.23	4.7	18.98	0.266	81.5	1.67	--	5.3	18.44	0.094	3.3	1.71	2.35
4.7	19.71	0.256	2.5	1.52	2.22	5.5	19.18	0.273	81.8	1.66	--	5.8	18.56	0.094	3.3	1.70	2.30
5.5	19.96	0.255	1.8	1.52	2.19	6.0	19.33	0.274	81.1	1.65	--	6.4	18.68	0.101	5.6	1.71	2.35
6.0	20.13	0.264	1.8	1.52	2.12	6.6	19.49	0.271	81.1	1.64	2.31	7.0	18.81	0.103	4.9	1.70	2.36
6.6	20.29	0.273	1.6	1.51	2.14	7.3	19.65	0.267	81.1	1.63	2.34	7.7	18.93	0.108	3.8	1.70	2.32
7.3	20.45	0.284	1.3	1.50	2.14	8.0	19.82	0.261	81.2	1.62	2.33	8.5	19.06	0.107	5.2	1.70	2.32
8.0	20.59	0.296	1.3	1.50	2.10	8.8	19.99	0.253	80.8	1.62	2.35	9.3	19.19	0.108	6.3	1.71	2.32
8.8	20.72	0.315	1.3	1.52	2.15	9.7	20.14	0.256	80.1	1.61	2.36	10.2	19.32	0.115	7.4	1.70	2.29
9.7	20.86	0.318	1.5	1.51	2.18	10.5	20.26	0.242	81.7	1.61	2.30	11.3	19.47	0.111	7.4	1.70	2.31
10.5	21.00	0.307	3.3	1.48	2.16	11.5	20.41	0.250	81.0	1.61	2.30	12.4	19.62	0.110	9.5	1.71	2.29
11.5	21.19	0.292	2.2	1.48	2.10	12.7	20.56	0.256	81.2	1.61	2.29	13.6	19.76	0.113	10.2	1.70	2.29
12.7	21.35	0.298	3.0	1.47	2.16	13.9	20.71	0.250	81.3	1.61	2.25	15.0	19.91	0.121	10.7	1.69	2.27
13.9	21.50	0.312	3.2	1.52	2.12	15.3	20.87	0.244	81.2	1.60	2.28	16.5	20.07	0.125	9.7	1.70	2.30
15.3	21.68	0.311	3.4	1.50	2.11	16.8	21.03	0.243	81.3	1.59	2.26	18.2	20.22	0.132	12.0	1.72	2.23
16.9	21.92	0.294	3.3	1.48	2.20	18.5	21.18	0.247	80.9	1.61	2.27	20.0	20.37	0.134	10.7	1.70	2.23
18.6	22.08	0.298	2.4	1.52	2.12	20.4	21.35	0.243	79.8	1.59	2.25	22.0	20.53	0.145	12.9	1.69	2.21
20.0	22.24	0.302	2.9	1.51	2.05	22.4	21.53	0.248	80.4	1.58	2.20	24.2	20.68	0.151	11.1	1.68	2.25
22.0	22.41	0.310	3.9	1.46	2.04	24.6	21.70	0.253	79.7	1.57	2.30	26.6	20.84	0.151	11.4	1.67	2.19
24.2	22.58	0.316	5.1	1.49	1.96	27.1	21.88	0.258	78.1	1.56	--	29.2	20.99	0.161	15.1	1.69	2.20
26.6	22.74	0.329	4.8	1.50	2.09	29.8	22.05	0.266	77.1	1.56	--	32.2	21.16	0.157	12.4	1.67	2.19
29.2	22.89	0.348	5.7	1.50	--	32.8	22.25	0.266	76.9	1.54	--	35.4	21.31	0.173	10.9	1.68	2.18
32.2	23.02	0.369	5.0	1.49	--	36.1	22.42	0.278	76.4	1.52	--	38.9	21.49	0.182	12.5	1.70	2.16
35.4	23.18	0.372	5.7	1.52	--	39.7	22.59	0.290	77.5	1.54	--	42.8	21.67	0.181	12.5	1.67	--
38.9	23.30	0.387	6.2	1.47	--	43.7	22.77	0.296	76.6	1.51	--	47.1	21.87	0.177	12.5	1.66	--
42.8	23.46	0.398	7.7	1.38	--	48.0	22.94	0.314	75.5	1.52	--	51.8	22.12	0.143	11.8	1.67	--
47.1	23.65	0.392	6.8	1.50	--	52.8	23.09	0.332	76.1	--	--	57.0	22.31	0.155	10.7	1.70	--
51.8	23.95	0.372	6.8	--	--	58.1	23.30	0.331	77.9	--	--	62.7	22.55	0.136	7.2	1.68	--
57.0	24.13	0.366	5.5	--	--							69.0	22.74	0.157	13.5	--	--

Notes to TABLE IX

Column (1) gives the radius along the major axis in arcsec, column (2) the surface brightness in Cousins R in mag arcsec^{-2}, and column (3) the ellipticity $1-b/a$. The position angle of the major axis measured from N through E is given in column (4), while columns (5) and (6) list the $B-R$ and $U-R$ colors in mag arcsec^{-2}.

NGC 5638. We only have 2.1 m data for this galaxy. An unexpected problem with the data in U caused us to delete a large fraction ($\simeq 40\%$) of the pixels from this frame, so the U results are less than optimum. As a result only the inner parts of the $U-R$ color profile are shown and the ellipticity and position angle profiles in U are omitted. It is one of the roundest ellipticals in our sample, and shows no significant higher-order structure.

NGC 5813. This galaxy has been studied previously by Efstathiou, Ellis, and Carter (1982). Kormendy (1984) argued that the unusual kinematic and structural character of the core was the result of the accretion of a smaller galaxy by NGC 5813. There appear to be no large-scale structural features resulting from that accretion, except for some dust in the nuclear regions. A N–S gradient in the background on the B and R frames was modeled and removed from the 0.9 m telescope frames. It is interesting that while the color gradients are so small, and are consistent between 0.9 and 2.1 m, NGC 5813 has a very steep Mg_2 gradient (Gorgas and Efstathiou 1987). This discrepancy is probably not due to dust. This unusual characteristic is also discussed in Peletier (1989).

NGC 5831. The ellipticity profile is somewhat unusual in that it decreases beyond 8″, making the NGC 5831 the only galaxy in the sample with small high-order terms and a decreasing ellipticity. An isophote twist of $>20°$ is seen between radii of 10″–25″. A particularly interesting feature of this galaxy is that the weak disk, initially along the major axis, remains at a constant position angle, even as the major axis skews (see Fig. 9).

NGC 5845. This very small galaxy has an effective radius which is a factor 3 smaller than that of the next smallest galaxy, as well as a very high central surface brightness. There is a good indication of a disk, associated with some dust on the major axis, between $\approx 5''$ and 15″. The quality of the data is good.

IC 1101. This is the cD galaxy in Abell 2029; the most luminous galaxy in our sample, at a redshift z of almost 0.08.The photometry is a compilation of a large number of frames, taken with both telescopes. The galaxy is a low surface brightness object, as can be expected for a cD. Many companion galaxies have been deleted. The ellipticity increases very rapidly outward from the center. The $n\theta$ terms are uncertain, although the agreement between B and R is good. Due to the lack of aperture photometry our absolute calibration is uncertain in U.

NGC 6051 (AWM 4). The galaxy was offset to the W on the frame to avoid a bright star. The data do not extend to very large radii, since only 2.1 m data were taken. A large number of companion galaxies have been masked out.

NGC 6086. The central galaxy in Abell 2162. The frame taken on the 2.1 m was positioned between two bright stars; one at 42″ to the SE and the other at 170″ to the SW. Many companion galaxies were masked out.

NGC 6269 (AWM 5). A highly luminous galaxy with data from both telescopes. Many companion galaxies were masked out.

NGC 7626. One of the two brightest ellipticals in the Pegasus I cluster—paired with the higher luminosity NGC 7619. The only data for this galaxy were taken in the October 1982 run. It is not of the quality of the later data. Beyond 60″ the shape parameters in B have been kept constant. Although the galaxy itself rotates quite slowly, its core rotates with an amplitude of $\approx 40\ \mathrm{km\,s^{-1}}$ (Jedrzejewski and Schechter 1988). There is also shell structure to the east of the galaxy, indicative of an interaction/acquisition.

APPENDIX B: FIGURES AND TABLES FOR INDIVIDUAL GALAXIES

The surface brightness, color, ellipticity, and position angle profiles, as well as the sin and cos 3θ and 4θ profiles, resulting from the reduction, calibration and analysis described in Secs. II–V are plotted in Fig. 15 for the 39 galaxies studied in this program. The surface brightness, ellipticity, position angle, and $B-R$ and $U-R$ color profile data are also tabulated in Table IX. The seeing FWHM in arcseconds and the sky background level in R mag arcsec^{-2} are shown on the plots. The seeing FWHM in the three bands is given at the top of each figure. The sky surface brightness in each band is given in Table III. Error bars have not generally been plotted since the major sources of error are systematic. For the $n\theta$ terms where the systematic errors are probably not dominant, an estimate of the uncertainty can be obtained from the scatter of the points. For the color profiles where the errors are systematic and probably comparable to the size of the gradient in many cases (particularly $B-R$), we give the uncertainty that results from a 1% error in the sky level. Since the uncertainty from the sky is most likely highly correlated between the different bands, these error bars represent upper limits to the actual uncertainty. They serve, however, as a useful guide to the confidence level that one can place on the results.

We have not tabulated the 3θ and 4θ terms. If desired these numbers can be obtained from the first author, either in tabulated or in computer-readable form.

REFERENCES

Bender, R. (1988). Astron. Astrophys. **193**, L7.

Bender, R., Döbereiner, S., and Möllenhoff, C. (1987). Astron. Astrophys. **177**, L53.

Bender, R., and Möllenhoff, C. (1987). Astron. Astrophys. **177**, 71.

Bender, R., Döbereiner, S., and Möllenhoff, C. (1988). Astron. Astrophys. Suppl. **74**, 385.

Bender, R., Surma, P., Döbereiner, S., Möllenhoff, C., and Madejsky, R. (1989). Astron. Astrophys. **217**, 35.

Bessell, M. (1979). Publ. Astron. Soc. Pac. **91**, 589.

Binney, J., and Petrou, M. (1985). Mon. Not. R. Astron. Soc. **214**, 449.

Binney, J., Davies, R. L., and Illingworth, G. D. (1990). Astrophys J. (to be published).

Birkinshaw, M., and Davies, R. L. (1985). Astrophys. J. **291**, 32.

Boroson, T. A., Thompson, T. B., and Shectman, S. A. (1983). Astron. J. **88**, 1707.

Burstein, D., Faber, S. M., Gaskell, C. M., and Krumm, N. (1984). Astrophys. J. **287**, 586.

Burstein, D., Davies, R. L., Dressler, A., Faber, S. M., Stone, R. P. S., Lynden-Bell, D., Terlevich, R., and Wegner, G. (1987). Astrophys. J. Suppl. **64**, 601.

Butcher, H. R., Van Breugel, W. J. M., and Miley, G. K. (1980). Astrophys. J. **235**, 749.

Canizares, C. R., Fabbiano, G., and Trinchieri, C. (1987). Astrophys. J. **312**, 503.

Carlberg, R. G. (1984). Astrophys. J. **286**, 403.

Carter, D. (1978). Mon. Not. R. Astron. Soc. **182**, 797.

Carter, D. (1987). Astrophys. J. **312**, 514.

Carter, D., Inglis, I., Ellis, R. S., Efstathiou, G., and Godwin, J. G., (1985). Mon. Not. R. Astron. Soc. **212**, 471.

Cawson, M. C. (1983). Ph.D. thesis, University of Cambridge.

Cohen, J. (1979). Astrophys. J. **228**, 405.

Cohen, J. (1986). Astron. J. **92**, 1039.

Davies, R. L., Efstathiou, G., Fall, M., Illingworth, G., and Schechter, P. (1983). Astrophys. J. **266**, 41 (DEFIS).

Davies, R. L., and Illingworth, G. D. (1986). Astrophys. J. **302**, 234.

Davies, R. L., and Birkinshaw, M. (1986). Astrophys. J. **303**, L45.

Davies, R. L., and Birkinshaw, M. (1988). Astrophys. J. Suppl. **68**, 409.

Davies, R. L., Burstein, D., Dressler, A., Faber, S. M., Lynden-Bell, D., Terlevich, R. J., and Wegner, G. (1987). Astrophys. J. Suppl. **64**, 581.

Davies, R. L., and Sadler, E. M. (1987). In *Structure and Dynamics of Elliptical Galaxies*, IAU Symposium No. 127, edited by P. T. de Zeeuw (Reidel, Dordrecht), p. 441.

Davis, L. E., Cawson, M., Davies, R. L., and Illingworth, G. (1985). Astron. J. **90**, 169 (Paper I).

De Vaucouleurs, G., De Vaucouleurs, A., and Corwin, H. G. (1976). *Second Reference Catalog of Bright Galaxies* (University of Texas Press, Austin) (RC2).

Djorgovski, S. (1983). J. Astrophys. Astron. **4**, 271.

Djorgovski, S., (1985). Ph.D. thesis, University of California, Berkeley.

Ebneter, K., and Balick, B. (1985). Astron.J. **90**, 183.

Efstathiou, G., Ellis, R. S., and Carter, D. (1982). Mon. Not. R. Astron. Soc. **201**, 975.

Franx, M., and Illingworth, G. D. (1988). Astrophys. J. **327**, L55.

Franx, M., Illingworth, G. D., and Heckman, T. (1989a). Astrophys.J. **344**, 613.

Franx, M., Illingworth, G. D., and Heckman, T. (1989b). Astron. J. **98**, 538.

Gorgas, J., and Efstathiou, G. (1987). In *Structure and Dynamics of Elliptical Galaxies*, IAU Symposium No. 127, edited by P. T. de Zeeuw (Reidel, Dordrecht), p. 189.

Green, E. M., Demarque, P., and King, C. R. (1987). Yale University Transaction. In preparation.

Gunn, J. E. (1979). In *Active Galactic Nuclei*, edited by C. Hazard and S. Mitton (Cambridge University Press,Cambridge, England), p. 213.

Gunn, J. E., and Stryker, L. L. (1983), Astrophys. J. **52**, 121.

Hansen, L., Nørgaard-Nielsen, H. U., and Jørgensen, H. E. (1984). Astron. Astrophys. **149**, 442.

Heckman, T. M., Balick, B., Van Breugel, W. J. M., and Miley, G. K. (1983). Astron. J. **88**, 583.

Illingworth, G. D., and Franx, M. (1988). In *Dynamics of Dense Stellar Systems*, edited by D. Merritt (Cambridge University, Cambridge), p. 13.

Illingworth, G. D., and Jedrzejewski, R. (1990). In preparation.

Jedrzejewski, R. I. (1987). Mon. Not. R. Astron. Soc. **226**, 747.

Jedrzejewski, R. I., and Schechter, P. L. (1988). Astrophys. J. **327**, L55.

Kent, S. E. (1984). Astrophys. J. Suppl. **56**, 305.

King, I. R. (1978). Astrophys. J. **222**, 1.

Knapp, G. R., Guhathakurta, P., Kim, D.-W., and Jura, M. (1989). Astrophys. J. Suppl. **70**, 329.

Kormendy, J. (1984). Astrophys. J. **287**, 577.

Kormendy, J., and Illingworth, G. D. (1983). Astrophys. J. **265**, 632.

Kormendy, J., and Stauffer, J. (1987). In *Structure and dynamics of elliptical galaxies*, IAU Symposium No. 127, edited by P. T. de Zeeuw (Reidel, Dordrecht), p. 405.

Kormendy, J., and Djorgovski, S. (1989). Annu. Rev. Astron. Astrophys. **27**, 235.

Kotanyi, C. (1979). Astron. Astrophys. **74**, 156.

Larson, R. B., (1975). Mon. Not. R. Astron. Soc. **173**, 671.

Lauer, T. R. (1985). Astrophys. J. Suppl. **57**, 473.

Longo, G., and de Vaucouleurs, A. (1983). A General Catalog of Photoelectric Magnitudes and Colors in the *U,B,V* System of 3 578 Galaxies Brighter then the 16th *V* Magnitude (1936–1982), Texas Monographs in Astronomy 3, University of Texas.

Longo, G., and de Vaucouleurs, A. (1985). Supplement to the General Catalog of Photoelectric Magnitudes and Colors of Galaxies in the *U,B,V* System, Texas Monographs in Astronomy 3a, University of Texas.

Malumuth, E. M., and Kirshner, R. P. (1985). Astrophys. J. **291**, 8.

Michard, R. (1985). Astron. Astrophys. Suppl. **59**, 205.

Mould, J. R. (1978). Astrophys.J. **220**, 434.

Peletier, R. F. (1989). Ph.D. thesis, University of Groningen.

Peletier, R. F., Valentijn, E. A., and Jameson, R. F. (1990). Astron. Astrophys. **233**, 62.

Persson, S. E., Frogel, J. A., and Aaronson, M. (1979). Astrophys. J. Suppl. **39**, 61.

Raimond, E., Faber, S. M., Gallegher, J. S., and Knapp, G. R. (1981). Astrophys. J. **246**, 708.

Sandage, A. R. (1972). Astrophys. J. **176**, 21.

Sandage, A. R., and Tammann, G. (1981). A Revised Shapley–Ames Catalog of Bright Galaxies (Carnegie Institute of Washington, Washington, DC) (RSA).

Sandage, A. R., and Visvanathan, N. (1978). Astrophys. J. **223**, 707.

Schweizer, F. (1979). Astrophys. J. **233**, 23.

Schweizer, F. (1981). Astron. J. **86**, 662.

Strom, K. M., Strom, S. E., Wells, D. C., and Romanishin, W. (1978), Astrophys. J. **220**, 62.

Terlevich, R. J., Davies, R. L., Faber, S. M., and Burstein, D. (1981). Mon. Not. R. Astron. Soc. **196**, 381.

Tonry, J., and Davis, M. (1981). Astrophys. J. **246**, 666.

Vader, J. P., Vigroux, L., Lachièze-Rey, M., and Souviron, J. (1988). Astron. Astrophys. **203**, 217.

Vigroux, L., Souviron, J., Lachièze-Rey, M., and Vader, J. P. (1988). Astron. Astrophys. Suppl. **73**, 1.

Whitford, A. E. (1971). Astrophys. J. **169**, 215.

Whitmore, B. C. (1980). Astrophys. J. **242**, 53.

White, S. D. M. (1979). Mon. Not. R. Astron. Soc. **189**, 831.